

PHYSICS OF PARTICLE TRAPPING IN ULTRARELATIVISTIC PLASMA
WAKES

by

Erdem Oz

A Dissertation Presented to the
FACULTY OF THE GRADUATE SCHOOL
UNIVERSITY OF SOUTHERN CALIFORNIA
In Partial Fulfillment of the
Requirements for the Degree
DOCTOR OF PHILOSOPHY
(PHYSICS)

December 2007

Copyright 2007

Erdem Oz

Dedication

To my parents Sakir, Sadiye and my sister Ezgi

Acknowledgments

I always wanted to be a scientist. I admired the scientists who solved the great mysteries of life. Although I had a strong physics background, I do not think I was even close to becoming a true scientist until I joined the plasma accelerator group at the University of Southern California. Here I had a chance to work with a number of great scientists from the University of Southern California (USC), University of California Los Angeles (UCLA) and Stanford Linear Accelerator Center (SLAC). I cannot thank them enough.

I was very lucky to have met my adviser Thomas Katsouleas and my experimental adviser Patric Muggli. They are not only role models as great scientist but also as great people too. I am very grateful for their support and I will try to follow their footsteps for the rest of my life.

I would like to thank all the distinguished members of our collaboration: Suzhi Deng, Thomas Katsouleas and Patric Muggli from USC, Chris Barnes, Ian Blumenfeld, Franz-Joseph Decker, Paul Emma, Mark Hogan, Rasmus Ischebeck , Rick Iverson, Devon Johnson, Neil Kirby, Patrick Krejcik, Caolionn O'Connell, Robert Siemann and Dieter Walz from SLAC, David Auerbach, Chris Clayton, Chengkun Huang, Chandrashekhar Joshi, Wei Lu, Kenneth Marsh, Warren Mori and Miaomiao Zhou from UCLA without you this thesis would not be possible. I also would

like to thank the long and hard shift members of the plasma wake field experiment at SLAC, the owl shifters, the day shifters, the swing shifters for making the experiment such a fun learning experience.

I also would like to thank my group mates Suzhi Deng, Bing Feng, Christopher Fenton, Ali Ghalam, Reza Gholizadeh, Efthymios Kallos, Xiaodong Wang from USC for their friendship and for making PhD at USC such a memorable time.

Table of Contents

| | |
|--|-----|
| Dedication | ii |
| Acknowledgments | iii |
| List of Figures | vii |
| Abstract | xiv |
| Chapter 1: Introduction | 1 |
| Chapter 2: Experimental Description of the Plasma Wake Field Accelerator Apparatus | 8 |
| 2.1 Description of Set-up in E-164/E-164X/E-167 Lab at Stanford Linear Accelerator Center | 9 |
| 2.2 Description of the Existing Diagnostics | 12 |
| 2.2.1 Current Transformers (Toroids) | 13 |
| 2.2.2 Optical Transition Radiation (OTR) beam spot size diagnostic | 15 |
| 2.3 Diagnostics for Trapped Particle Research [this thesis work] | 16 |
| 2.4 Cherenkov diagnostic | 16 |
| 2.4.1 Incoming electron beam energy spectrum: Xray diagnostic . | 22 |
| 2.4.2 LiTrack and electron beam current profiles | 24 |
| 2.5 Optical Diagnostics of Plasma and Beam Conditions | 27 |
| Chapter 3: Theory of Plasma and Beam Dynamics | 32 |
| 3.1 Wave breaking | 33 |
| 3.1.1 1 D Cold-nonrelativistic wave breaking limit | 34 |
| 3.2 1-d cold relativistic | 39 |
| 3.2.1 Trapping threshold in a 3D cold relativistic plasma wake in the presence of ionization | 40 |
| 3.2.2 Calculation of the cold relativistic trapping threshold in the presence of ionization in 1-D | 46 |
| 3.3 Dark Current | 49 |

| | |
|--|------------|
| Chapter 4: Experimental Results | 50 |
| 4.1 Evidence for trapped particles and experimental trapping threshold | 51 |
| 4.2 Properties of trapped particles from optical diagnostics | 54 |
| 4.3 Beam loading and origin of trapped particles | 61 |
| 4.4 Energy and charge measurement of trapped particles from Cherenkov diagnostic | 65 |
| Chapter 5: Simulations | 77 |
| 5.1 What are the trapped particles? | 77 |
| 5.2 Trapping threshold | 79 |
| 5.3 Effect of trapped particles on energy gain | 86 |
| Chapter 6: A Brightness Transformer Using a Beam Driven Plasma Wake Field Accelerator | 91 |
| Chapter 7: Future Work | 98 |
| 7.1 An alternative buffer gas | 98 |
| References | 101 |
| Appendices | 105 |
| Appendix A: Derivation of the Constant of Motion | 106 |

List of Figures

| | | |
|-----|--|----|
| 1.1 | 2D simulation of a plasma wave excited by an electron beam; a cartoon surfer represents the location of electrons that surf on the wave. | 1 |
| 1.2 | Plasma Wake Field: (a) Real space of lithium electrons, lithium gas and electron beam showing the formation of the wakefield generated with the simulation code OSIRIS. (b) The same electron and gas real space with a different color map emphasizing the escaping electrons. | 4 |
| 1.3 | Measured longitudinal density of lithium vapor (red circles) and inferred helium gas (blue circles) in the heat- pipe oven for $n_0 = 1.6 \times 10^{17} cm^{-3}$. The gray curve is the maximum radial field of the bunch as it propagates along the plasma. The multiple peaks are due to the periodic oscillations of the beam's transverse envelope in the plasma. The red, blue, magenta and black lines are the field ionization thresholds for Li, He, He ion and Li ion respectively. | 6 |
| 2.1 | Stanford Linear Accelerator Center and the Experimental set-up at the Final Focus Test Beam Facility (FFTB) | 8 |
| 2.2 | Experimental set-up at the Final Focus Test Beam Facility at SLAC | 9 |
| 2.3 | A cartoon of SLAC showing the main sections (not to scale). | 9 |
| 2.4 | Schematic of the heat-pipe oven | 10 |
| 2.5 | ADK ionization rate vs. electric field: (a) For Li. (b) For He. The dashed lines correspond to the threshold ionization rate and field for $\sigma_z = 27 \mu m$ (Eq. 2.3). | 12 |
| 2.6 | Plot of event number vs. charge difference in two toroids located before and after the plasma chamber (with plasma off) | 14 |
| 2.7 | OTR image of the electron beam taken using the Photometrics Sen-Sys 12 bit camera. The yellow line is the vertically summed image | 15 |

| | | |
|------|--|----|
| 2.8 | Cartoon of Cherenkov radiation. | 17 |
| 2.9 | A typical cherenkov image recorded with a ccd camera when the plasma is off and the corresponding energy spectra. | 18 |
| 2.10 | A typical cherenkov image recorded with ccd camera when the plasma is on and the corresponding energy spectra. | 19 |
| 2.11 | Schematic of the Cherenkov energy spectrometer. Two cameras record the light produced in the air gap by the electrons after they exit the plasma and the dipole magnet. In the low dispersion region, light is imaged to the energy loss camera. In the higher dispersion region, light is imaged to the energy gain camera with a larger lens magnification; these images show greater detail of the energy gain. The comparison of these two images also allows for an independent measurement of vertical deflection and energy gain. | 20 |
| 2.12 | Simple illustration of circular trajectory of electrons in the constant B-field of a dipole magnet | 21 |
| 2.13 | Centroid of the electron beam cherenkov image for three different B field settings. | 23 |
| 2.14 | (a) A typical xray spectrometer image. (b) The summed image. . . | 24 |
| 2.15 | A typical output of LiTrack: (a) Horizontal summation of the phase space given in b. (b) The phase space of the electron beam E_0 is the mean energy of electrons 28.5 GeV in this case. (c) Vertical summation of phase space in b. | 26 |
| 2.16 | Experimental lay out in the FFTB. | 27 |
| 2.17 | Light collection set-up I. | 28 |
| 2.18 | Light collection set-up II. | 29 |
| 2.19 | Spex 270 M with Czerny-Turner Mounting, entrance focal length 227.3 mm, and exit focal length 267.84 mm. | 29 |
| 2.20 | Typical plasma light image and its corresponding spectrum obtained with the 150 gr/mm grating. Atomic lines from LiI, LiII, Fe and He are visible. The Fe lines probably originate from iron emitted by the Li heat-pipe oven maintained at a temperature > 900 C. The He lines originate from the excitation of the heat-pipe buffer gas, He at room temperature. | 30 |

| | | |
|-----|--|----|
| 3.1 | An ocean wave breaks and the broken part (the white water) gets trapped in the ocean wave. The largest ocean wave measured was 27.7 m from peak to trough [Pir05]. | 32 |
| 3.2 | Equations that results from the displacement of a sheet of charge by ξ and a cartoon of the displacement. | 37 |
| 3.3 | E/E_{max} vs x for different values of A, $k = 1$ | 38 |
| 3.4 | (a) On-axis wake field, $E_z(c)$. (b) Wake potential Ψ | 44 |
| 3.5 | On axis electric field and the potential Ψ | 45 |
| 4.1 | Picture of the spectrograph and the light collection setup. | 50 |
| 4.2 | (a) A typical image from two independent diagnostics downstream otr camera and the spectrograph. (b) A continuum of light appearing on spectrograph and the down otr camera is being saturated with extra light. | 51 |
| 4.3 | (a) Charge measured after the plasma versus the average energy loss. (b) Relative amount of visible continuum light. Note, the relative fluctuations of the charge below threshold on Fig. 4.3(a) are also present in the incoming charge as measured before the plasma (see Fig. 4.4). The plasma density is $1.6 \times 10^{17} cm^{-3}$ | 52 |
| 4.4 | (a) The charge measured after the plasma (blue circles) and the charge measured before the plasma (red) vs. the average energy loss. | 53 |
| 4.5 | (a) Spectrograph image showing the atomic emission lines (He I, Li I) when there is no trapping. (b) Continuum emission caused by trapped particles on top of emission lines. | 55 |
| 4.6 | (a) Current profile of two bunches: a Gaussian (black line) with rms bunch length of $10 \mu m$ and a non-Gaussian bunch (This is the current profile of a trapped particle bunch, and is taken from simulation done with the particle in cell code OSIRIS) with rms bunch length of $3\mu m$ (red line). (b) The log scale plot of the function $N f(\omega) ^2$. Green shaded area marks the visible spectrum. | 56 |
| 4.7 | (a) Spectrograph image recorded using the spectrograph set-up II showing the interference pattern (modulations). (b) Light intensity versus wavelength, calculated by vertically summing the image over the marked white rectangular region. | 58 |

| | | |
|------|--|----|
| 4.8 | (a) Spectrograph image. (b) Light intensity versus wavelength, calculated by vertically summing the image in (a). | 60 |
| 4.9 | (a) Possible current source for modulations in 4.8: three Gaussian bunches each with a σ_z of $0.1 \mu m$ separated by 2 and $60 \mu m$. (b) The amplitude of the Fourier transform of this current source. | 61 |
| 4.10 | (a) Spectrograph image. (b) Light intensity versus wavelength, calculated by vertically summing the image in (a) | 62 |
| 4.11 | (a) Possible current source for modulations in 4.8: three Gaussian bunches each with a σ_z of $0.1 \mu m$ separated by 4 and $60 \mu m$. (b) The amplitude of the Fourier transform of this current source. | 63 |
| 4.12 | (a) Spectrograph image. (b) Light intensity versus wavelength, calculated by vertically summing the image in (a). | 64 |
| 4.13 | (a) Possible current source for modulations in 4.8: three Gaussian bunches each with a σ_z of $0.1 \mu m$ separated by 9 and $60 \mu m$. (b) The amplitude of the Fourier transform of this current source. | 65 |
| 4.14 | (a) Osiris simulation trapped bunches at the exit of the plasma. (b) The amplitude of the Fourier transform of the bunches. | 66 |
| 4.15 | (a) Current profile of two Gaussian bunches separated by a distance Δz . (b) The amplitude of the Fourier transform of these two bunches. | 67 |
| 4.16 | (a) Xray profiles of the two electron beams. (b) Energy spectrum of the two beams and the trapped particles. (c) Energy spectrum of the two beams and the trapped particles. | 68 |
| 4.17 | Charge measured after the plasma for 7 set of events. Each set represents a different waist position, each set is represented by a different color blue to yellow. Blue represents the set where the waist is located before the plasma source and it is moved further in through each new data set. | 69 |
| 4.18 | Top figure is the energy spectrum of the particles exiting the plasma for $B = 1$ kGauss | 70 |
| 4.19 | Top figure is the energy spectrum of the particles exiting the plasma for $B = 2$ kGauss | 71 |
| 4.20 | Top figure is the energy spectrum of the particles exiting the plasma for $B = 4$ kGauss | 72 |

| | | |
|------|--|----|
| 4.21 | Top figure is the energy spectrum of the particles exiting the plasma for $B = 4$ kGauss | 73 |
| 4.22 | Top figure is the energy spectrum of the particles exiting the plasma for $B = 4$ kGauss the dashed rectangles mark the region of beam and trapped particles, the plots show the number of counts on the whole image and on the marked rectangular regions respectively. | 74 |
| 4.23 | (a) The energy spectrum of the particles exiting the plasma for $B = 1$ kGauss trapped particles blob is centered about 2 GeV. (b) The number of trapped particles for several events. (c) Electron beam counts normalized by the first image counts to 1.8×10^{10} | 75 |
| 4.24 | (a) The energy spectrum of the particles exiting the plasma for $B = 4$ kGauss. (b) Number of trapped particles for several events. (c) Electron beam counts normalized by the first image counts to 1.8×10^{10} | 76 |
| 5.1 | 2-D OSIRIS simulation results with the Li vapor and He gas profiles and density of Fig. 1.3(b). The left panels correspond to Li and the right to He electrons. Figures (a) and (b) are real space densities ($r-z$) at $z = 11.3$ cm (see Fig. 1.3(b)) and (c) and (d) are the corresponding phase space densities ($p_z - z$) at $z = 11.3$ cm and $z = 22$ cm, respectively. The line plot in (c) is the on-axis wakefield E_z . The beam (black line in (a)) has a charge of 1.88×10^{10} electrons, a Gaussian transverse profile with $\sigma_r = 10\mu m$ and a longitudinal profile with $FWHM \approx 65\mu m$ shown by the. The simulation was performed on a moving 500×600 grid ($\Delta z \times \Delta r, 1 \mu m \times 0.5 \mu m$) with 25 beam particles/cell and 1 of each gas atoms/cell. | 78 |
| 5.2 | cartoon of longitudinal density of lithium vapor. The accelerating wake field amplitude W is estimated at the start middle and the top of the ramp | 80 |
| 5.3 | (a) Oven profile used in the simulation (same as Fig. 1.3). Stars indicate the position of the electron beam for the following plots. (b) On axis longitudinal field E_z at three positions: $z=5.85$ cm where density is $n_0/2$ (blue line), $z=11$ cm where density is n_0 (black line), and $z=16$ cm where density is $n_0/2$ (red line). (c) Phase space P_z vs z of the electron beam at the end of the oven | 81 |
| 5.4 | Longitudinal electric field at $\xi = 240\mu m$ (red line) and $\xi = 320\mu m$ (blue line) vs distance in the plasma | 82 |

| | | |
|------|---|----|
| 5.5 | Simulation gas profile used, blue line is the lithium gas and the red line is the helium gas, black line is the same electron beam current that is used in the case of Fig. 5.1 except the peak current is less in the example shown and the beam spot size is made five times smaller to account for the plasma focusing. | 83 |
| 5.6 | Number of trapped He electrons (circles) as a function of the peak accelerating field obtained from simulations with $n_0 = 1.6 \times 10^{17} \text{ cm}^{-3}$, and a bunch charge increasing from 0.4 to 1 times $1.8 \times 10^{10} e^-$. The dashed vertical lines show the trapping threshold (Eq. 3.46) from the values of $k = \frac{dE}{d\xi}$ obtained from the same simulations. Circles and the lines of the same color corresponds to the same simulation. The same current profile as in Fig. 5.1 has been used but $\sigma_r = 2.4 \mu\text{m}$ | 84 |
| 5.7 | (a) Number of trapped electrons along oven (overlaid is the lithium density) (b) Threshold along oven (blue circles), E_{useful} along oven (red circles) | 85 |
| 5.8 | Value of $\Delta\Psi = \Psi_{max} - \Psi_{min}$ (Eq. 3.45) as a function of beam position (red circles). Blue line is the threshold for trapping ($\Delta\Psi = 0.5 mc^2$) | 87 |
| 5.9 | Maximum radial field of a Gaussian bunch is calculated for various beam rms spot size (σ_r) and bunch length (σ_z). The white contour corresponds to the tunneling ionization threshold for various bunch lengths | 88 |
| 5.10 | (a) Real space (r-z) of Li electrons from an Osiris simulation (at a location of the simulation box in the middle of the oven profile Fig. 1.3). (b) The same as (a) except in the simulation there is no He. (c) The real space of He electrons. (d) The blue line is the E_z on axis from the simulation with He, and red line is from the simulation with no He. The inset shows the ratio of peak on-axis field at different r positions | 89 |
| 6.1 | Schematic of the brightness transformer. | 92 |
| 6.2 | Longitudinal density profiles of lithium vapor (blue line) and helium gas (red line) in the plasma source for a vapor and plasma density of $2.7 \times 10^{17} \text{ cm}^{-3}$. At this density the plasma wavelength is of the same order as the bunch length. The pressure is constant along the oven while the Li vapor has a temperature of $\approx 1300 \text{ K}$ and the He gas is at room temperature far from the hot Li vapor. | 93 |

| | | |
|-----|---|-----|
| 6.3 | Simulation results obtained with the 2-D OSIRIS PIC code, using the plasma profile of Fig. 6.2: (a) Longitudinal profile of the drive bunch (pink) and the trapped particles bunch (blue). (b) Energy distribution of the trapped particle bunch at $z = 84$ cm. | 94 |
| 6.4 | OSIRIS simulations with three different drive beams, the gas profiles are the same as in Fig. 6.2 (a) Drive beam and trapped particle current profiles. (b) Energy spectrum of the trapped bunches | 95 |
| 6.5 | OSIRIS simulations with three different drive beams. | 95 |
| 6.6 | Phase space of trapped helium plus electrons from OSIRIS simulation. | 97 |
| 7.1 | Ionization energies of He, Li and Ar. | 99 |
| 7.2 | Simulation results obtained with the 2-D OSIRIS PIC code, using the plasma profile of Fig. 6.2: (a) Longitudinal profile of the drive bunch (blue) and the trapped particles bunch of argon I electrons (red), argon II electrons (black), argon III electrons (yellow)and the combined current profile (green); (b) the corresponding energy distribution of the trapped particle bunches. | 100 |
| A.1 | Partial derivative tree for the variables of interest | 108 |

Abstract

The accelerator at the Stanford Linear Accelerator Center is the world's largest linear accelerator. The electron beam produced here is unique; it is an ultra-relativistic, 28.5 GeV, and ultra-intense (rms bunch length and spot size $\approx 10\text{-}50 \mu\text{m}$) electron beam. Its radial field is so intense that it can field ionize and create a plasma as it traverses a neutral gas. It also creates a very large amplitude (10s of GV/m) plasma wave. When the plasma wave (wake) amplitude is so large, some of the plasma electrons can gain enough forward momentum that they might catch-up with the wave, i.e. get trapped in the wave. This is called wave breaking. Wave breaking has been of fundamental interest for many years and is important in plasma-based accelerators. In the SLAC experiment we observed trapping although 1-D cold relativistic wave breaking theory predicts wave breaking to occur for waves with much higher amplitudes. We attribute this to the uniqueness of the plasma source and field ionization. The plasma source is a heat pipe oven where a hot Lithium (Li) gas is confined at the edges by a helium (He) buffer gas. The plasma wake traps electrons in the He-Li transition regions of the oven. The lithium plasma electrons support the wake, however, the higher ionization potential helium electrons are ionized as the beam is focused by the Li ions and can be trapped inside the wake with a lower wave amplitude.

As the wake amplitude is increased in the experiment, the onset of trapping is observed as a sudden increase both in the total number of electrons leaving the plasma and in the visible radiation they emit. The experimentally inferred trapping threshold is at a wake amplitude of 36 GV/m, and is in good agreement with predictions of an analytical model and detailed particle in cell simulations of the experiment. These electrons are measured to gain 10s of GeV energies and simulations show that these electrons reach energies (>28.5 GeV) exceeding the electron beam driver. Experiments suggest and simulations show that these electrons also form ultra short (a few microns long) bunches. The properties of these trapped electron bunches if optimized can be useful for many applications such as high brightness radiation sources that are used to investigate the properties of molecules in biological cells.

In this thesis, the onset of trapping of electrons that are ionized inside a highly relativistic, three dimensional plasma wake and their properties is investigated with theory simulation and experiment.

Chapter 1

Introduction

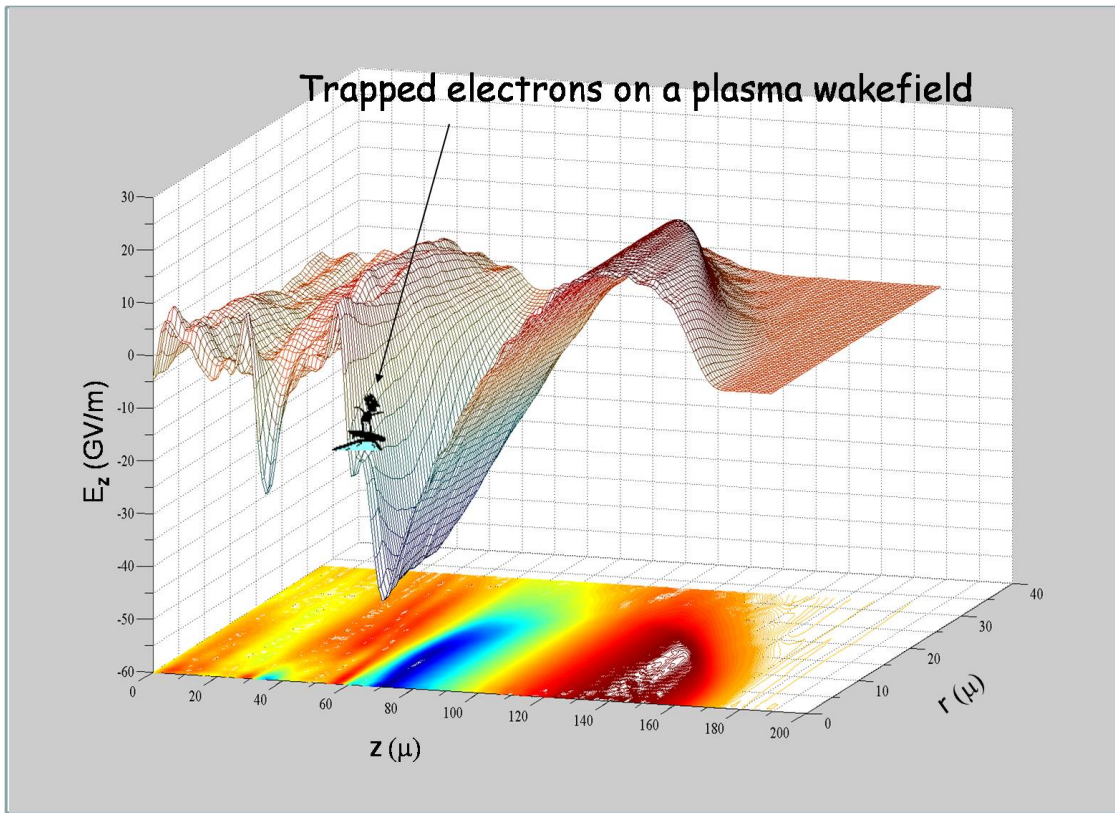


Figure 1.1: 2D simulation of a plasma wave excited by an electron beam; a cartoon surfer represents the location of electrons that surf on the wave.

Accelerators are tools with which the predictions of theoretical physicists about the underlying principles of the nature of the universe are put to test. This is done by studying the collisions of particles. Conventional metallic accelerators use radio frequency waves to accelerate particles and the highest gradients they could produce is about 100 MV/m, making it extremely costly to go to higher energies.

The next linear collider is anticipated to be the international linear collider (ILC) [int] and will be a multi-billion dollar project. It will help answer fundamental questions like how particles acquire mass, what is the structure of space and time and what constitutes the dark matter of the universe by colliding TeV electrons and positron in a 30 km LINAC that will be built using superconducting RF technology.

One of the fundamental limiting factors for highest gradients in conventional accelerators is the dark current. Dark current results from trapping of electrons ionized at the metal surfaces. This has led to active research on plasma accelerating structures that are already ionized and therefore potentially not damaged by the large accelerating fields that they can support. Recent plasma wakefield accelerator experiments driven by lasers or particle beams have successfully accelerated particles at rates of 10-100 GeV/m, several orders of magnitude above the limits set by breakdown in metals. Among these are the experimental programs known as e164, e164X and e167 at the Stanford Linear Accelerator Center conducted by the world's leading research group in plasma wake field accelerators, a collaboration of USC (University of Southern California), UCLA (University of California Los Angeles) and SLAC (Stanford Linear Accelerator Center).

In the latest SLAC experiments, a highly relativistic electron beam propagates through a column of gas, creating a very high gradient plasma wake which is used to accelerate particles in the back of the bunch. In the latest experiment we doubled the energy of a 42 GeV beam over less than a meter of plasma [BCD⁺06]. In addition to record breaking acceleration results we have observed a very interesting phenomena; when the wakefield amplitude is above a threshold value plasma electrons are trapped.

The self-trapping of electrons in plasma waves is a topic of much contemporary interest. Akhiezer and Polovin [AP56] in their seminal paper showed that for one dimensional relativistic plasma waves in a cold plasma with a density n_p fluid theory breaks down when the wave amplitude reaches

$$E_{max} = \sqrt{2(\gamma_\phi - 1)}mc\omega_p/e, \quad (1.1)$$

where $\omega_p = \sqrt{\frac{n_p e^2}{m\epsilon_0}}$ is the plasma frequency and $\gamma_\phi = (1 - v_\phi^2/c^2)^{-1/2}$ and v_ϕ is the wave phase velocity. A physical interpretation of this limit for a non-relativistic plasma wave was given by Dawson in 1959 [Daw59] who associated it with wave breaking and self trapping of plasma electrons due to self steepening of the wave. Calculation of E_{max} in a 1D, warm plasma leads to a small correction to both Dawson's, and Akhiezer and Polovin's results [Cof71, MK90, KM88, Ros88, TN06]. Self-trapped high energy electrons have been routinely observed in experiments on laser driven plasma waves with moderate γ_ϕ [MND⁺95, UKD96, LSE⁺96, JK03]; these experiments were in the self-modulated regime in which the plasma wave grows via an instability until wave breaking and particle trapping occur. In these experiments, the trapping is not deleterious rather it acts as the injector for the accelerator. The wave amplitude is growing from an instability and hence not well determined; it is not possible in those experiments to study the onset of trapping in a very controlled way. Therefore, no systematic study of the onset of the trapping process has been carried out.

Here we use electron beams to create a wake and trap electrons. The advantage to this is that beams evolve more slowly in the plasma and allow the plasma wave amplitude to be controlled via the bunch length and charge. Beam-driven plasma waves have been studied previously by several groups ANL, KEK, ATF

[RSC⁺89, HNN93, YPP⁰³]; however, the wakes generated in those experiments were orders of magnitude too small to reach wave breaking thresholds and the plasma was pre-formed. To reach such high fields we employed the extraordinary power density available from the world's largest linear accelerator, the 3km SLAC linac. The wake is induced by the passage of a short electron bunch through a lithium column confined by helium gas. The wake field amplitude is controlled by varying the peak current of the electron bunch.

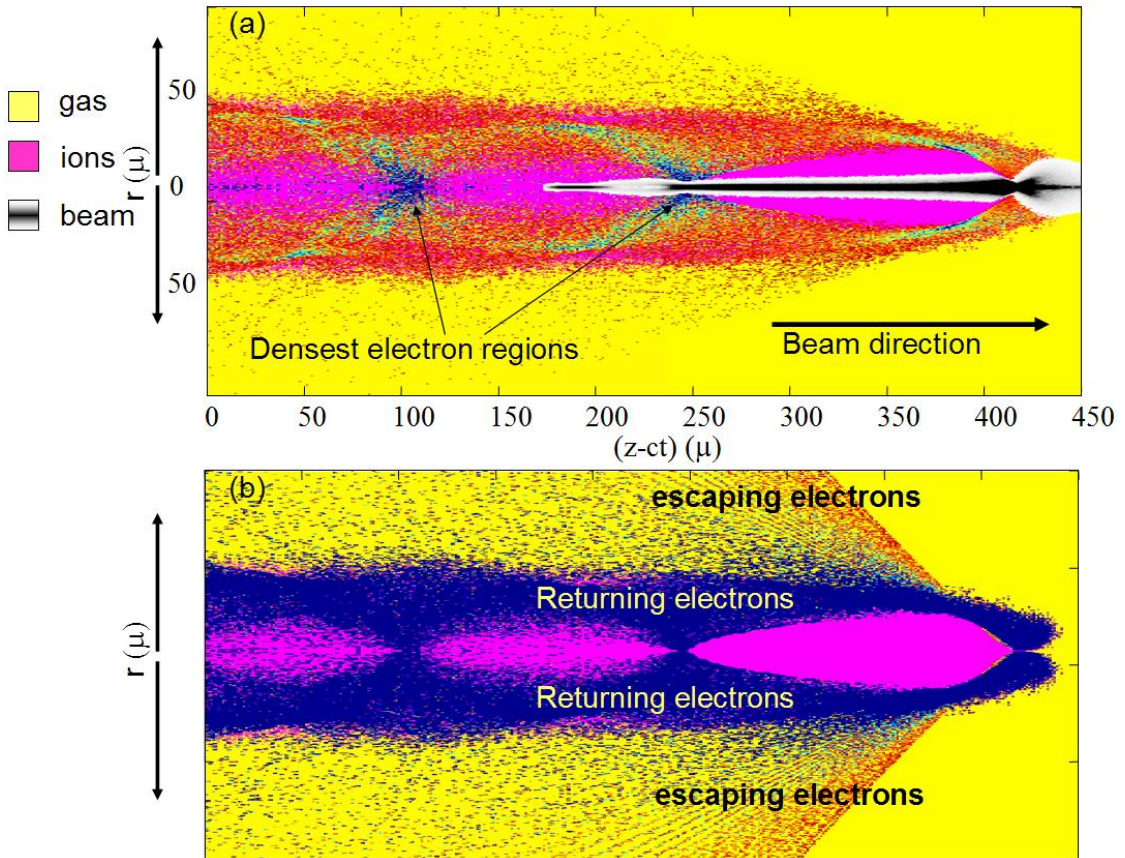


Figure 1.2: Plasma Wake Field: (a) Real space of lithium electrons, lithium gas and electron beam showing the formation of the wakefield generated with the simulation code OSIRIS. (b) The same electron and gas real space with a different color map emphasizing the escaping electrons.

The experiment is carried out in the highly nonlinear or blowout regime of the plasma wake field accelerator (PWFA), in which the focused beam density exceeds the plasma density. As the electron bunch enters the Li vapor, its space charge field first ionizes Li and then expels all the plasma electrons out of the bunch volume (see Fig. 1.2). As a result, a positive plasma ion charge is left behind the head of the bunch and it focuses the beam. In expelling the plasma electrons, the head and core bunch particles lose energy to the plasma wake. The plasma electrons rush back to the beam axis, approximately one plasma period after being expelled. This creates an on axis negative charge spike that can accelerate the electrons in the back of the bunch and also trap plasma electrons. A peak energy gain of about 42 GeV, the largest to date in any plasma accelerator, has been observed in a 85 cm, $2.8 \times 10^{17} \text{ cm}^{-3}$ plasma [BCD⁺06], corresponding to a accelerating gradient of $\approx 50\text{GV}/m$.

As the beam is focused by the plasma ion column to a size smaller than that at the plasma entrance, its space charge field increases as shown in Fig. 1.3 and can become large enough to ionize the first electron of the He buffer gas (24.6 eV ionization potential). This occurs in the He to Li transition regions ($0 < z < 9$ cm and $12 < z < 20$ cm in Fig. 1.3) of the oven where the field exceeds $E_{He} = 70\text{GV}/m$. These newly ionized He electrons are born inside the plasma wake that is supported by the Li electrons, and we show later that they can therefore be trapped and accelerated by the wake. The trapped plasma electrons exit the plasma with the drive bunch and are detected in the form of excess charge and light. We explore a new trapping mechanism: the onset of trapping of electrons that are ionized inside a highly relativistic plasma wave (wake). We show that in the experiment, there is a well-defined threshold for the onset of trapping in an ionizing plasma at a value much lower than that given by Eq. (1.1). A trapping threshold for these

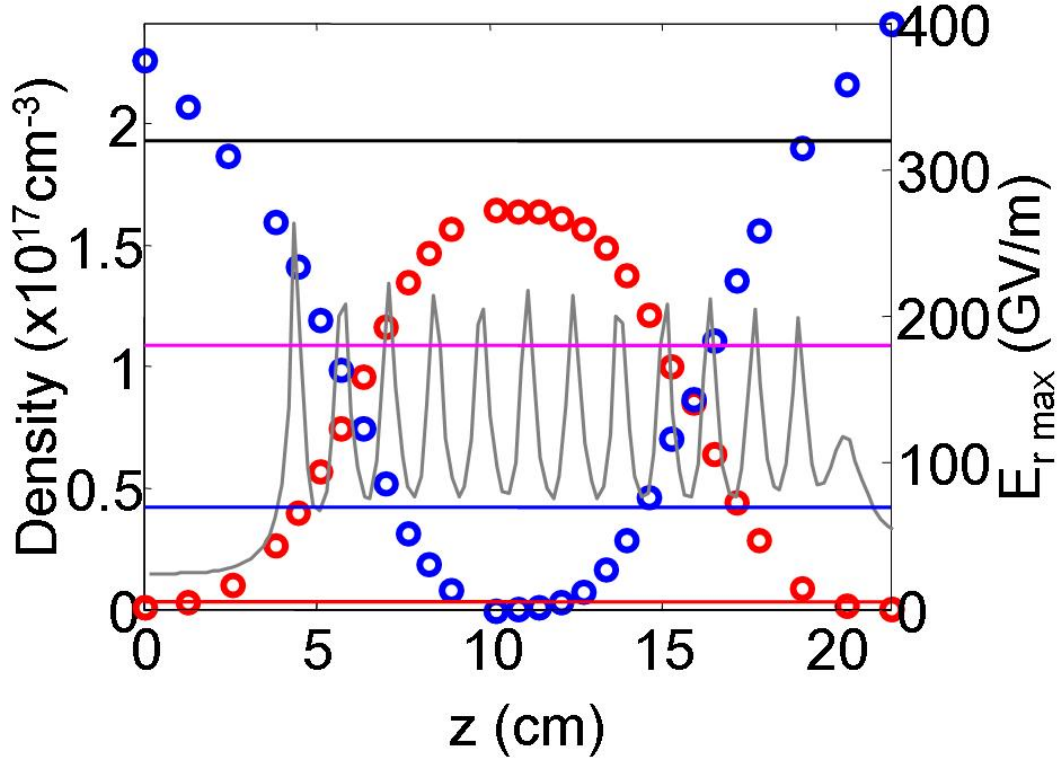


Figure 1.3: Measured longitudinal density of lithium vapor (red circles) and inferred helium gas (blue circles) in the heat- pipe oven for $n_0 = 1.6 \times 10^{17} \text{ cm}^{-3}$. The gray curve is the maximum radial field of the bunch as it propagates along the plasma. The multiple peaks are due to the periodic oscillations of the beam's transverse envelope in the plasma. The red, blue, magenta and black lines are the field ionization thresholds for Li, He, He ion and Li ion respectively.

newly ionized particles is derived and is in excellent agreement with that obtained in numerical simulations and that inferred from the two independent experimental measurements. Experiments also revealed that these particles bunches have very high energies and have ultra short features (2 fs rms bunch length). These unique qualities make them of interest for applications such as making novel light sources. In summary, in this PhD thesis physics of particle trapping in plasma wakefield accelerators is investigated using experiments and detailed full length numerical

simulations. A new analytic model of the particle trapping threshold is presented. Finally it is shown how trapping can be avoided or enhanced depending on the intended use of the PWFA accelerator.

Chapter 2

Experimental Description of the Plasma Wake Field Accelerator Apparatus

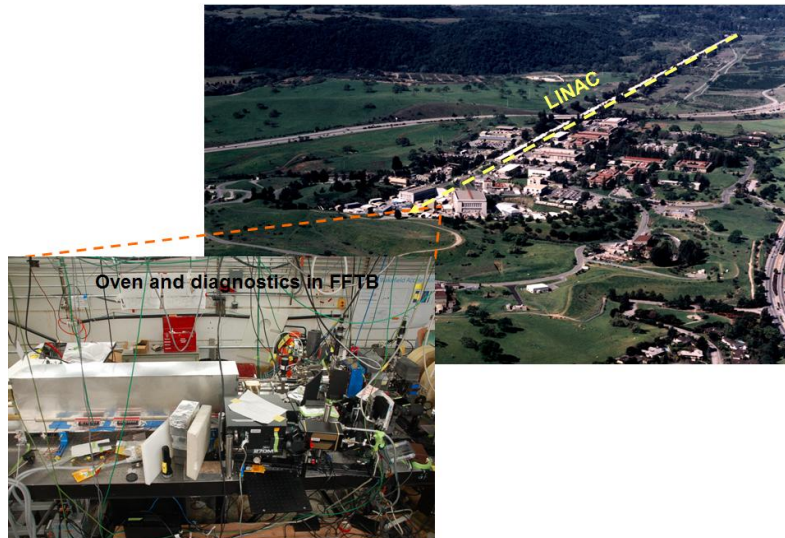


Figure 2.1: Stanford Linear Accelerator Center and the Experimental set-up at the Final Focus Test Beam Facility (FFTB)

The experiments described here were carried out at a plasma wakefield facility built at the Final Focus Test Beam Facility (FFTB) at SLAC. The basic set-up is shown in Fig. 2.2 and was first built in 1999. In this chapter we first describe the SLAC facility and diagnostics prior to this work, followed by new diagnostics and apparatus that were built to carry out this thesis work.

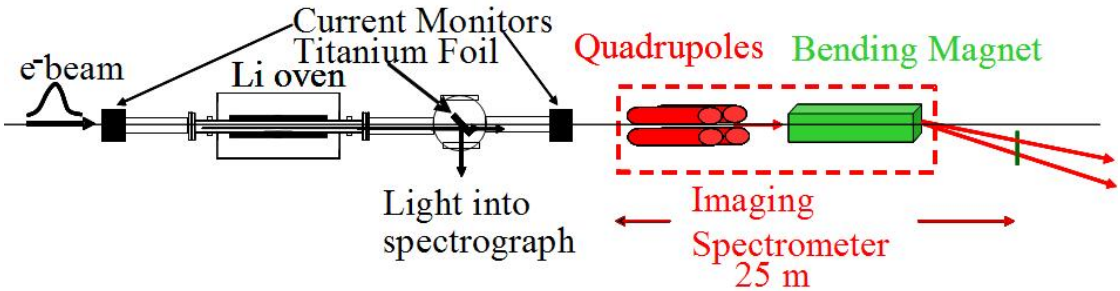


Figure 2.2: Experimental set-up at the Final Focus Test Beam Facility at SLAC

2.1 Description of Set-up in E-164/E-164X/E-167 Lab at Stanford Linear Accelerator Center

With thousands of employees the world's largest linear accelerator SLAC stands as a unique facility (see Fig. 2.1). The main mission of the accelerator is to provide high energy electron and positron beams and collide them for the study of elementary particle physics. The beams from this facility provide a unique driver for the experimental study of plasma wake field physics. The main sections of the

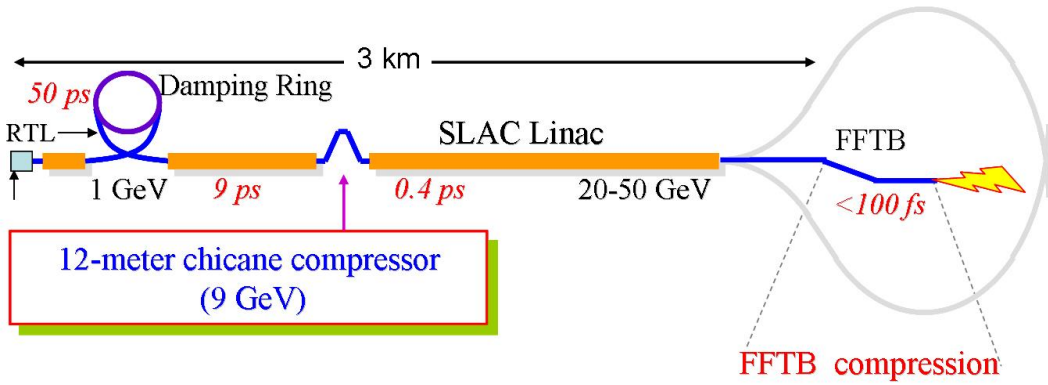


Figure 2.3: A cartoon of SLAC showing the main sections (not to scale).

LINAC that create this unique electron beam is illustrated in Fig. 2.3.

The experiment uses the ultra-relativistic (28.5 GeV) ultra-short (< 100 fs) electron bunches with approximately 1.8×10^{10} electrons available at SLAC. A schematic of the experiment is shown in Fig. 2.2. The electron beam is focused near the entrance of a lithium (Li) vapor of density n_0 contained in a heat-pipe oven [MMW⁺99].

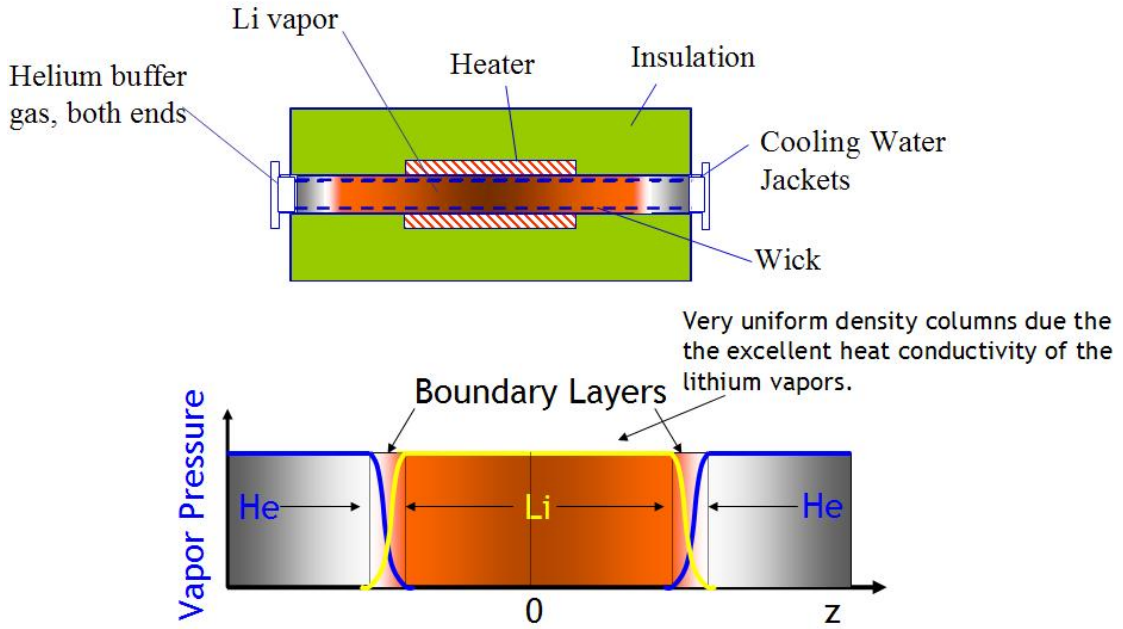


Figure 2.4: Schematic of the heat-pipe oven

The Li is confined to the oven hot region by a helium (He) buffer gas (at room temperature away from the hot region), and the total pressure is constant along the oven (see Fig. 2.4). The gas density is varied in the $0.5 - 3.5 \times 10^{17} \text{ cm}^{-3}$ range by changing the buffer gas pressure. The plasma length is varied in discrete steps by varying the number of oven heaters. The density profile of the Li vapor measured along the oven, as well as the inferred He density are shown in Fig. 1.3 for the case $n_0 = 1.6 \times 10^{17} \text{ cm}^{-3}$, the plasma length is approximately 10 cm

(FWHM). The plasma is created through tunnel ionization [OCD⁺, ADK86] of the low ionization potential (5.39 eV) Li vapor by the large radial space charge field of the bunch once the field exceeds the threshold value of $E_{Li} = 5GV/m$ (calculation of this threshold is explained shortly; this assumes a bunch with 27 μm rms bunch length). The plasma density, n_p is therefore equal to the local neutral Li density (see Fig. 1.3). Note that the plasma off condition is obtained by mechanically moving the lithium oven out of the beam line and replacing it with a helium filled section.

Because of the large radial field of the electron beam driver field ionization is the dominant process in the formation of the plasma. Simulations showed that for current experimental parameter range the impact ionization can be neglected. Field ionization occurs when the infinite atomic potential where the electrons reside changes as a result of the externally applied electric field. The tunneling probability for the atomic electrons can be calculated using the Ammosov-Delone-Krainov (ADK) model [MVAK86, O'C05] which is

$$W \approx 1.54 \times 10^{15} \frac{4^n I[eV]}{n\Gamma(2n)} \left(20.5 \frac{I^{3/2}[eV]}{E \left[\frac{GV}{m} \right]} \right)^{2n-1} \exp \left(-6.83 \frac{I^{3/2}[eV]}{E \left[\frac{GV}{m} \right]} \right) \quad (2.1)$$

W is the ionization rate per second, I is the ionization potential of the desired atomic species, and E is the electric field. The effective principal quantum number is given by $n \approx 3.69 Z / (\sqrt{I} [eV])$ where Z is the ionization state being calculated. $Z = 1$ corresponds to single ionization. Gamma is the usual generalization of the factorial function

The ionization rate is

$$\frac{dn_i}{dt} = W_i n_{i-1} \quad (2.2)$$

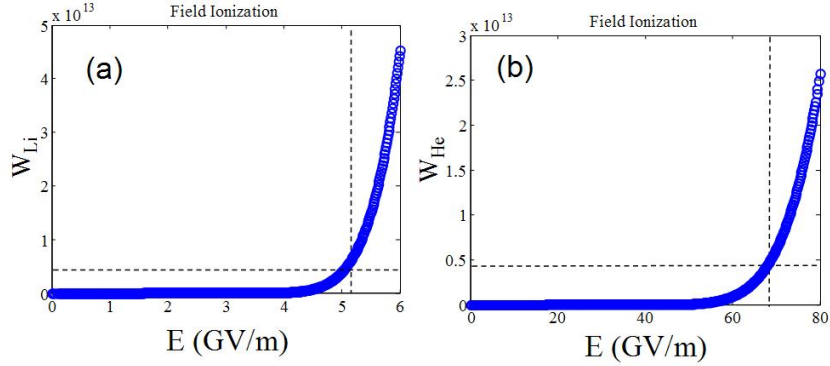


Figure 2.5: ADK ionization rate vs. electric field: (a) For Li. (b) For He. The dashed lines correspond to the threshold ionization rate and field for $\sigma_z = 27 \mu m$ (Eq. 2.3).

where i is the level of ionization, n_0 is the neutral density. Since the tunnel ionization rate is a very steep function of electric field we can define an ionization threshold as follows: $dn = dtWn_0$ full ionization means $dn = n_0$ and dt can be taken as the bunch period divided by speed of the electron bunch [MOM02, B⁺⁹¹] $c/\sqrt{2\pi}\sigma_z$. Therefore

$$\begin{aligned} n_0 &= dtWn_0 \\ 1 &= dtW \\ W &= \frac{c}{\sqrt{2\pi}\sigma_z} \end{aligned} \tag{2.3}$$

using Eq. 2.3 the tunnel ionization threshold field can be read off of the Fig. 2.5

2.2 Description of the Existing Diagnostics

In this section we briefly summarize the experimental diagnostics that existed at the SLAC PWFA facility before this thesis work. These include diagnostics for

beam parameters: Charge, spot size, and energy spectrum of the electron beam before and after the plasma.

The electron bunch charge is measured before and after the plasma using fast current transformers. The visible radiation emitted by the electrons is extracted from the beam line using a $1\mu m$ thick Ti foil at 45 degrees, and is recorded using a charge coupled device (CCD) camera. It is a combination of bremsstrahlung radiation emitted by the particles along the plasma, Cherenkov radiation emitted along the plasma and buffer gas, and transition radiation emitted at the extraction foil. After the plasma, a magnetic spectrometer (see Fig. 2.2) images and disperses the beam to yield single-bunch energy spectra from which we can infer wakefield amplitudes with an accuracy of the order of 1 percent of the incoming beam energy [HBC⁺05].

2.2.1 Current Transformers (Toroids)

One of the factors that determines the wakefield amplitude is the number of electrons in the electron beam. The electron beam charge is measured along the beam line at many locations by current transformers also known as toroids. This is a simple device which consist of a ferrite-core with a wire wrapped around. When the beam passes through the transformer it induces a current; the induced current and beam current are related by the following

$$\int I_{out} dt = \frac{1}{N} \int I_{beam} dt \quad (2.4)$$

where I_{out} is the output current, N is the number of turns on the toroid (8 for the toroid used in the analysis). There are a number of toroids located along the accelerator beam line.

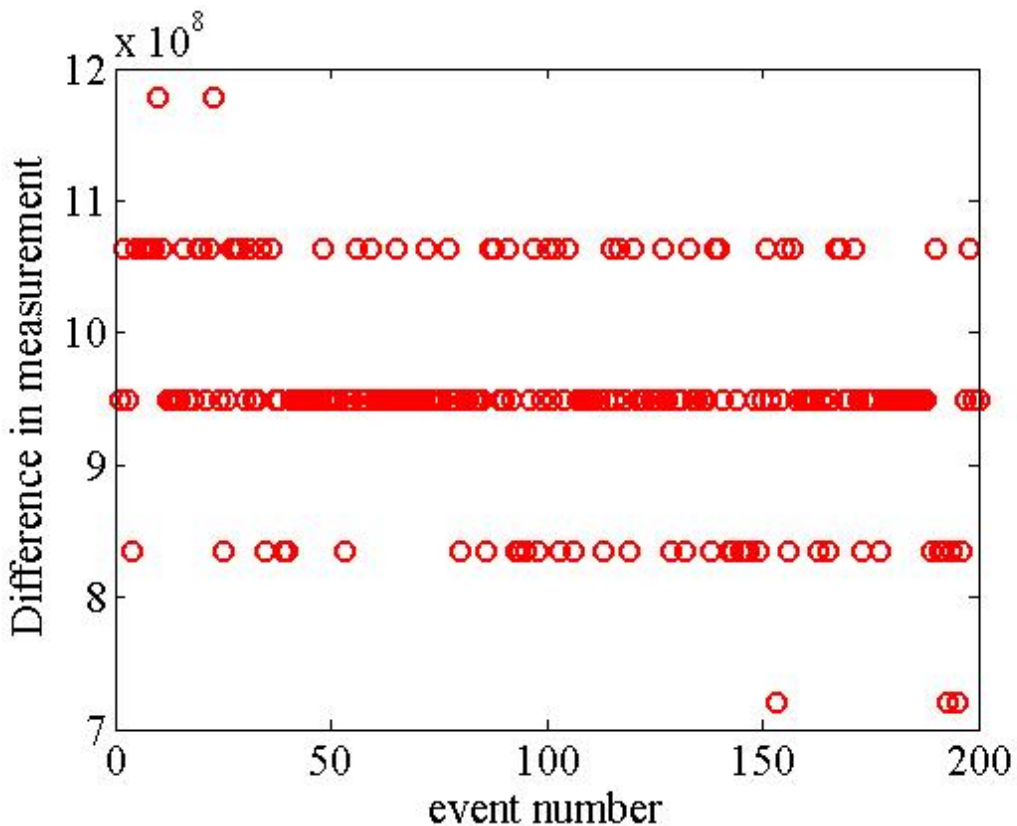


Figure 2.6: Plot of event number vs. charge difference in two toroids located before and after the plasma chamber (with plasma off)

For the current analysis one would like to know the accuracy of the toroid. To get an idea of the sensitivity of the toroids we plot the difference in charge measurement data from the two toroids located before and after the plasma chamber (Fig. 2.6) with the plasma out. The standard deviation of this variation is 8×10^7 . Which is much less than the average charge in the electron beam $\approx 1.8 \times 10^{10}$. Therefore toroids are quite excellent diagnostics to measure the charge.

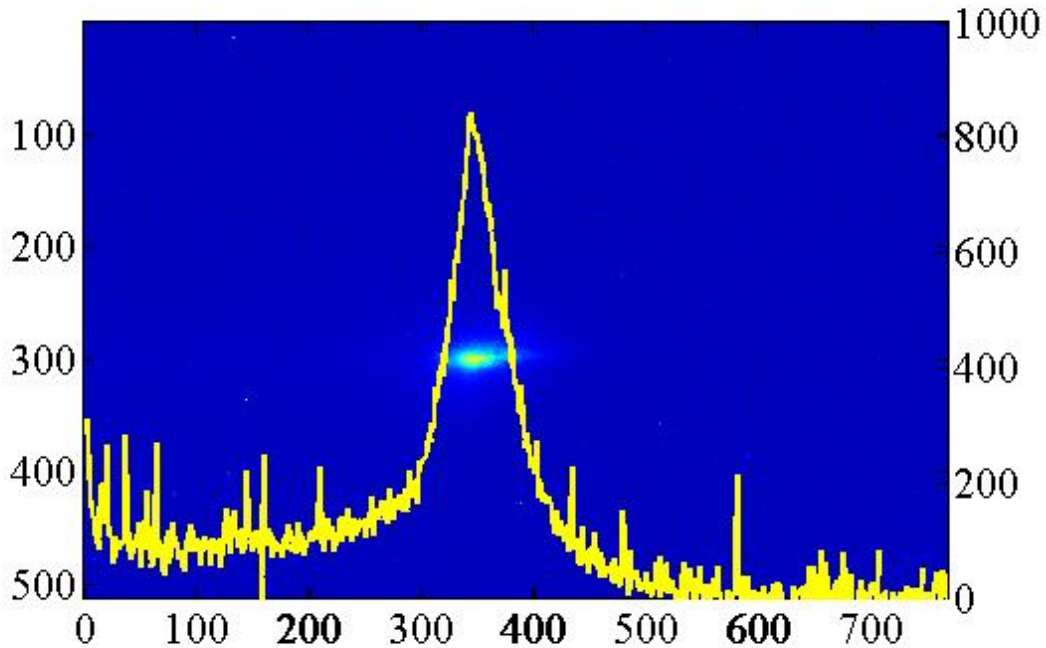


Figure 2.7: OTR image of the electron beam taken using the Photometrics SenSys 12 bit camera. The yellow line is the vertically summed image

2.2.2 Optical Transition Radiation (OTR) beam spot size diagnostic

Transverse spot size of the beam is monitored by recording the optical transition radiation that is produced as a result of passage of the electron beam through a $1 \mu\text{m}$ titanium foil. This diagnostic has a diffraction limited resolution of $5 \mu\text{m}$ [HAD⁺⁰⁰]. A typical image is shown in Fig. 2.7

2.3 Diagnostics for Trapped Particle Research

[this thesis work]

To carry out this thesis research several new diagnostics were implemented at the PWFA facility. These increase our understanding of the plasma and beam physics and enable detection and characterization of trapped particles. These are a Cherenkov energy spectrometer to measure the energy change of the electron beam by the plasma as well as the energy of the trapped particles; an Xray energy spectrometer to measure the incoming energy spectrum of the electron beam; and a spectrograph to diagnose the beam, trapped particles and plasma conditions.

2.4 Cherenkov diagnostic

Čerenkov (Chrenkov) radiation is produced when a particle exceeds the speed of light in a medium (i.e. $\frac{c}{n}$, $c = 299792458$ m/s is the speed of light in vacuum). As the particle travels in the medium the medium is excited and the radiation is emitted at each point (and travels in the medium with c/n) but until the particle reaches c/n these waves cannot form a wave front. Once particle reaches or goes above c/n wavelets constructively superpose and a wavefront (i.e. Čerenkov radiation) is formed (see Fig. 2.8). The angle of Čerenkov radiation for a particle traveling at a speed $v \approx c$ is given by

$$\cos\theta = \frac{1}{n} \quad (2.5)$$

In the case of interest here, Čerenkov radiation emitted when an electron passes through a gas in our experimental apparatus. This could be either neutral Li or He in the oven or He in a special cell added for diagnostics purposes. In this case

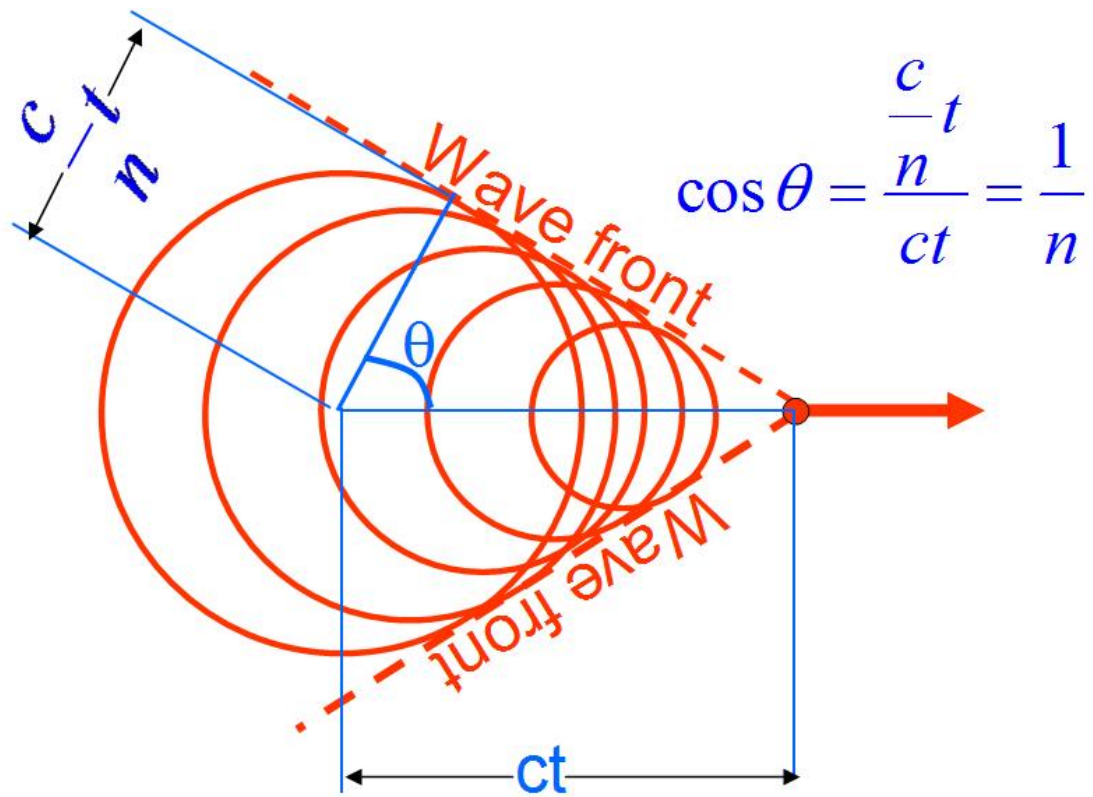


Figure 2.8: Cartoon of Cherenkov radiation.

n is a function of gas pressure, $n - 1 \propto P$. At standard temperature and pressure $n - 1 = 3.3 \times 10^{-5}$ for He.

In the experiment we built a magnetic spectrometer which images and disperses the beam to yield single-bunch energy spectra from which we can infer wakefield amplitudes with an accuracy of the order of 1 percent of the incoming beam energy [HBC⁺05]. Figures 2.9 and 2.10 show typical cherenkov images when the plasma is off and on respectively.

Later in the experiments the oven length was increased up to 120 cm. As a result of the longer plasma length, much larger energy change of the incoming electron beam made it impossible to transport the electron beam through the

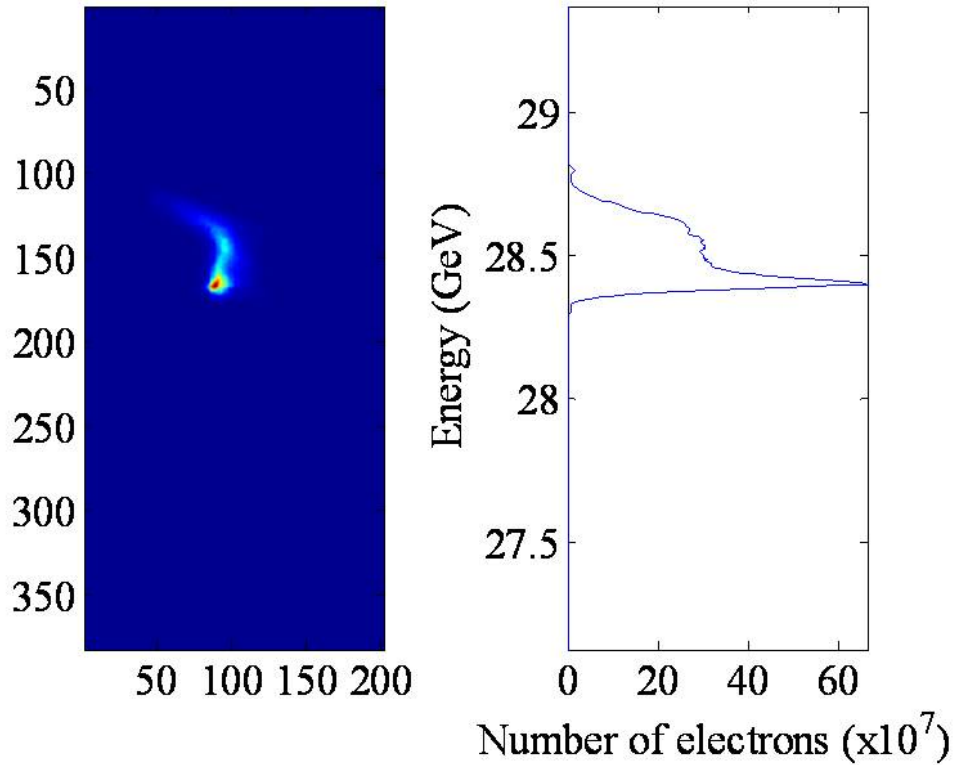


Figure 2.9: A typical cherenkov image recorded with a ccd camera when the plasma is off and the corresponding energy spectra.

imaging spectrometer. Hence, a new powerful dipole magnet was placed closer to the plasma exit and the energy change of the incoming electron beam by plasma was monitored by recording the Cherenkov radiation produced in the air at two locations. At one location (see Fig. 2.11) the imaging system was adjusted to look at the energy loss of the electron beam; at the second location the imaging system was adjusted to look at the energy gain of the electron beam. The measurement of the electron beam energy change at two locations also enabled the measurement of the vertical deflection of the electron beam caused by the plasma.

Cherenkov images obtained in this set-up can be calibrated as follows:

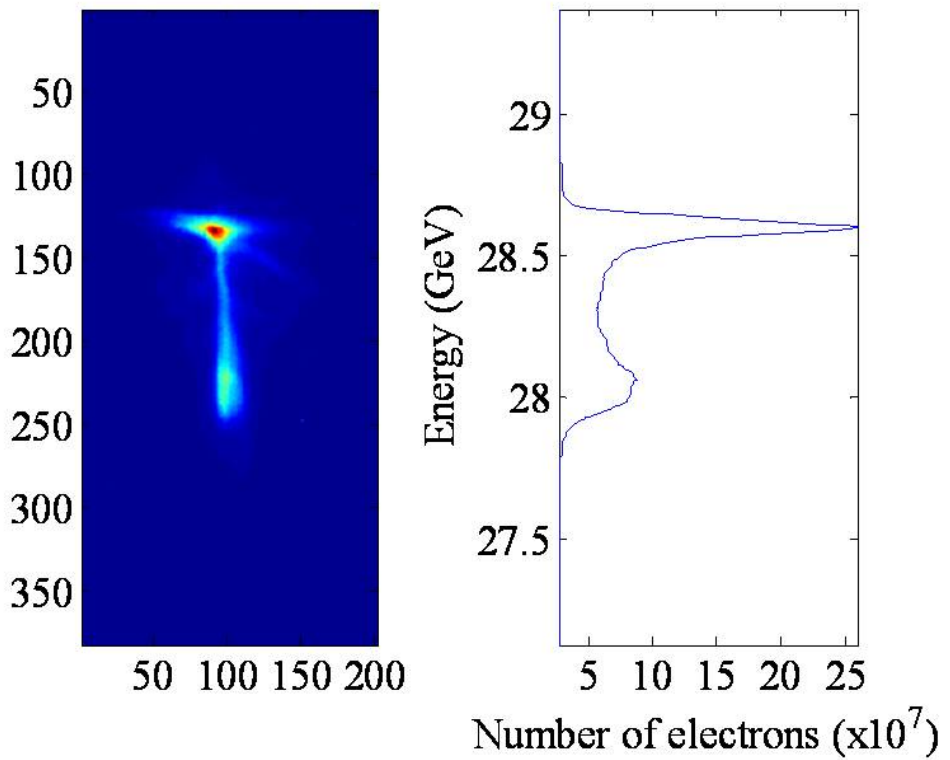


Figure 2.10: A typical cherenkov image recorded with ccd camera when the plasma is on and the corresponding energy spectra.

$$\gamma \frac{mV^2}{R} = eVB \quad (2.6)$$

$$V \approx c \text{ where } c \text{ is the speed of light} \quad (2.7)$$

$$R = \gamma \frac{mc}{eB} \quad (2.8)$$

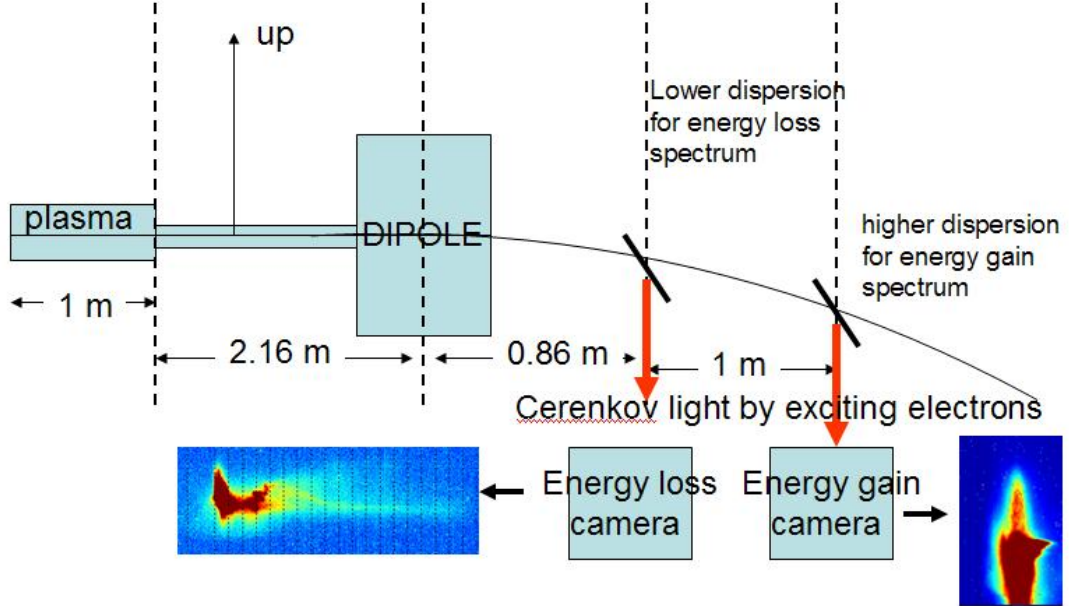


Figure 2.11: Schematic of the Cherenkov energy spectrometer. Two cameras record the light produced in the air gap by the electrons after they exit the plasma and the dipole magnet. In the low dispersion region, light is imaged to the energy loss camera. In the higher dispersion region, light is imaged to the energy gain camera with a larger lens magnification; these images show greater detail of the energy gain. The comparison of these two images also allows for an independent measurement of vertical deflection and energy gain.

Using the equation of a circle, (For the coordinate system of choice see Fig. 2.12)

$$x^2 + (y + R)^2 = R^2 \quad (2.9)$$

$$y = \sqrt{R^2 - x^2} - R$$

$$x = L$$

$$y = \sqrt{R^2 - L^2} - R$$

$$y = R\sqrt{1 - \left(\frac{L}{R}\right)^2} - R$$

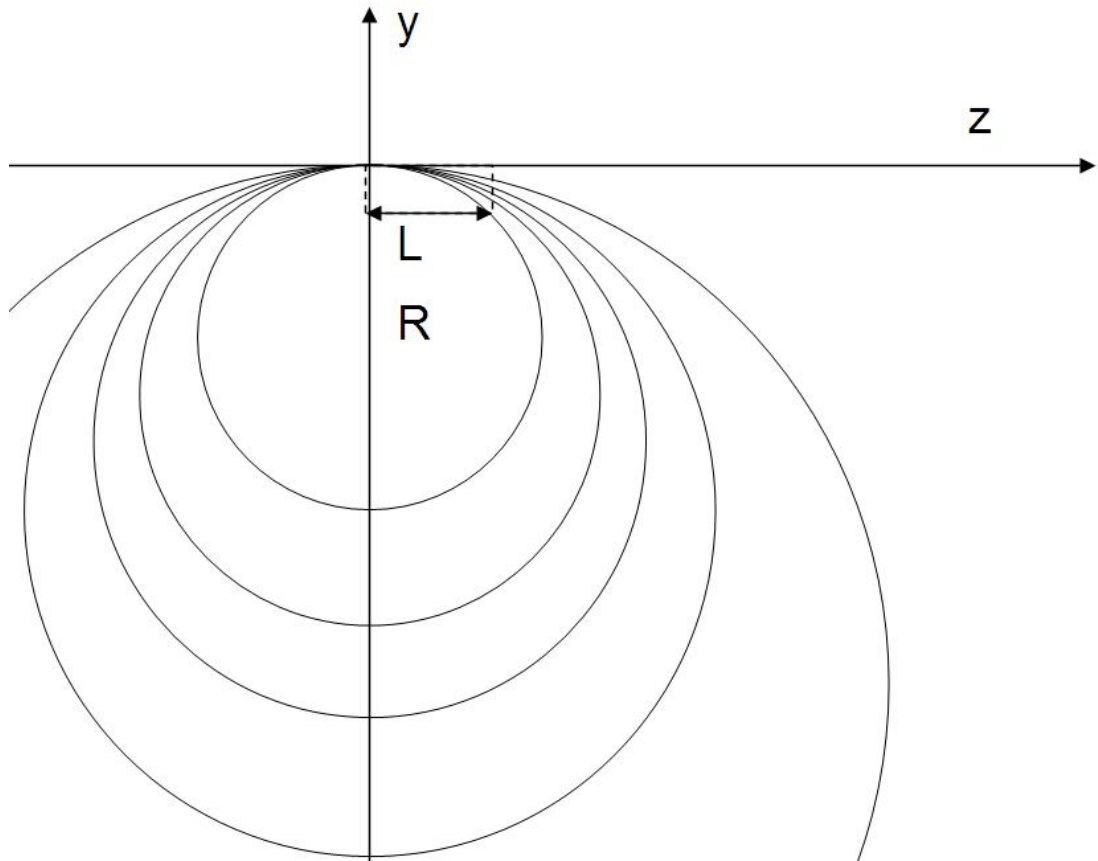


Figure 2.12: Simple illustration of circular trajectory of electrons in the constant B-field of a dipole magnet

Taylor expand the expression in the square root to get

$$\begin{aligned}
 \frac{y}{R} &= 1 - \frac{1}{2} \left(\frac{L}{R} \right)^2 - 1 \\
 \frac{y}{R} &= -\frac{1}{2} \left(\frac{L}{R} \right)^2 \\
 y &= -\frac{L^2}{2R} \\
 y &= -\frac{eBL^2}{2\gamma mc}
 \end{aligned} \tag{2.10}$$

Therefore we can simply write

$$E = \frac{A}{y - yb0} \quad (2.11)$$

where E is energy, $yb0$ is the position of the beam when $B = 0$, and A is a constant.

$$28.5 = \frac{A}{y0 - yb0} \quad (2.12)$$

$$E = \frac{A}{y - yb0} \text{ therefore} \quad (2.13)$$

$$E = 28.5 \frac{y0 - yb0}{y - yb0} \quad (2.14)$$

where $y0$ is the position of the beam when B is on.

To be able to get the constants for the energy calibration we look at three different B field settings when the plasma is off. B field vs. centroid of the beam is linear; therefore, when we interpolate the line to $B = 0$ we will get the first constant, $yb0$. The second constant $y0$ comes from the location of the beam centroid when the B field is at the value of interest.

Figure 2.13 is a plot of centroid for three different B field settings, the slope is $y = 12B + 14$. For $B=0$ the location of the centroid is therefore 14.

2.4.1 Incoming electron beam energy spectrum: Xray diagnostic

Since the incoming electron beam has energy spread it is important to know the incoming energy spectrum to be able to determine the energy change of an electron. This is critical for the case of a short plasma (≈ 10 cm long) where the energy change is on the order of energy spread. The diagnostic for measuring the incoming energy spectrum is an Xray spectrometer [Bar05]. Xray spectrometer consists

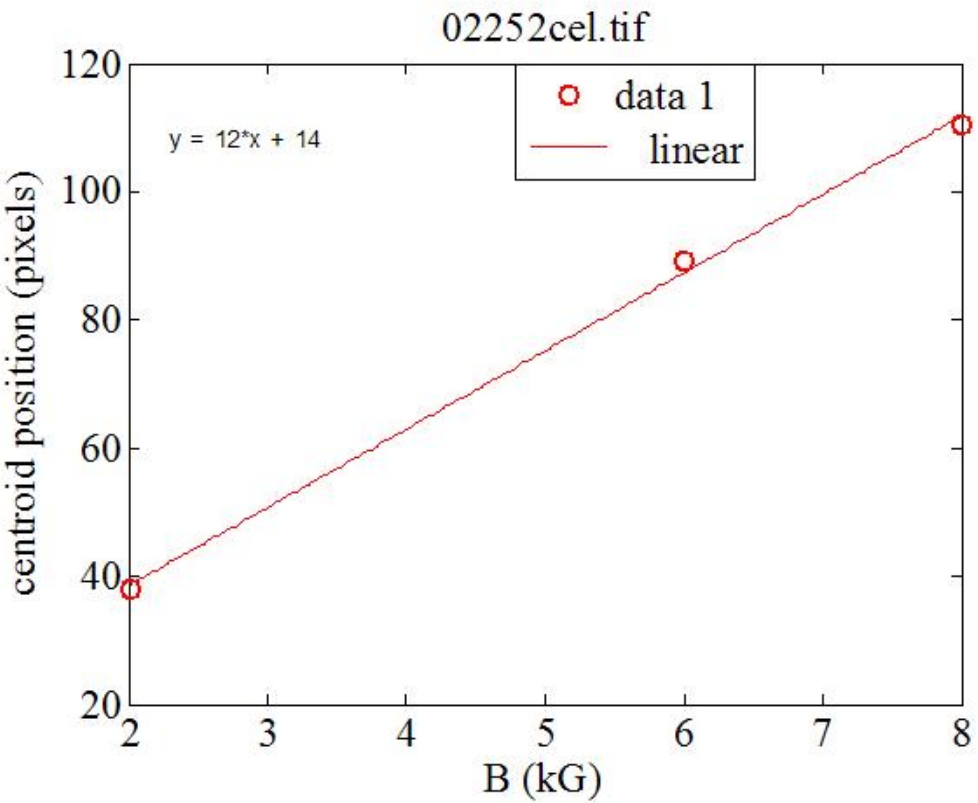


Figure 2.13: Centroid of the electron beam cherenkov image for three different B field settings.

of a wiggler magnet and a Ce:YAG scintillating crystal. As the electron beam traverses the wiggler which is a series of dipoles whose polarity is switched to wiggle the electrons, the wiggling electrons radiate X-rays. These X-rays create visible photons when they hit the crystal, the light is recorded with a CCD (Charge Coupled Device) camera. Figure 2.14 shows a typical image.

Knowing the energy spectrum by itself is not enough since energy spectrum does not contain the position of the particle. The position of the particle determines whether it will lose or gain energy. Hence we need the phase space of the electrons (Energy vs. position). However there is no direct way of measuring the phase space

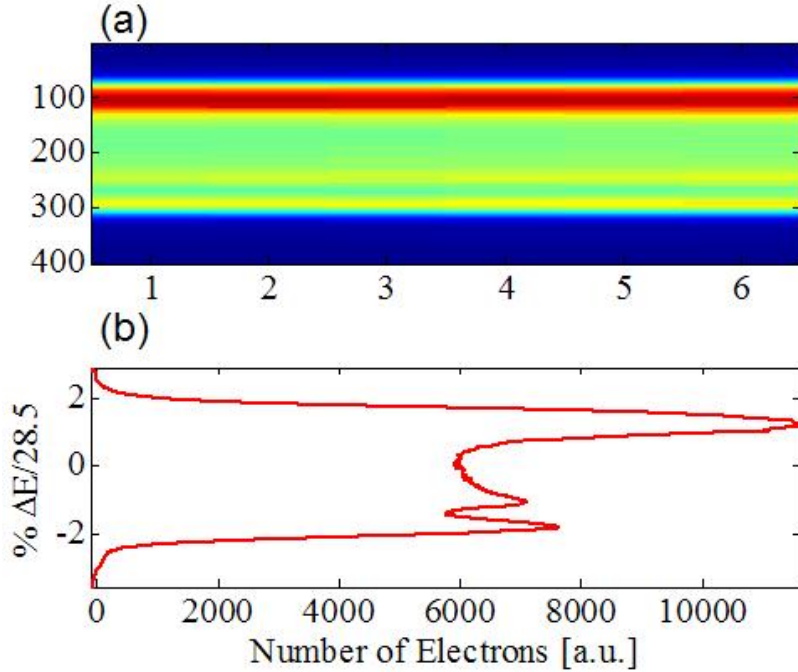


Figure 2.14: (a) A typical x-ray spectrometer image. (b) The summed image.

of such ultrarelativistic electron beam. Fortunately though there is an indirect way to reveal this information using the incoming energy spectrum which will be explained in the next section.

2.4.2 LiTrack and electron beam current profiles

There is no direct way of measuring the longitudinal profile of the electron beam on a shot to shot (each passage of the electron beam is called a shot in the experimentalists lingo) basis because it is extremely short (rms bunch length of 30 fs to 300 fs) although we did investigate a method proposed by Max Zolotrev [MSZ96] using the statistical fluctuations of the incoherent transition radiation of the beam in the visible spectrum. The longitudinal profile of the beam determines the amplitude of the wake field at a constant plasma density, therefore it is extremely important.

We chose to use an indirect method of determining the profile of the beam. This is done using the incoming energy spectrum of the beam and reproducing this through a linac simulation code LiTrack [PE05] written in Matlab.

Knowing the parameters of the Stanford Linear Accelerator which includes hundreds of magnets their strengths, dimensions, the initial condition of the electron beam, and the magnitude of the radio frequency waves everywhere, one can calculate the 3-d phase space (P_x, P_y, P_z, x, y, z) of the electron beam right before it enters the plasma. The simulation code ELEGANT [Bor00] has this capability but running a single simulation takes many hours. Since in the experiment some of these parameters constantly fluctuate causing the electron beam profile to vary from shot to shot, to be able to figure out the incoming profile one needs a pool of simulations. Then one can match the measured energy spectrum to the simulation pool and determine the phase space of the electron beam. Fortunately it turns out that the transverse and longitudinal dynamics of this highly relativistic electron beam can be assumed independent as was confirmed by comparison between the 1-D (LiTrack) and the 3-D models (Elegant). This simplifies the problem, down to only 10s of parameters which are simulated using LiTrack. A single simulation takes only a few seconds. Therefore creating almost every possible configuration in a reasonable sampling of the accelerator and beam parameters is possible.

Figure 2.15 shows a typical LiTrack output. The longitudinal phase space is given in b. By summing the phase space vertically or horizontally we get figures c and b, respectively. The longitudinal current profile is what determines the plasma wake field. Experimentally we measure the energy spectrum which corresponds to (a). Our method assumes that each xray profile has a uniquely associated longitudinal profile of the electron beam and that therefore finding a simulation spectrum which is the same as the experimental energy spectrum determines the

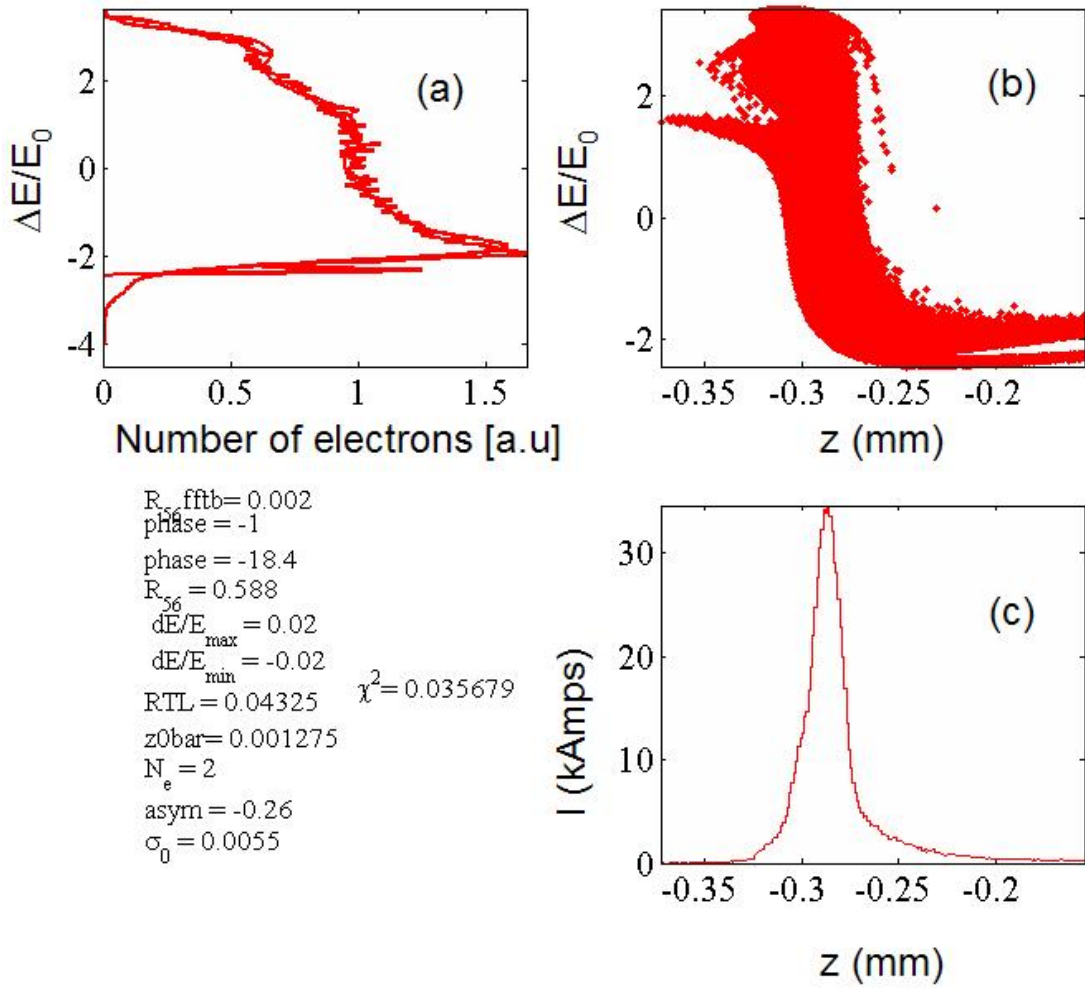


Figure 2.15: A typical output of LiTrack: (a) Horizontal summation of the phase space given in b. (b) The phase space of the electron beam E_0 is the mean energy of electrons 28.5 GeV in this case. (c) Vertical summation of phase space in b.

longitudinal profile. Although we do not rigorously prove this assumption, it appears to be born out by hundreds of linac configurations we have simulated.

2.5 Optical Diagnostics of Plasma and Beam Conditions

Light emission from the plasma is rich with information about the plasma as well as the properties of the beams passing through it.

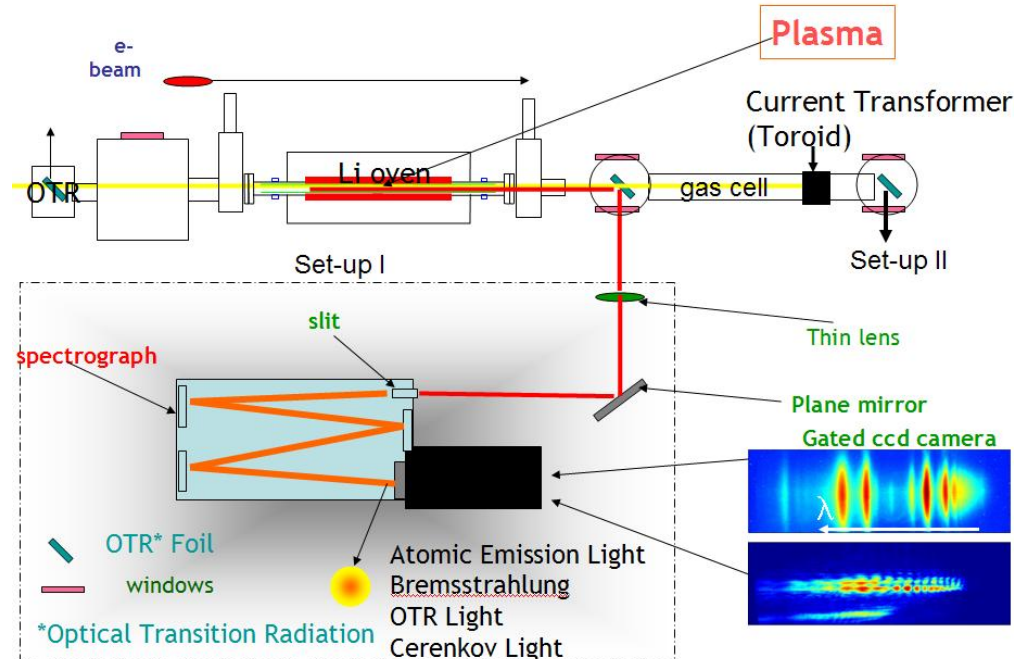


Figure 2.16: Experimental lay out in the FFTB.

Figure 2.16 shows the spectrograph set-up to collect the plasma light. The details of the two different optical collection set-ups are shown in Figs. 2.17 and 2.18. Setup-II enabled us to vary the helium pressure inside the gas cell therefore enhancing or zeroing out the Cherenkov radiation and look at the only OTR radiation. In case of setup-I we used one or two lenses to change the light collection spot.

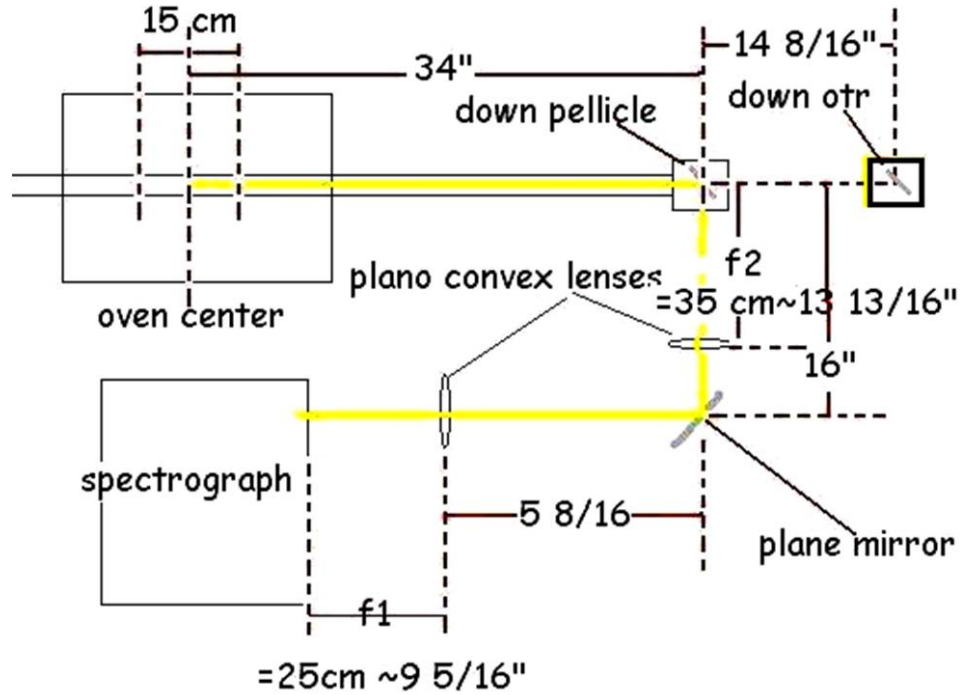


Figure 2.17: Light collection set-up I.

The plasma light is directed towards and focused onto the slit of a 27 cm focal length imaging optical spectrograph 2.19. A gated intensified camera with 1024×256 , $27 \mu\text{m}$ square pixel is placed in the image plane of the spectrograph.

The gated camera can be adjusted to look at different times after and during the interaction; the gate can be as narrow as five nano seconds. Since the plasma beam interaction only lasts for a couple of nano seconds, when the gate is adjusted to 5ns, the emission light from neutral lines is negligible. This enables us to separate emission light from beam light.

The resolution of the spectrograph is 2.5 nm with a 150 gr/mm grating blazed at 560 nm, and 0.3 nm with a 1200 gr/mm grating blazed at 500 nm. The low dispersion grating is used to monitor the entire visible spectrum, while the higher dispersion grating is used to monitor the width of individual atomic/ionic lines.

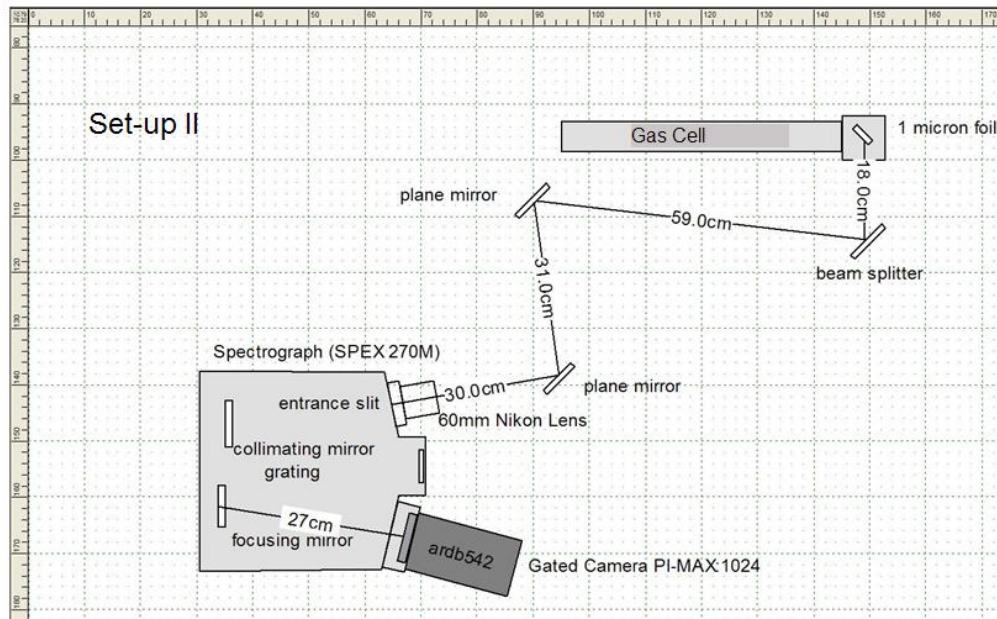


Figure 2.18: Light collection set-up II.

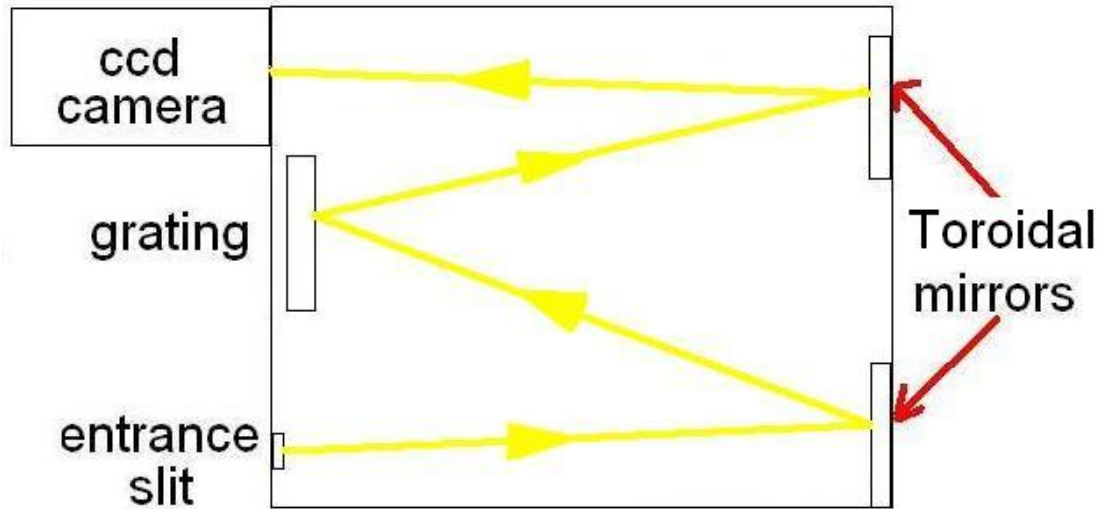


Figure 2.19: Spex 270 M with Czerny-Turner Mounting, entrance focal length 227.3 mm, and exit focal length 267.84 mm.

Figure 2.20 shows a typical plasma light image dispersed in wavelength, as well as the corresponding energy spectrum obtained by summing the image along its

vertical dimension. The plasma light spectrum is composed of atomic lines from the different atoms present in the heat-pipe oven (Li, He, Fe).

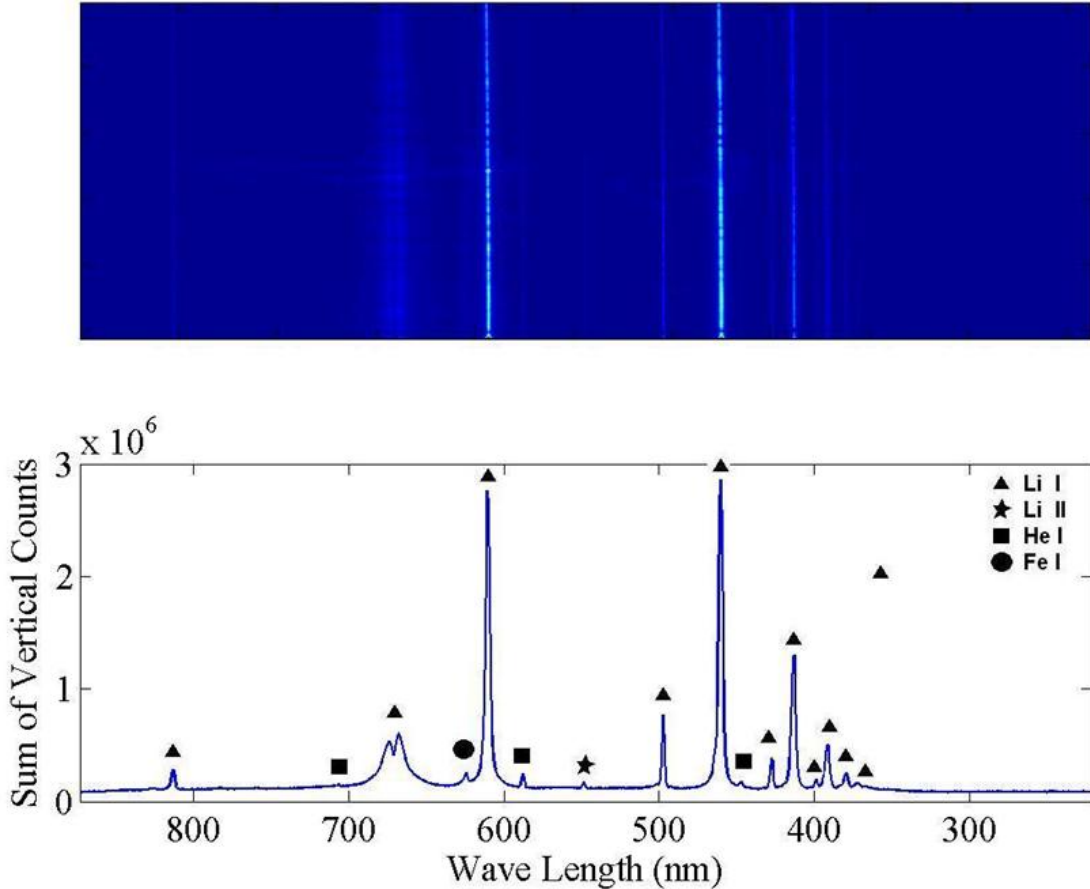


Figure 2.20: Typical plasma light image and its corresponding spectrum obtained with the 150 gr/mm grating. Atomic lines from LiI, LiII, Fe and He are visible. The Fe lines probably originate from iron emitted by the Li heat-pipe oven maintained at a temperature > 900 C. The He lines originate from the excitation of the heat-pipe buffer gas, He at room temperature.

The wavelength calibration is obtained using the known atomic lines of a spectral lamp. The well known grating equation for the condition of a maximum is

$$m\lambda = d(\sin(\theta) + \sin(\theta')) \quad (2.15)$$

where m is called the order number, θ' and θ are the angles of incidence and reflection angles, and d is the grating groove distance of the grating. The grating equation near Littrow mode (defined as the incidence angle is equal to diffraction angle) can be used to express the dispersion

$$\frac{d\lambda}{dl} = \frac{2f}{\sqrt{4d^2 - \lambda^2}} \quad (2.16)$$

where f is the focal length of spectrograph (in our case exit focal length). This tells us that for $\frac{\lambda^2}{4d} \ll 1$ we have a simple relation relating the dl to $d\lambda$ independent of λ . Therefore plotting the location of a known line on the chip vs. the wavelength of the line can be used to convert the pixel location to real wavelength.

Chapter 3

Theory of Plasma and Beam Dynamics

In this chapter, physics of wave breaking and a theoretical prediction of particle trapping thresholds will be presented.



Figure 3.1: An ocean wave breaks and the broken part (the white water) gets trapped in the ocean wave. The largest ocean wave measured was 27.7 m from peak to trough [Pir05].

3.1 Wave breaking

The limiting amplitude of relativistic cold plasma waves in one-dimension was given by Akhiezer and Polovin in 1956. In their derivation the maximum amplitude of the plasma wave corresponds to a singularity in the plasma density ($n = \infty$). Dawson in 1959 derived the wave breaking condition for cold non-relativistic waves and his derivation provided a physical interpretation for wave breaking. Namely wave breaking occurs when neighboring plasma wave sheets cross causing mixing of the phases of electrons. When the wave breaks the electrons that are phase mixed can be accelerated and gain energy beyond that provided by the plasma oscillation. This is called trapping¹. A similar phenomena occurs when an ocean wave breaks, the white water is caught in the wave and accelerated by the wave (see 3.1). In section 3.1, we review the prior 1D results on plasma wave breaking, and in section 3.2 we extend the model to 3D waves under certain conditions.

¹The definition of trapping has not been consistently applied throughout the literature. In some formal definitions and in particular non-relativistic ones, trapping has been defined as a particle reaching $v = v_\phi$. However, for very relativistic waves, an electron can surf for long distances, gaining many GeV but not necessarily exceeding v_ϕ in speed or $\gamma_\phi = 1/\sqrt{1 - \frac{v_\phi^2}{c^2}}$ in energy. We consider such a particle to be effectively trapped even though $v < v_\phi$ so long as $\gamma - 1$ of the particle is much larger than the kinetic energy associated with oscillating in the wave.

3.1.1 1 D Cold-nonrelativistic wave breaking limit

We start with the Eulerian equation of motion for a Eulerian fluid element and Maxwell's equations (cgs). From there we develop the appropriate equations for a Lagrangian fluid [MK90] The Euler and Maxwell's equations we use are

$$\left(\frac{\partial}{\partial t} + v \frac{\partial}{\partial x} \right) v = -eE/m \quad (3.1)$$

$$\nabla \times \mathbf{H} = \frac{4\pi}{c} \mathbf{J} + \frac{1}{c} \frac{\partial \mathbf{D}}{\partial t} \quad (3.2)$$

$$\frac{\partial E}{\partial x} = 4\pi e(n_0 - n) \quad (3.3)$$

We include the plasma electrons and ions as free charges in the equations hence

$$D = \epsilon E \text{ and } \epsilon = 1 \quad (3.4)$$

In 1D $H = 0$. Therefore equation 3.2 becomes

$$\frac{\partial E}{\partial t} = -4\pi J \quad (3.5)$$

with $J = -nev$ Equation 3.3 becomes

$$\frac{\partial E}{\partial t} = 4\pi nev \quad (3.6)$$

Substituting for n from 3.3 into 3.6 gives

$$\frac{\partial E}{\partial t} = 4\pi ev \left(\frac{-1}{4\pi e} \frac{\partial E}{\partial x} + n_0 \right)$$

Note that

$$\frac{\partial E}{\partial t} + v \frac{\partial E}{\partial x} = \frac{dE}{dt} \quad (3.7)$$

thus

$$\frac{dE}{dt} = 4\pi e n_0 v \quad (3.8)$$

$$E = 4\pi e n_0 \int v dt \quad (3.9)$$

Integrating with respect to t and using the fact that

$$v = \frac{d\xi}{dt} \quad (3.10)$$

where v is the velocity of the eulerian fluid element and ξ is the displacement of a Lagrangian fluid element given by $x = x_0 + \xi$ gives

$$E = 4\pi e n_0 \xi \quad (3.11)$$

Using this we can write

$$\frac{\partial E}{\partial x} = 4\pi e n_0 \frac{\partial \xi}{\partial x} \quad (3.12)$$

and substituting into Eq. (3.3) (Gauss's law) gives

$$n = n_0 \left(1 - \frac{\partial \xi}{\partial x}\right) \quad (3.13)$$

Substituting for $\frac{\partial}{\partial x}$ using the following relation

$$\frac{\partial}{\partial x} = \frac{1}{1 + \frac{\partial \xi}{\partial x_0}} \frac{\partial}{\partial x_0} \quad (3.14)$$

we obtain

$$n = \frac{n_0}{1 + \frac{\partial \xi}{\partial x_0}} \quad (3.15)$$

this means when

$$\frac{\partial \xi}{\partial x_0} = -1 \quad (3.16)$$

the density will be infinite. Using 3.1 and 3.10 we can write

$$\frac{d^2 \xi}{dt^2} = -eE \quad (3.17)$$

substituting E from 3.11 we obtain

$$\frac{d^2 \xi}{dt^2} + \omega_p^2 \xi = 0 \quad (3.18)$$

using these we can derive the wave breaking amplitude.

The same wave breaking amplitude is derived by Dawson using a physical sheet model as follows.

Figure 3.2 helps explain how the equations for displacement of sheet of charge are derived. Dawson in 1959 derived the equations for electrons (sheets) in 1-D using this simple picture: Imagine a neutral plasma with density of ions n_0 . When the sheet of electrons moves by a small amount ξ this creates a positive surface charge density $\sigma = en_0\xi$ and the restoring force on the electrons as a result of this surface charge is $E = 4\pi en_0\xi$ from Gauss' Law, leading to the same results given

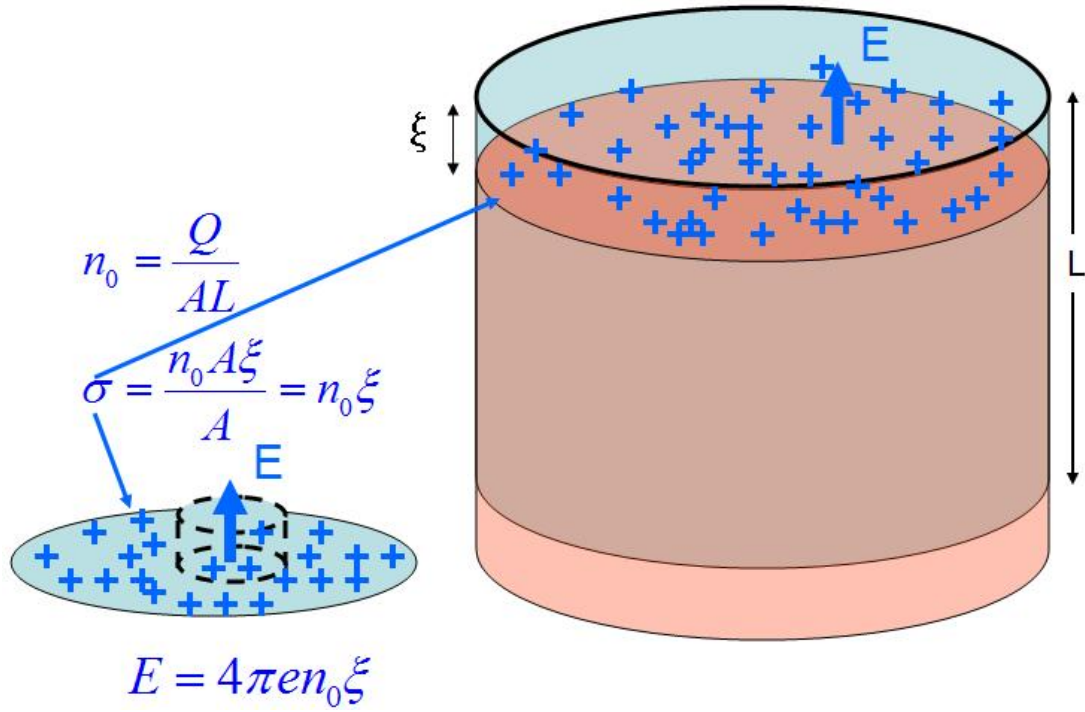


Figure 3.2: Equations that results from the displacement of a sheet of charge by ξ and a cartoon of the displacement.

in Eq. 3.11. The solution to Eq. 3.18 is $\xi = A(x_0)\sin(\omega_p t) + B(x_0)\sin(\omega_p t)$ For a specific case $A = 0$, $\xi = B\sin(kx_0)$ and $x = x_0 + B\sin(kx_0)$. We can easily plot $x = x_0 + \xi(x_0)$ vs E by varying x_0 . Figure 3.3 shows electric field as a function of position for $k=1$ and $A=0.1, 1, 2$ and 5 . For A greater than $1/k$ the field is double valued, this corresponds to sheets of charge crossing or wave breaking. Ordering of electrons (sheets not crossing) is maintained as long as change in X is greater than change in equilibrium position (Δx_0). This means

$$\frac{\partial X}{\partial x_0} > -1 \quad (3.19)$$

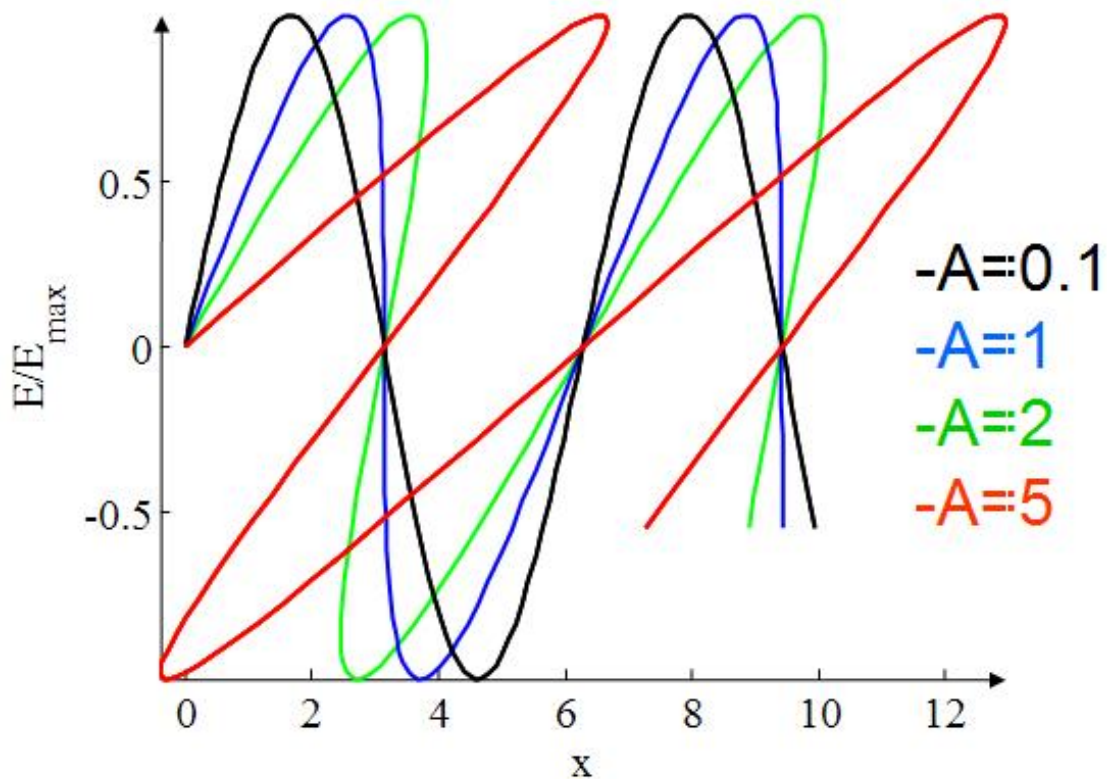


Figure 3.3: E/E_{max} vs x for different values of A , $k = 1$.

Therefore this condition gives $Ak\cos(kx_0) = -1$. This implies the maximum value of E will occur when

$$Ak = 1 \quad (3.20)$$

$$E_{max} = \frac{4\pi en_0}{k} \quad (3.21)$$

$$(3.22)$$

or

$$E_{max} = \frac{mv_\phi\omega_p}{e} \quad (3.23)$$

This is the 1D non-relativistic wave breaking limit derived by Dawson.

3.2 1-d cold relativistic

We now extend the non-relativistic treatment of the previous section to the case of relativistic motion. In this case, the momentum equation is replaced by $\frac{dp}{dt} = -eE$ where $p = \gamma mv$ and $\gamma = \frac{1}{\sqrt{1 - \frac{v^2}{c^2}}}$. Equations for E and n derived for the non-relativistic case are the same. Taking the derivative of E and replacing in the derivative of the equation of motion we obtain

$$\frac{d^2p}{d^2t} = -4\pi e^2 n_0 \frac{d\xi}{dt} = -4\pi e^2 n_0 v$$

Expressing v in terms of p from

$$v^2 = \frac{p^2}{m^2(1 + \frac{p^2}{c^2})} \quad (3.24)$$

gives

$$\frac{d^2p}{d^2t} = -\omega_p^2 \frac{p}{\sqrt{1 + \frac{p^2}{m^2 c^2}}}$$

multiplying by dp/dt and integrating we obtain

$$\frac{\dot{p}^2}{2} + \omega_p^2 m^2 c^2 \sqrt{1 + \frac{p^2}{m^2 c^2}} = constant \quad (3.25)$$

We can find the constant using the extremum of p . At the extremum $\dot{p} = 0$ hence $\omega_p^2 m^2 c^2 \sqrt{1 + \frac{p^2}{m^2 c^2}} = constant$. This is equivalent to $\omega_p^2 m^2 c^2 \gamma = constant$ where $\gamma = \sqrt{1 + \frac{p^2}{m^2 c^2}}$. For wave like solutions in other words solutions where the physical quantities are only functions of $x - v_\phi t$ we can write $\frac{d\xi}{dt} = -v_\phi \frac{\partial \xi}{\partial x_0}$. $\frac{\partial \xi}{\partial x_0} = -1$ gives an extremum in eq. 3.15. Therefore

$$v = v_\phi$$

and $p = p_\phi$, $\omega_p^2 m^2 c^2 \gamma_\phi = constant$

Substituting \dot{p} in $E = -\frac{\dot{p}}{e}$ gives

$$E = \pm \frac{mc\omega_p}{e} \sqrt{2(\gamma_\phi - \gamma)} \quad (3.26)$$

therefore we have $E = E_{max}$ for $\gamma = 1$

$$E_{max} = \pm \frac{mc\omega_p}{e} \sqrt{2(\gamma_\phi - 1)} \quad (3.27)$$

This is the result of Akhiezer and Polovin [AP56].

3.2.1 Trapping threshold in a 3D cold relativistic plasma wake in the presence of ionization

Discussion of the previous sections was exact for cold 1-D plasma waves; however, in all realizable experiments to date the 1-D approximation is not a good one.

Motion is often predominantly radial in the blowout regime. Here we extend the discussion of trapping to 3-D. We investigate the threshold for the onset of trapping in a 3D highly relativistic wake in the presence of an ionizing gas. We begin with the constant of motion for particles in arbitrary wave potentials of the form, $\mathbf{A} = \mathbf{A}(x, y, z - v_\phi t)$, $\Phi = \Phi(x, y, z - v_\phi t)$. This constant [MA97] can be obtained as follows:

The Hamiltonian for a charged particle in potentials ϕ and \mathbf{A} is

$$H = \gamma mc^2 + q\Phi \quad (3.28)$$

if we choose the canonical momentum to be $\mathbf{P} = \mathbf{p} + q\mathbf{A}$, the Hamiltonian equations of motion are

$$\dot{\mathbf{r}} = \frac{\partial H}{\partial \mathbf{P}} \quad (3.29)$$

$$\dot{\mathbf{P}} = -\frac{\partial H}{\partial \mathbf{r}} \quad (3.30)$$

We define $\xi = z - v_\phi t$. The full time derivative of a physical quantity Q can be written using the chain rule and Hamiltonian equations of motion

$$\frac{dQ}{dt} = \frac{\partial H}{\partial \mathbf{P}} \frac{\partial Q}{\partial \mathbf{r}} - \frac{\partial H}{\partial \mathbf{r}} \frac{\partial Q}{\partial \mathbf{P}} + \frac{\partial Q}{\partial t} \quad (3.31)$$

for any Q . For example if $Q = H$ this gives $\frac{dH}{dt} = \frac{\partial H}{\partial t}$. Here we choose $Q = H - v_\phi \mathbf{P}_z$; then using the chain rule we have

$$\frac{dQ}{dt} = \frac{dH}{dt} - v_\phi \frac{dP_z}{dt} \quad (3.32)$$

(3.33)

Using 3.27 we write

$$\frac{dP_z}{dt} = -\frac{\partial H}{\partial z} \quad (3.34)$$

For any physical quantity $Q(\xi)$ we have the following partial derivative relations

$$\frac{\partial Q}{\partial z} = \frac{\partial Q}{\partial \xi} \quad (3.35)$$

$$\frac{\partial Q}{\partial t} = -\frac{v_\phi}{c} \frac{\partial Q}{\partial \xi} \quad (3.36)$$

Using these relations we can substitute for the two terms on the left side of 3.29 and we obtain

$$\frac{dQ}{dt} = 0 \quad (3.37)$$

So Q is a constant of the motion. For a charged particle, $H = \gamma mc^2 + q\Phi$ and $Q = \gamma mc^2 + q\Phi - v_\phi P_z$. This constant of motion can be written as

$$\gamma mc - \frac{v_\phi}{c} p_z + q \frac{\Psi}{c} = \text{constant} \quad (3.38)$$

where γ is the particle's Lorentz factor and p_z is the longitudinal momentum of the trapped electron. The potential function $\Psi = \Phi - v_\phi A_z$ is related to the longitudinal wakefield by $E_z = -\partial_\xi \Psi$ where $\xi = z - v_\phi t$. Evaluating Eq.(3.38) for particles ionized at rest ($p_z = 0, \gamma = 1$), near the axis, and at a phase such that $\Psi = \Psi_i$ (see Fig. 3.4(a),(b)) gives the constant in Eq.(3.38) to be $mc + q \frac{\Psi_i}{c}$.

The trapping condition follows from the requirement that the electron velocity V_z reaches the wake phase velocity v_ϕ by the time the electron slips back to the peak of the potential at $\Psi = \Psi_{max}$. $v_z = v_\phi$ and $p_z = \gamma m v_z = \gamma m v_\phi$

Therefore, we have

$$mc - \gamma mc + \gamma m \frac{v_\phi^2}{c} \leq \frac{q}{c} (\Psi_{max} - \Psi_i) \quad (3.39)$$

$$mc(1 - \gamma + m \frac{v_\phi^2}{c}) \leq \frac{q}{c} (\Psi_{max} - \Psi_i) \quad (3.40)$$

$$\gamma_\phi^{-2} = 1 - \frac{v_\phi^2}{c^2} \quad (3.41)$$

$$mc(1 - \gamma(1 - \frac{v_\phi^2}{c})) \leq \frac{q}{c} (\Psi_{max} - \Psi_i) \quad (3.42)$$

$$mc(1 - \gamma \gamma_\phi^{-2}) \leq \frac{q}{c} (\Psi_{max} - \Psi_i) \quad (3.43)$$

If the particle is born near the axis its perpendicular velocity remains much smaller than its perpendicular velocity ($v_\perp \ll v_z$), then

$$\gamma = \frac{1}{\sqrt{1 - \frac{v_z^2}{c^2} - \frac{v_\perp^2}{c^2}}} \quad (3.44)$$

and at trapping $\gamma = \gamma_\phi$. The trapping condition is then

$$mc^2(1 - \frac{1}{\gamma_\phi}) \leq q(\Psi_{max} - \Psi_i) \quad (3.45)$$

Therefore the lowest threshold for trapping occurs for a particle born where $\Psi = \Psi_{min}$ which is where the electric field of the wake crosses the axis, at the potential ξ_{min} . It is interesting to relate this threshold in potential to the maximum electric field of the wake. A theory for wakes in non- linear blow out regime shows that the slope of E_z is nearly linear over a large region of ξ from ξ_{min} to ξ_{max} (see Fig. 3.4(a)) [LHZ⁺06]. We thus write $\tilde{E}_z \approx k(\tilde{\xi} - \tilde{\xi}_{min})$ where we obtain k

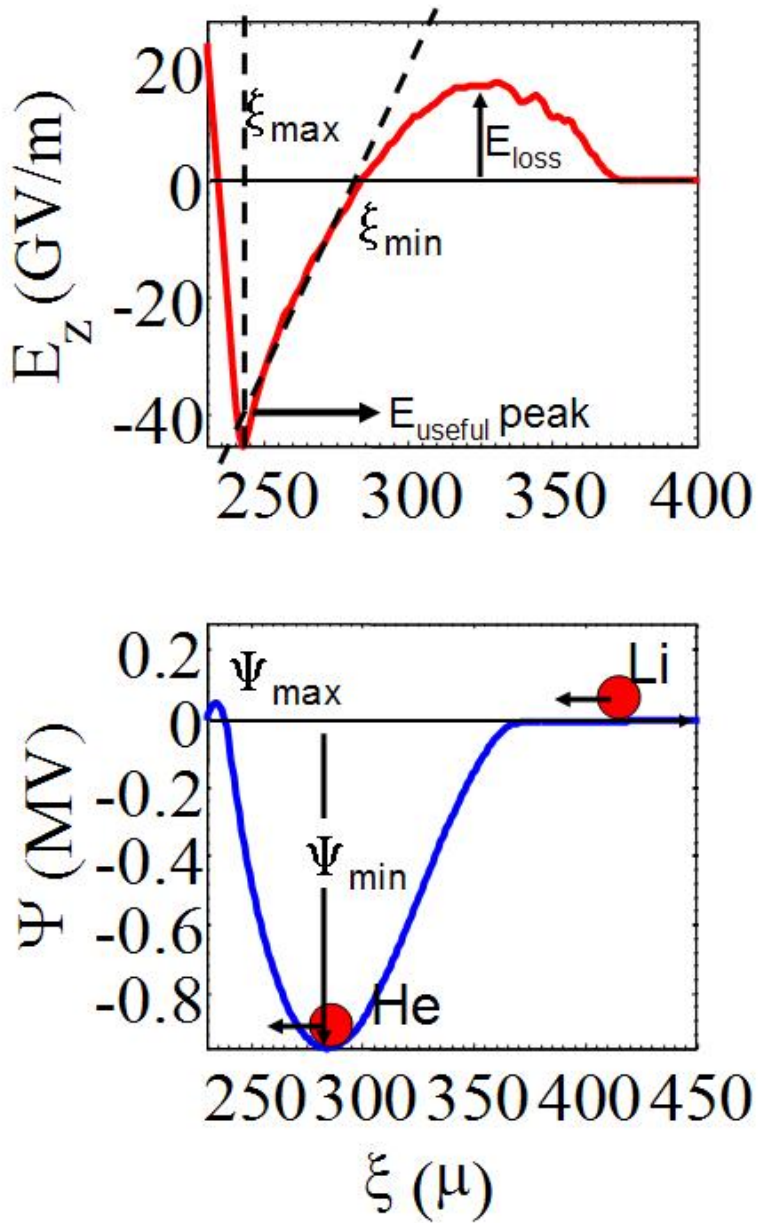


Figure 3.4: (a) On-axis wake field, $E_z(c)$. (b) Wake potential Ψ .

from linear fitting to the E_z field obtained from PIC simulations; tildes indicate dimensionless quantities ($\tilde{E} = E/(mc\omega_p/e)$, $\tilde{\xi} = \xi/(c/\omega_p)$). Integrating the linear

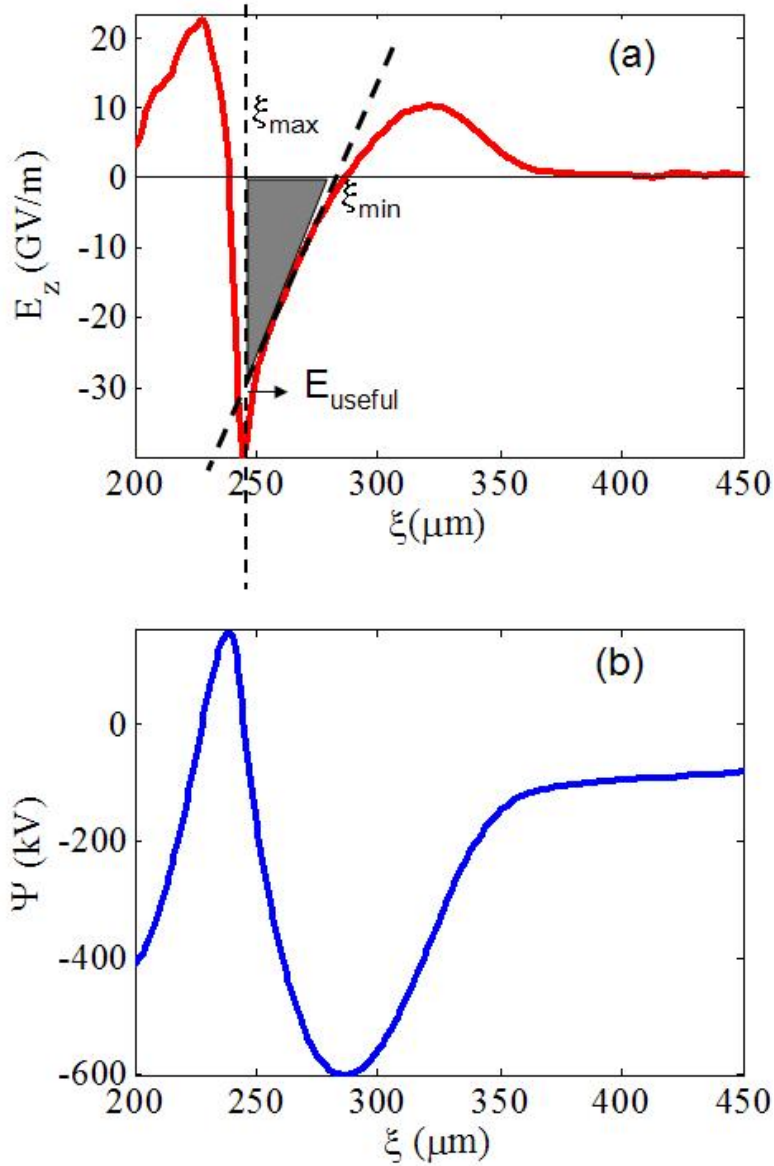


Figure 3.5: On axis electric field and the potential Ψ .

E_z from ξ_{min} to ξ_{max} (see Fig. 3.4) gives the rhs of Eq. 3.45. Therefore we obtain the trapping threshold (for $\gamma_\phi \gg 1$)

$$|\tilde{E}_{max}| \geq \sqrt{2k}. \quad (3.46)$$

Figure 3.5 shows the on-axis electric field and the corresponding potential, this is an example where the field has a linear region ending with a spike, since the potential energy that eventually turns the particles around corresponding to the spike is much smaller than potential energy contained in the linear region we define the field E_{useful} to approximate the maximum field amplitude for threshold calculation. E_{useful} is the field amplitude at ξ_{max} extrapolated from the linear fit to the electric field starting at ξ_{min} , where E_z is zero. When we derive the trapping threshold we use E_{useful} , doing so neglects the area under the longitudinal field spike.

It is interesting to note that in the extreme blowout regime, k approaches the value $1/2$ [L⁺⁰⁵] so that $E_{max} \approx 1$, coincidentally the same value Dawson obtained non-relativistically in 1-D (Eq. 3.18).

3.2.2 Calculation of the cold relativistic trapping threshold in the presence of ionization in 1-D

Here we rederive the result of the previous section in the limit of a 1-D wave and show that for trapping of ionized electrons born in the wake, the result is the same.

$$\begin{aligned} E_z &= \partial_z \Phi - \frac{1}{c} \partial_t A_z \\ E_z &= -\partial_\xi (\Phi - A_z) \\ E_z &= -\partial_\xi \Psi \end{aligned}$$

In 1-D $\Phi = \Psi$ since vector potential $\mathbf{A} = \mathbf{0}$. For calculation of trapping threshold we go to the plasma wake frame. The trapping condition is that the particle's

potential energy relative to the peak of the wake should be higher than the kinetic energy of the particle (see figure x), that is,

$$(\gamma' - 1)mc^2 \leq q(\Psi'_{max} - \Psi'_0) \quad (3.47)$$

where ' indicates that the quantity is in the wake frame. Lorentz transformation of the electromagnetic fields in the moving frame with a relative velocity \mathbf{v} is given by

$$\mathbf{E}' = \gamma(\mathbf{E} + \beta \times \mathbf{B}) - \frac{\gamma^2}{\gamma + 1}\beta(\beta \cdot \mathbf{E}) \quad (3.48)$$

$$\mathbf{B}' = \gamma(\mathbf{B} - \beta \times \mathbf{E}) - \frac{\gamma^2}{\gamma + 1}\beta(\beta \cdot \mathbf{B}) \quad (3.49)$$

$\Psi' = \gamma_\phi\Psi$ which can be seen from the following (subscript ϕ refers to the plasma wake frame).

$$\Psi' = \int E'_z d\xi' \quad (3.50)$$

$$d\xi' = \gamma_\phi d\xi \quad (3.51)$$

$$E'_z = E_z \quad (3.52)$$

$$\Psi' = \gamma_\phi\Psi \quad (3.53)$$

Assuming that the trapped particles are born at rest

$$\gamma' = \gamma_\phi \quad (3.54)$$

and they are born at $\Psi_0 = \Psi_i$, then the condition for trapping becomes

$$1 - \frac{1}{\gamma_\phi} \leq q(\Psi_{max} - \Psi_i)/mc^2 \quad (3.55)$$

for $\gamma_\phi \gg 1$ this reduces to

$$mc^2 \leq q(\Psi_{max} - \Psi_i) \quad (3.56)$$

$\Psi_{max} - \Psi_{min}$ can be approximated using the integral of E_z

$$\Psi_{max} - \Psi_{min} \approx \int_{\xi_{min}}^{\xi_{max}} E_\xi d\xi \quad (3.57)$$

as illustrated in Fig. 3.4 (a) electric field between ξ_{min} and ξ_{max} can be approximated with a linear fit. Therefore the integral can be calculated using the area of the triangle between ξ_{min} and ξ_{max} which gives

$$\Psi_{max} - \Psi_{min} \approx \frac{1}{2} E_{max} l \quad (3.58)$$

$$l \equiv \xi_{min} - \xi_{max} \quad (3.59)$$

We can approximate the electric field in the region where it crosses 0 and before the spike as

$$\tilde{E} = k(\tilde{\xi} - \tilde{\xi}_0) \quad (3.60)$$

where \tilde{E} and $\tilde{\xi}$ are defined as follows:

$$\tilde{E} = \frac{E}{\frac{mc\omega_p}{e}} \quad (3.61)$$

$$\tilde{\xi} = \frac{\xi}{\frac{c}{\omega_p}} \quad (3.62)$$

$$(3.63)$$

where $\omega_p = \sqrt{\frac{ne^2}{\epsilon_0 m}}$ is the plasma frequency. We finally obtain the threshold for trapping by substituting E for Ψ in Eq. 3.56

$$|\tilde{E}_{max}| \geq \sqrt{2k}. \quad (3.64)$$

3.3 Dark Current

The trapping threshold just described is physically similar to the dark current threshold in conventional rf accelerators. In this section we review this and show the connection. In a conventional rf accelerator an electron gas is formed through the field emission process in the accelerator wall. When the accelerating gradient is above a critical value, trapping of this electron gas creates a current referred to as dark current. Trapped electrons in an rf cavity create radiation, cause noise in instruments, and absorb rf energy. The trapping threshold in an rf cavity is given by $E_c = 1.6/\lambda MV/m$ [AS70]. This can be derived from Eqn. 3.56) as follows: Let the RF field be $E = E_{max} \sin k\xi$ and $\Psi = \frac{E}{k} \cos k\xi$ with $k = \frac{2\pi}{\lambda}$. Assuming that background field emmited gas electrons start out on the zero crossing of the sine wave of the RF field (this is the optimum place to be trapped) and calculating the potential change for these electrons for the whole accelerating part. $(\Psi - \Psi_0) = \lambda E_{max}/\pi$

$$mc^2 \leq q(\Psi - \Psi_i) \quad (3.65)$$

$$mc^2 \leq eE_c\lambda/\pi \quad (3.66)$$

$$1.6/\lambda \text{ MV/m} \leq E_c \quad (3.67)$$

For the SLAC accelerator, $\lambda = 10.5 \text{ cm}$, giving $E_{max} = 15 \text{ MV/m}$, 3 orders of magnitude smaller than the trapping threshold in a PWFA of density $n = 10^{17} \text{ cm}^{-3}$.

Chapter 4

Experimental Results

In this chapter we present the experimental results obtained from the trapped particle diagnostics and their analysis. We try to establish how trapping occurs, when it occurs, where the trapped particles originate, and what properties trapped particles have.

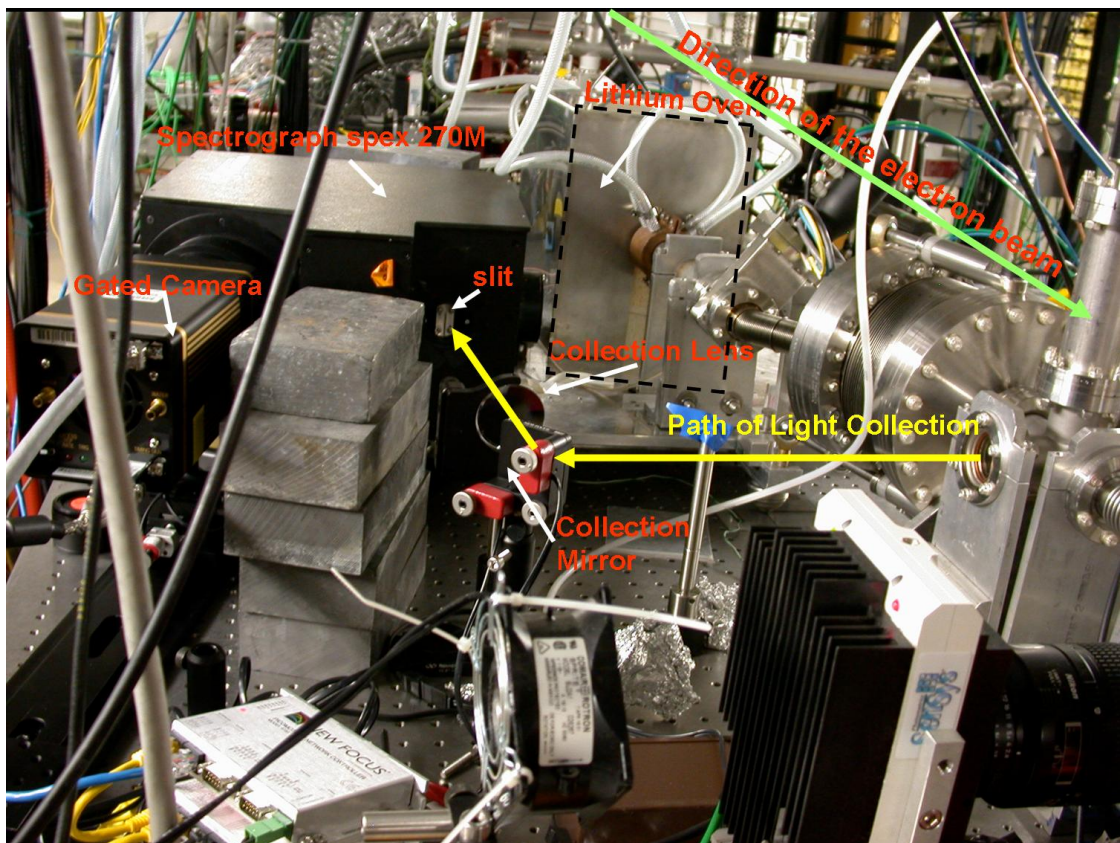


Figure 4.1: Picture of the spectrograph and the light collection setup.

4.1 Evidence for trapped particles and experimental trapping threshold

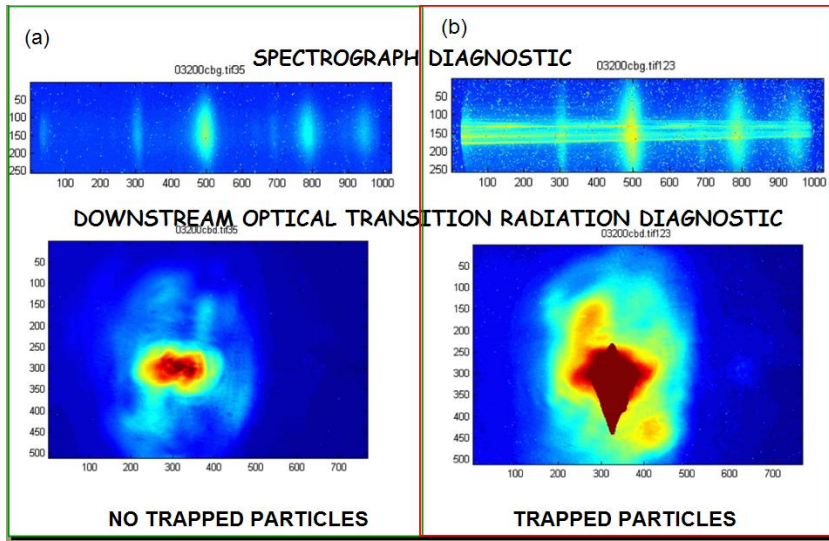


Figure 4.2: (a) A typical image from two independent diagnostics downstream otr camera and the spectrograph. (b) A continuum of light appearing on spectrograph and the down otr camera is being saturated with extra light.

The Stanford linear accelerator drive beam that we used in the plasma wake field experiment contains about 1.8×10^{10} electrons. Extra charge reading on the current transformers after the plasma is the first experimental direct evidence for particle trapping. The optical diagnostics, spectrograph and downstream otr camera also show evidence of particle trapping. The extra charge reading is simultaneous with a very bright continuum of light on the spectrograph camera (fig. 2.17) and light orders of magnitude higher intensity on the otr camera (see Fig. 4.2). Fig. 4.5 shows the spectrograph images with and without trapping. Notice that the atomic emission lines are also brighter in Fig. 4.5 (b) indicating that the wake field amplitude is higher [OBC⁺04]. The properties of this light are discussed in the next section.

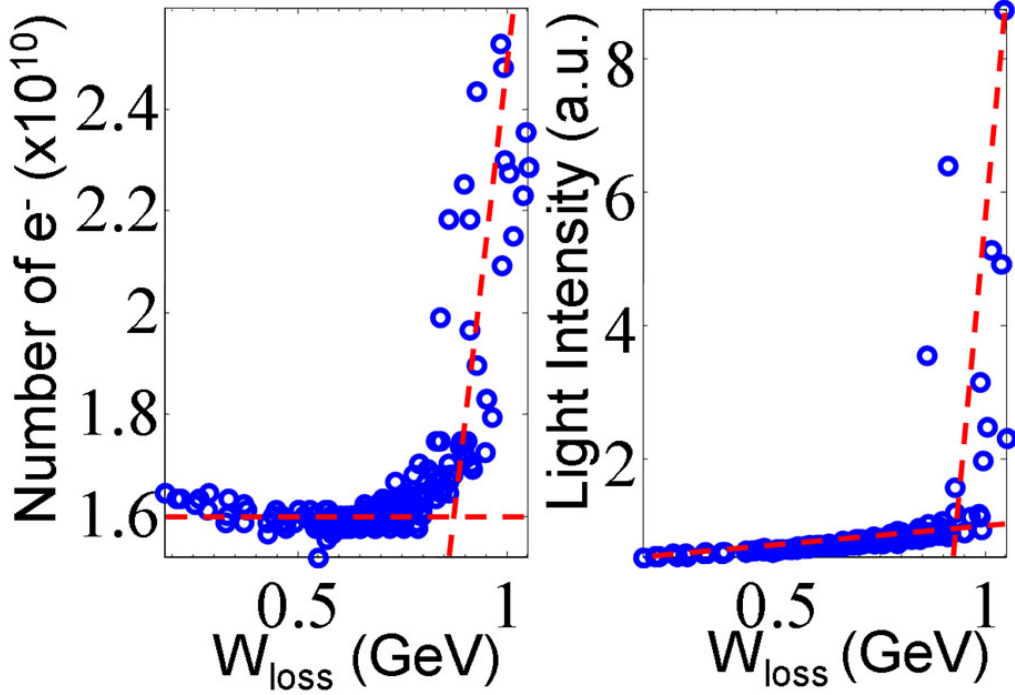


Figure 4.3: (a) Charge measured after the plasma versus the average energy loss. (b) Relative amount of visible continuum light. Note, the relative fluctuations of the charge below threshold on Fig. 4.3(a) are also present in the incoming charge as measured before the plasma (see Fig. 4.4). The plasma density is $1.6 \times 10^{17} cm^{-3}$.

The trapping can be controlled. It can be turned on and off by changing the wake field amplitude. At a constant density the wake field amplitude can be varied by changing the parameters of the drive beam such as the total charge or the bunch length. In the experiment we varied the bunch length to study trapping. The change in the wake field amplitude was indirectly determined by measuring the average energy loss (W_{loss}) by the drive beam electrons in exciting the wake using the cerenkov diagnostic. Therefore the trapping threshold in wake field amplitude at which we observe a sudden increase in the amount of charge detected after the plasma can be seen when we correlate the W_{loss} with the charge (Fig.4.3(a)). Since

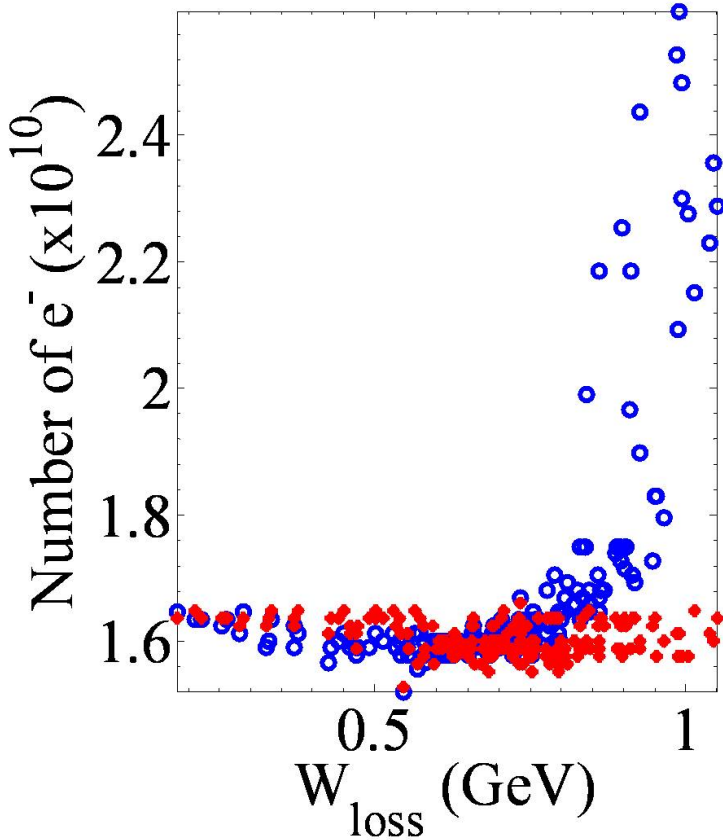


Figure 4.4: (a) The charge measured after the plasma (blue circles) and the charge measured before the plasma (red) vs. the average energy loss.

the appearance of this excess charge also coincides with the abrupt increase in the amount of light collected downstream of the plasma. Correlation of excess light ((spectral region between 520 nm and 530 nm) with W_{loss} also reveals the threshold (Fig. 4.3(b)). Choosing a region where continuum light is on top of the atomic emission lines will show the same threshold except the initial slope when there is no trapping will be steeper because of the linear increase in the plasma emission light as a result of wake field [OBC⁺04]. We interpret these results as evidence of the onset of particle trapping. In the next chapter we compare the measured

trapping threshold to the threshold calculated from the analytical model and the simulations.

4.2 Properties of trapped particles from optical diagnostics

When there is no trapping the spectrograph collects light coming from the plasma as a result of neutral gas line emission, Cherenkov light emission as a result of the highly relativistic drive beam traversing the neutral helium region, and the otr light as a result of drive beam passing through the collection foil (down pellicle see fig 2.17). Depending on the gate of the gated camera one or all could be present. When the particle trapping occurs trapped particles also produce light similar to the electron beam. Our analysis shows that this light is partially coherent and therefore orders of magnitude brighter than incoherent light.

Normally each beam electron produces a certain amount of incoherent optical transition radiation. Therefore orders of magnitude more light (as in Fig. 4.3 (b)) means there was an enormous increase in charge or a modest increase with some electrons emitting coherent transition radiation. Coherency enhances the radiation by square of the number of electrons. It could also be that this is a combination of both effects and hence the light is partially coherent.

Consider a bunch with N electrons. Let $e(t)$ represent the radiation each electron produces as it goes through the cause of the radiation (transition, Cherenkov, synchrotron radiation etc.). The total radiation field is $E(t) = \sum_{k=1}^N e(t - t_k)$

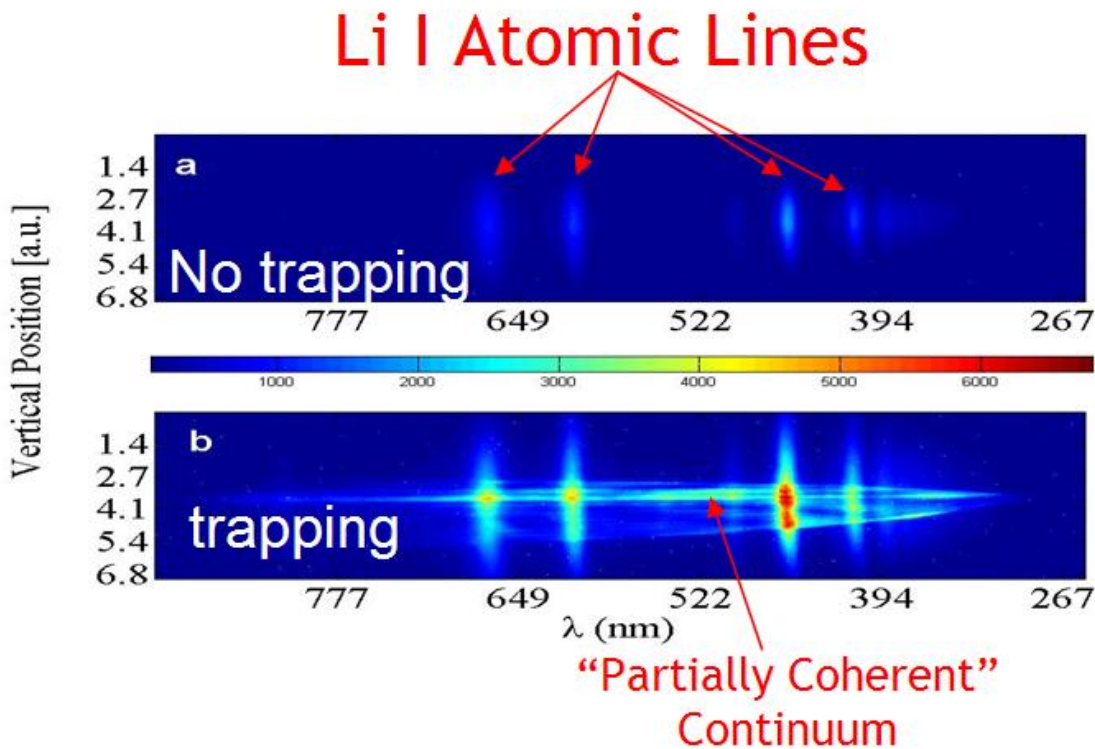


Figure 4.5: (a) Spectrograph image showing the atomic emission lines (He I, Li I) when there is no trapping. (b) Continuum emission caused by trapped particles on top of emission lines.

where t_k is the time of arrival of the electron to the cause of the radiation, and the Fourier transform of $E(t)$ can be written as

$$\hat{E}(\omega) = \hat{e}(\omega) \sum_{k=1}^N e^{-i\omega t_k} \quad (4.1)$$

where $\hat{e}(\omega)$ is simply the Fourier transform of the radiation field of a single electron.

The power spectrum $P(\omega)$ will be

$$P(\omega) = e(\omega)^2 \sum_{k,l=1}^N e^{i\omega(t_k - t_l)} \quad (4.2)$$

Starting off from this summation we can write an insightful expression for the radiation intensity of an electron bunch consisting of N electrons as follows

$$I(\omega) = e(\omega)(N + N^2 |\tilde{f}(\omega)|^2) \quad (4.3)$$

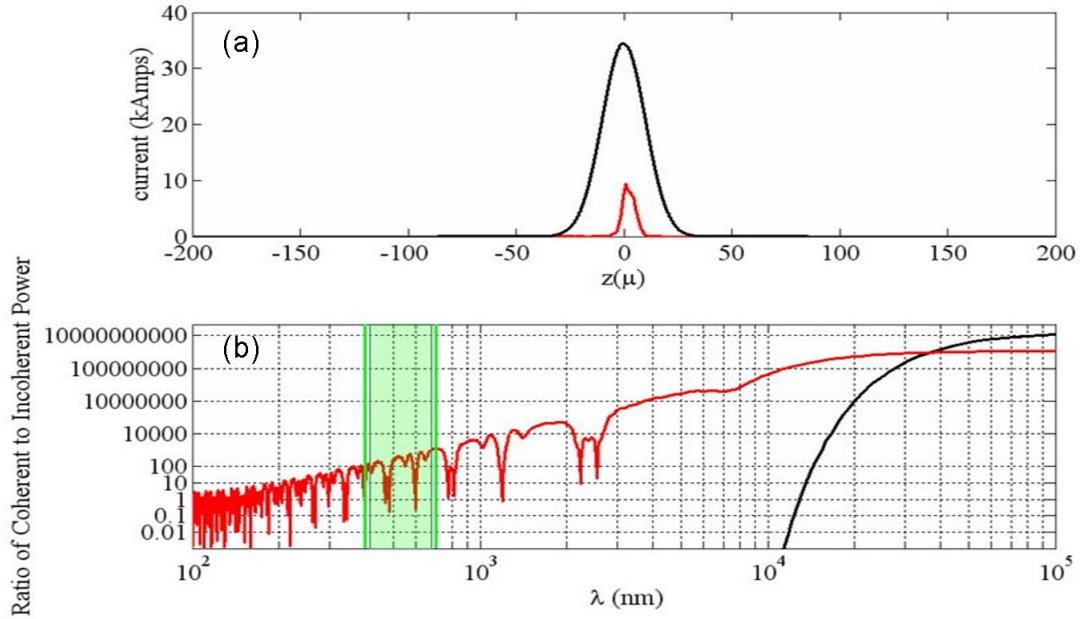


Figure 4.6: (a) Current profile of two bunches: a Gaussian (black line) with rms bunch length of $10 \mu\text{m}$ and a non-Gaussian bunch (This is the current profile of a trapped particle bunch, and is taken from simulation done with the particle in cell code OSIRIS) with rms bunch length of $3 \mu\text{m}$ (red line). (b) The log scale plot of the function $N |\tilde{f}(\omega)|^2$. Green shaded area marks the visible spectrum.

where $\tilde{f}(\omega)$ is the normalized Fourier transform of the longitudinal distribution (current) of the electron bunch. As we shortly illustrate this expression reveals that one part of the radiation consists of only the sum of the contributions of each electron. This is called incoherent radiation; whereas one part is the sum of the squares of the contributions of each electron multiplied by a factor. This is called

coherent radiation and depending on the frequency range it can be negligible or the dominant term in the total radiation. Figure 4.6(a) shows the current profile of a Gaussian beam with rms bunch length of $10 \mu\text{m}$ and a non-Gaussian beam with rms bunch length of $3\mu\text{m}$ (shape taken from a representative PIC simulation of our experiment). Figure 4.6(b) is the ratio of coherent power to incoherent power for the Gaussian (black line) and non-Gaussian bunches (red line). There is a very sharp drop off at $\lambda = 10\mu\text{m}$ for the Gaussian bunch where the ratio goes below 1. This means that the Gaussian electron bunch radiates coherently only for wavelengths larger than $10 \mu\text{m}$. Whereas the drop-off is not as sharp for the non-Gaussian bunch. The ratio is still larger than one up to the visible spectrum. This can be attributed to the sharp features in the current profile that are on the length scale of visible radiation.

Apart from the orders of magnitude more continuum light, the light collection set-up also revealed that the continuum radiation produced by the trapped particles has modulations. This interference pattern supports the hypothesis that the visible light is emitted coherently. This coherent emission suggests a longitudinal structure of the trapped particles with features shorter than the observed visible wavelength of $\approx 600 \text{ nm}$ (see Fig. 4(b)) or $\approx 2 \text{ fs}$. As we shall see later, simulations show that trapped particles are produced in multiple buckets of the plasma wave. The interference pattern formed as a result can be used to calculate the separation of the trapped particle bunches as follows.

The coherent radiation from two bunches with Gaussian profiles forms an interference pattern the spacing between two extremum ($\Delta\lambda$) is related to the spacing of the bunches Δz . The current profile shown in Fig. 4.15 can be written as

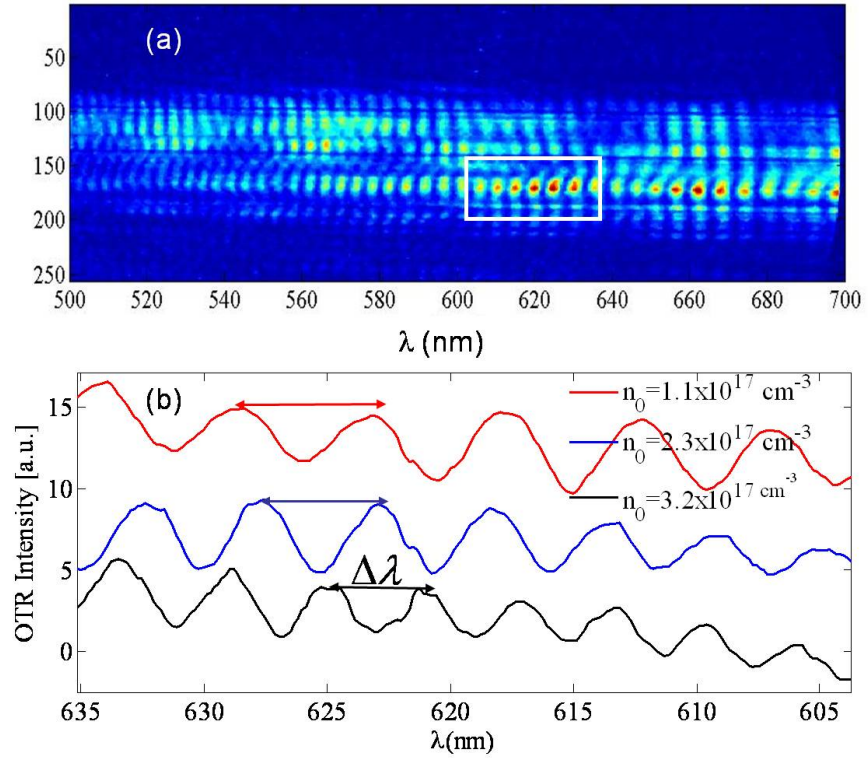


Figure 4.7: (a) Spectrograph image recorded using the spectrograph set-up II showing the interference pattern (modulations). (b) Light intensity versus wavelength, calculated by vertically summing the image over the marked white rectangular region.

$I(z) = Ae^{\frac{-z^2}{2\sigma_{z1}^2}} + Be^{\frac{-(z+\Delta z)^2}{2\sigma_{z2}^2}}$ where A and B are arbitrary constants and σ_z is the rms bunch length. The Fourier transform of $I(z)$ is

$$\tilde{I} = \int_{-\infty}^{\infty} I(z)e^{ikz}dz \quad (4.4)$$

$$\tilde{I} = \int_{-\infty}^{\infty} \left(Ae^{\frac{-z^2}{2\sigma_{z1}^2}} + Be^{\frac{-(z+\Delta z)^2}{2\sigma_{z2}^2}} \right) e^{ikz}dz \quad (4.5)$$

$$\tilde{I} = Ce^{k^2\sigma_{z1}^2} + De^{k^2\sigma_{z2}^2}e^{-ik\Delta z} \quad (4.6)$$

where C and D are constants and $k = \frac{2\pi}{\lambda}$. The interference pattern follows $\tilde{I}\tilde{I}^*$ where * represents the complex conjugate. Let $a \equiv Ce^{k^2\sigma_{z1}^2}$ and $b \equiv De^{k^2\sigma_{z2}^2}$ then $\tilde{I}\tilde{I}^*$

$$\tilde{I}\tilde{I}^* = (a + be^{-ik\Delta z})(a + be^{ik\Delta z}) \quad (4.7)$$

$$\tilde{I}\tilde{I}^* = (a^2 + abe^{-ik\Delta z} + abe^{ik\Delta z} + b^2) \quad (4.8)$$

$$\tilde{I}\tilde{I}^* = (a^2 + 2ab \cos(k\Delta z) + b^2) \quad (4.9)$$

The extrema condition is $k\Delta z = 2\pi n$ where $n = 0, 1, 2, \dots$. Therefore the distance between two extrema and spacing of the bunches related as

$$\Delta k = \frac{2\pi}{\Delta z} \quad (4.10)$$

$$\Delta k = 2\pi \frac{\Delta \lambda}{\lambda^2} \text{ or} \quad (4.11)$$

$$\Delta k = 2\pi \left(\frac{1}{\lambda_1} - \frac{1}{\lambda_2} \right) \quad (4.12)$$

Using this relation we deduce that the observed interference pattern is attributed to the coherent emission by multiple ultra-short bunches of trapped particles spaced by $\Delta z = \frac{\lambda^2}{\Delta \lambda} \cong 72, 84$ and $102 \mu m$ for the case of Fig. 4.7. This is slightly longer than the plasma wavelength of $60, 70, 100 \mu m$ for $n_0 = 3.2, 2.3, 1.1 \times 10^{17} cm^{-3}$ respectively as predicted by the linear theory[L⁺05]. This is consistent with the non-linear frequency shift to longer wavelengths expected for plasma wakes of larger amplitude [LHZ⁺06].

Spectrograph images also show modulations with a larger wavelength this suggests that the coherently emitting sources could be located much closer than the sources producing the smaller modulations. Images in Figures 4.8, 4.10, 4.12, are

a number of examples showing the variations in these larger wavelength modulations. The Figures 4.9,4.11,4.13 show the possible sources that could cause these modulations. Note that this is only a qualitative comparison (Continuum radiation from plasma, quantum efficiency of the camera etc. would affect the background and amplitude of these oscillations). There is a big variation in the number of these modulations which can be attributed to the change of longitudinal profile of the incoming electron beam. In the experiment it's been shown that the incoming electron beam could emit coherent light as a result of the scalloping caused by the transverse oscillations of the beam. Therefore these bigger modulations could result from the interference of the beam light and trapped particles light.

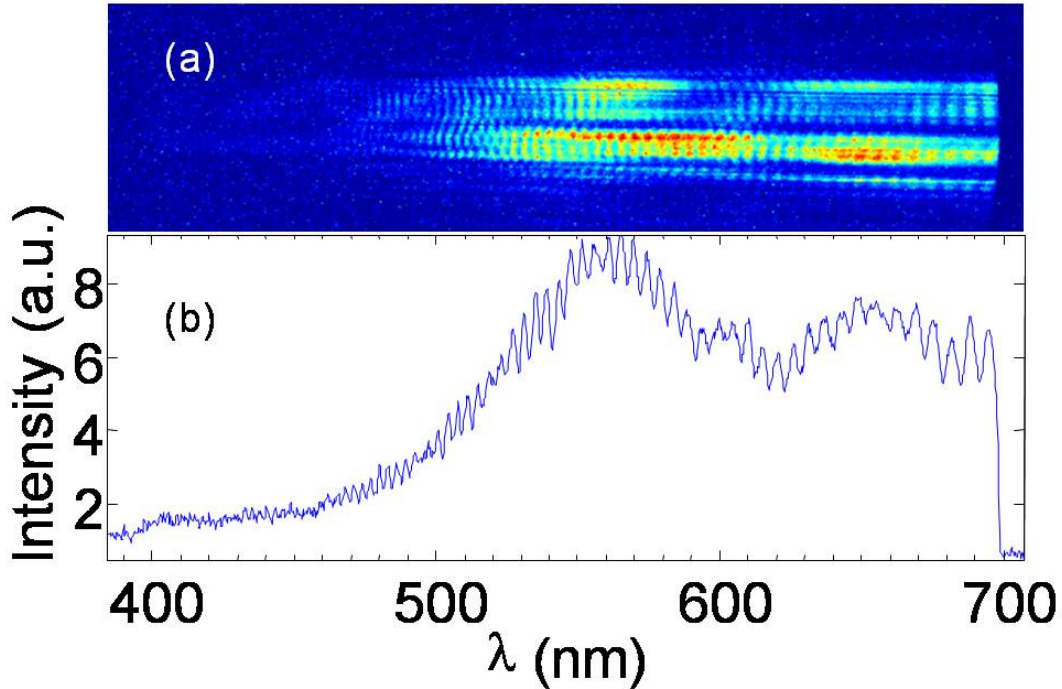


Figure 4.8: (a) Spectrograph image. (b) Light intensity versus wavelength, calculated by vertically summing the image in (a).

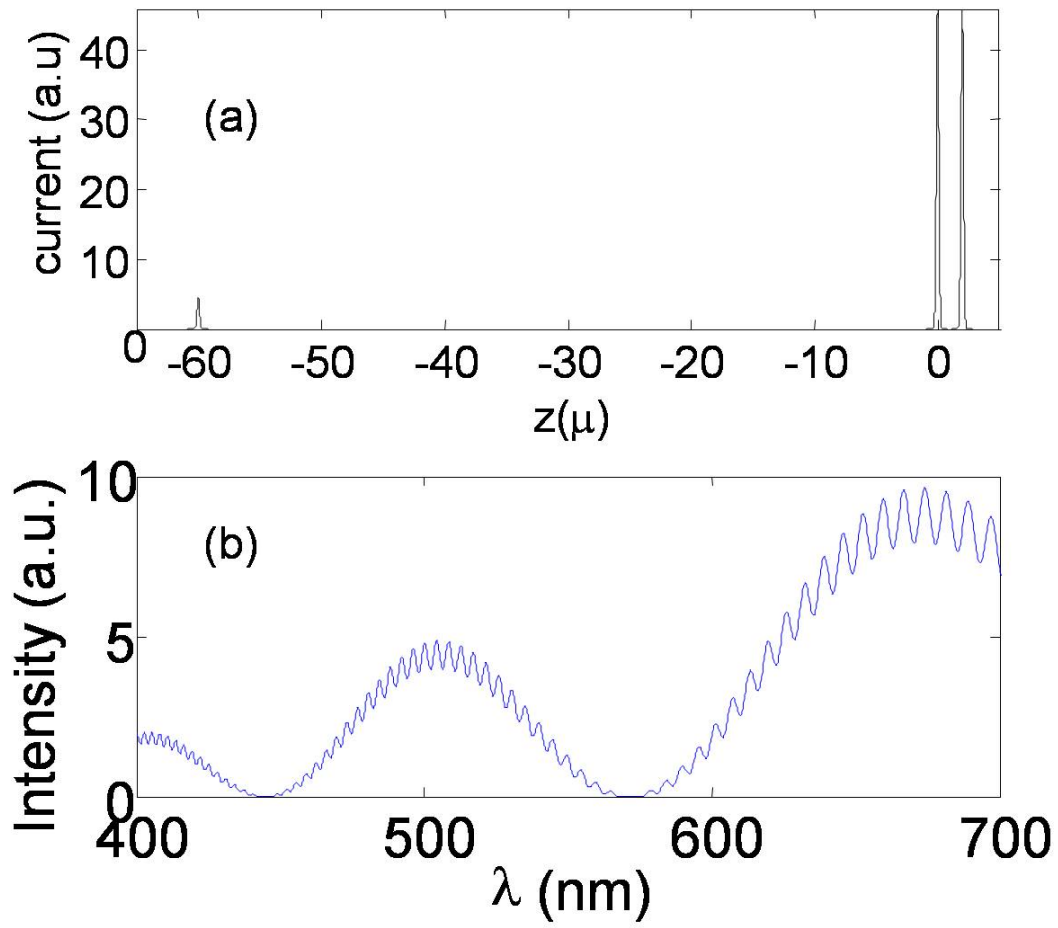


Figure 4.9: (a) Possible current source for modulations in 4.8: three Gaussian bunches each with a σ_z of $0.1 \mu\text{m}$ separated by 2 and $60 \mu\text{m}$. (b) The amplitude of the Fourier transform of this current source.

4.3 Beam loading and origin of trapped particles

In this section using simple energy transfer arguments we deduce that trapped particles are first born in the initial helium buffer region of the plasma source. We analyze several sets of experimental data where the position of the beam waist is varied. Varying the beam waist changes the initial electron beam transverse size

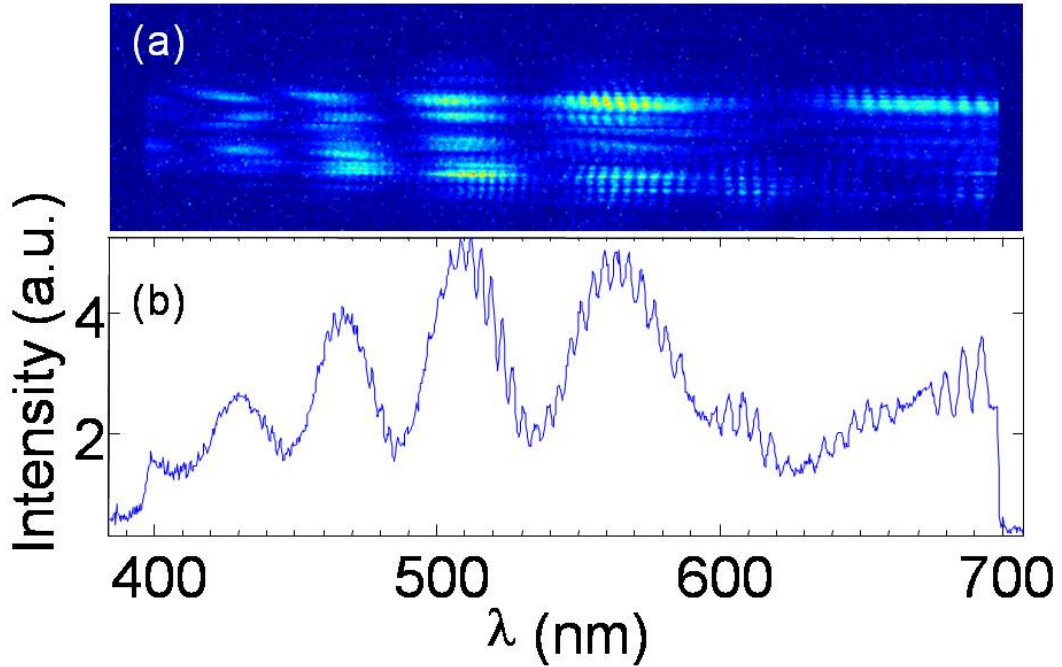


Figure 4.10: (a) Spectrograph image. (b) Light intensity versus wavelength, calculated by vertically summing the image in (a)

and therefore how large the plasma wake initially is. However as the beam self-focuses these differences disappear and the wake converges to the same amplitude eventually. We pick two cases where electron beams have two different waist locations -one at the plasma entrance and one deeper into the plasma- but the same longitudinal current profile. We pick the same longitudinal current profile by using the matching of x-ray profiles of the incoming electron beam.

Figure 4.16 shows these two cases. Figure 4.16 (a) shows the x-ray profiles on top of each other, figures (b) and (c) show the energy spectrum. This shows that in the case of waist location deeper into the plasma source there are more beam electrons experiencing energy gain. This shows up as a saturated color on the image. When there is less energy gain the corresponding energy spectrum on

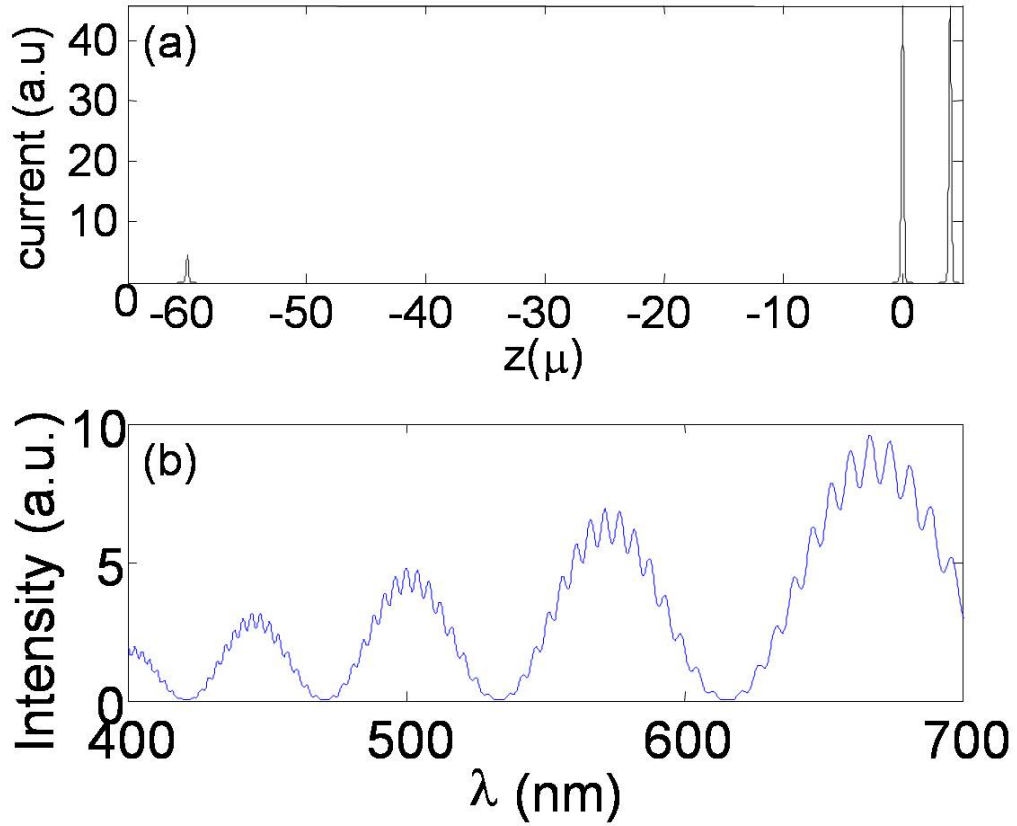


Figure 4.11: (a) Possible current source for modulations in 4.8: three Gaussian bunches each with a σ_z of $0.1 \mu m$ separated by 4 and $60 \mu m$. (b) The amplitude of the Fourier transform of this current source.

(c) shows a clump of particles at high energy marked as trapped particles in a dashed rectangle. This tells us that when the electron beam is focused earlier it traps lots of electrons from the buffer region and these electrons take the energy of the wake instead of the beam electrons. Therefore the electrons at the tail of the injected beam show up with less energy gain. Conversely, when the beam is focused further into the plasma, the electrons take the energy instead of the trapped particles. Another surprising effect is there is more charge coming out

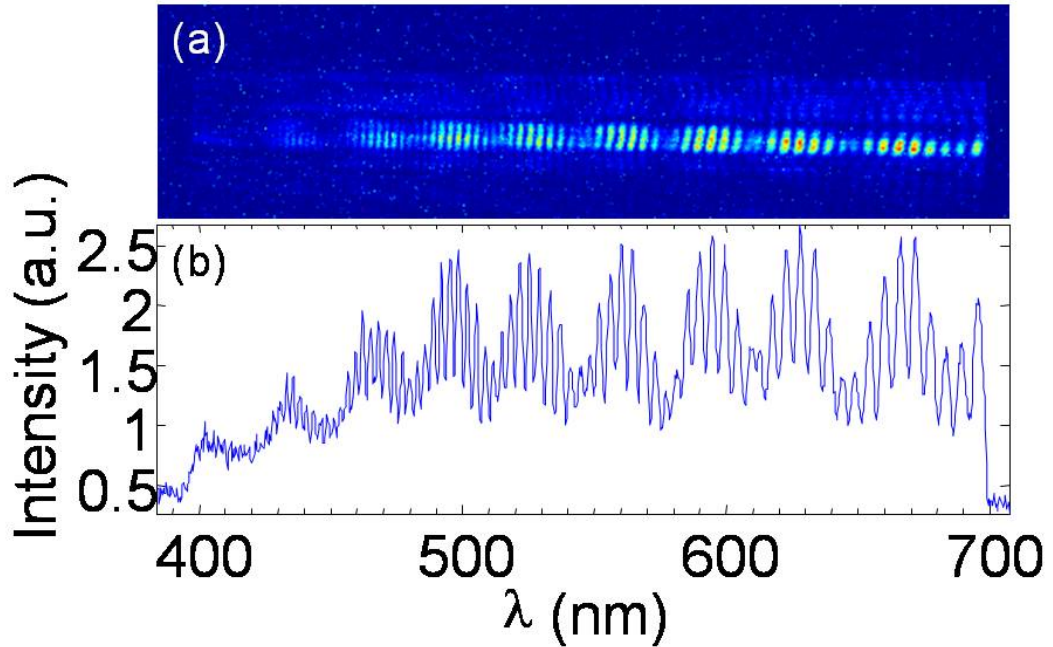


Figure 4.12: (a) Spectrograph image. (b) Light intensity versus wavelength, calculated by vertically summing the image in (a).

of the plasma when the waist is located further in. One would expect that as the extra charge reading on the current transformer increases there would be less energy gain. In this case the current transformer reads 8×10^{10} for the higher energy gain case compared to 4.9×10^{10} for the lower gain case. This can be explained as follows. Most of this charge is low energy electrons coming out of the plasma from the second buffer region. We know this from the simulations and also from the experiment([K⁺06], see next chapter). When the wake field is loaded less with the trapped particles from the first buffer region the wake can trap many more electrons at the second buffer. This is also evident from Fig. 4.17. Each color indicates a 200 set of constant waist events; the waist location is moved more into plasma source from left to right.

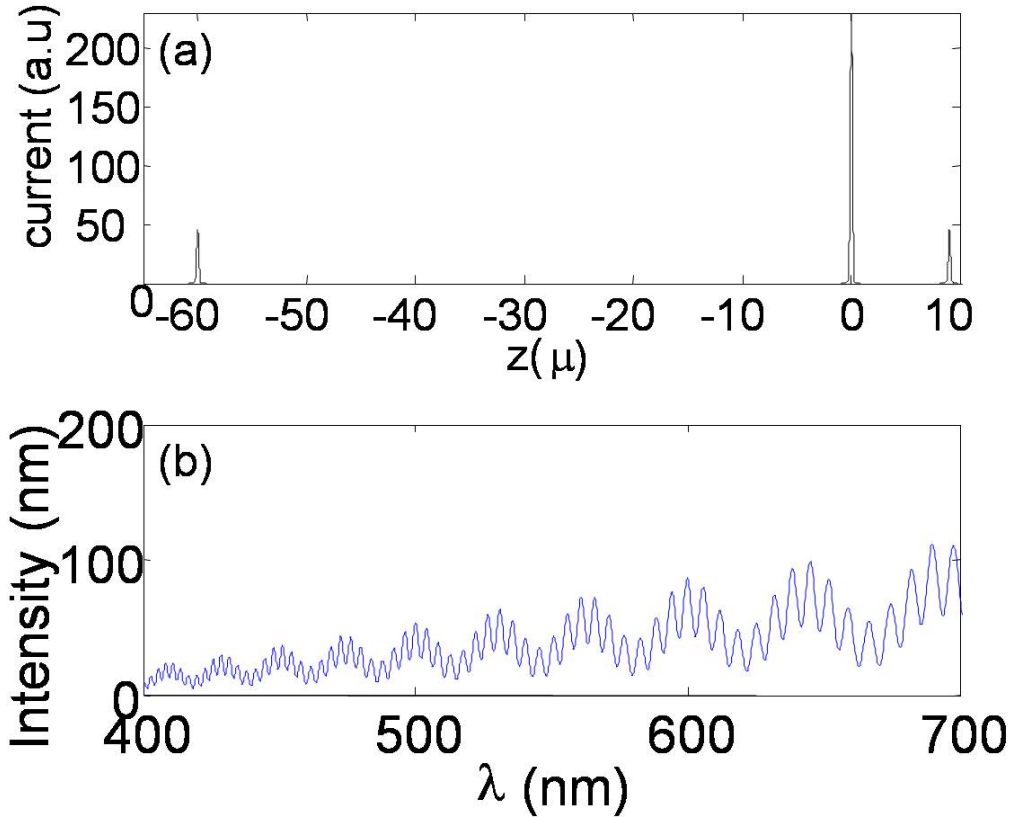


Figure 4.13: (a) Possible current source for modulations in 4.8: three Gaussian bunches each with a σ_z of $0.1 \mu m$ separated by 9 and $60 \mu m$. (b) The amplitude of the Fourier transform of this current source.

4.4 Energy and charge measurement of trapped particles from Cherenkov diagnostic

The experimental set up for the energy spectrum measurement (Fig. 2.11) enables us to image and measure the energy of trapped particles as well as the electron drive beam. Some particles show up with very high energy and very narrow features on the Cerenkov energy loss camera. We hypothesized that these were the trapped particles which gained a considerable amount of energy through the large

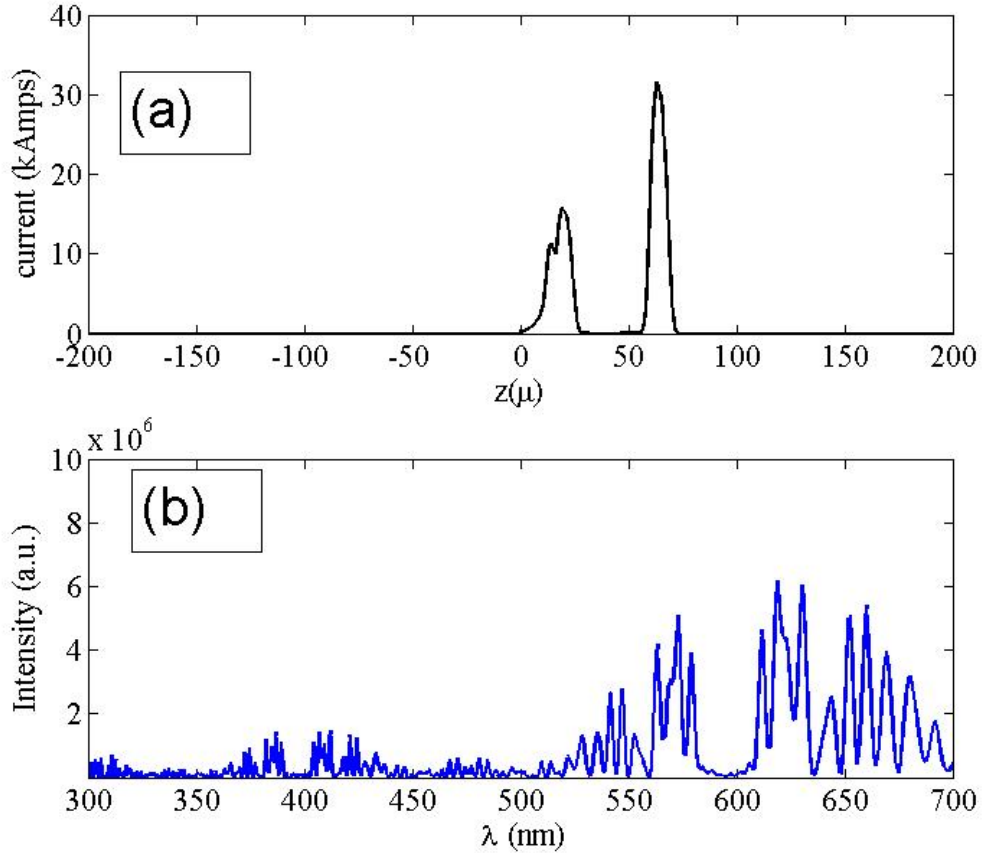


Figure 4.14: (a) Osiris simulation trapped bunches at the exit of the plasma. (b) The amplitude of the Fourier transform of the bunches.

wake over the 90 cm long plasma as we pointed out in the previous section. An important question is how many electrons are there in these bunches and can these be classified as mono energetic electron beams? We can calculate the energy distribution and number of trapped particles using the Cerenkov images as follows.

Figures 4.18, 4.19, 4.20, 4.21 show the energy spectra of the electrons exiting the plasma for several B field values. These are only a couple of examples out of hundreds of other events. These images show that there is a peak in energy

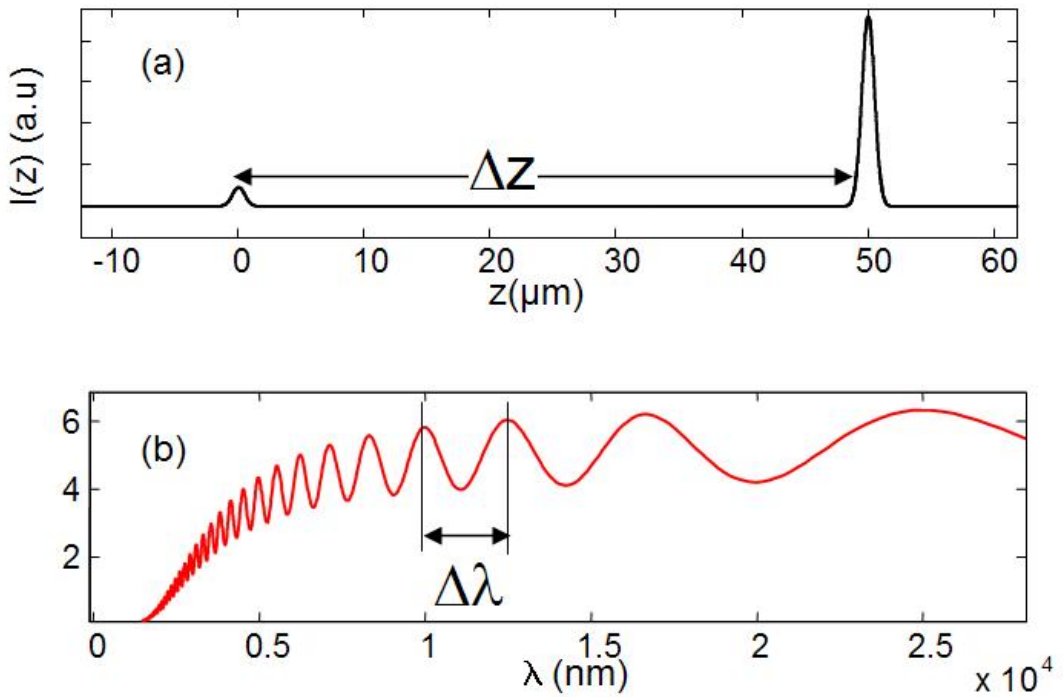


Figure 4.15: (a) Current profile of two Gaussian bunches separated by a distance Δz . (b) The amplitude of the Fourier transform of these two bunches.

spectrum at low energies around 2-3 GeV and another bump at the higher energies. The low energy peak is not visible for higher magnet settings because the low energy particles are deflected out.

There are several reasons we think these are trapped particles: The energies that these particles reach are consistent with the energies from the simulations. And the number of trapped particles are also consistent with the simulations.

The number of trapped particles can be calculated from two diagnostics are that used to look at the energy change of the electron beam after the plasma (the energy gain and energy loss cameras). Unfortunately the energy loss camera used in the experiment shows a strange background increase independent of any physical effect during a two hundred shot event regardless of plasma in or out. Although

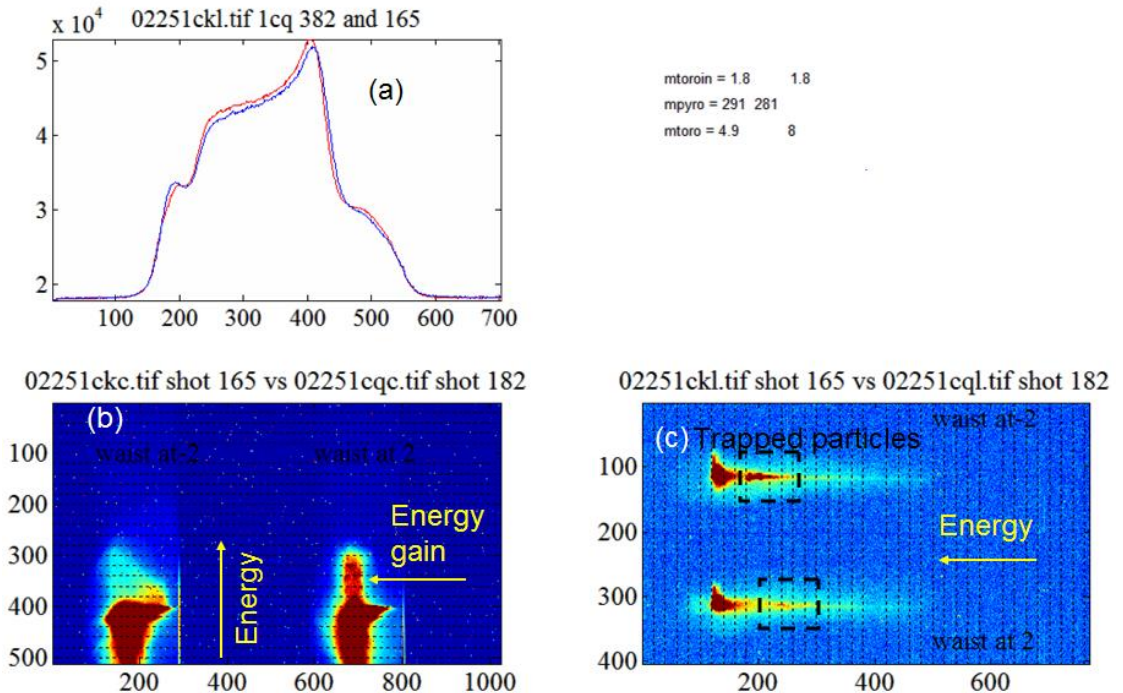


Figure 4.16: (a) X-ray profiles of the two electron beams. (b) Energy spectrum of the two beams and the trapped particles. (c) Energy spectrum of the two beams and the trapped particles.

this is not apparent from the image, this is clear when the number of counts on the image is plotted versus shot number. We cannot account for this since this increase is different for the pixels where trapped particles are and for the pixels where the beam particles are.

Figure 4.22 shows that the number of counts per pixel has two levels for the beam, it jumps from 10 to 60, while counts for trapped particles jump from 5 to 15. This obviously introduces an error. For the two hundred events taken the incoming beam charge is approximately 1.8×10^{10} . This is measured by several current transformers located along the accelerator beam line. The total number of counts on the beam area is supposed to be linear with the measured incoming charge. To calculate the total number of trapped particles we assume that the

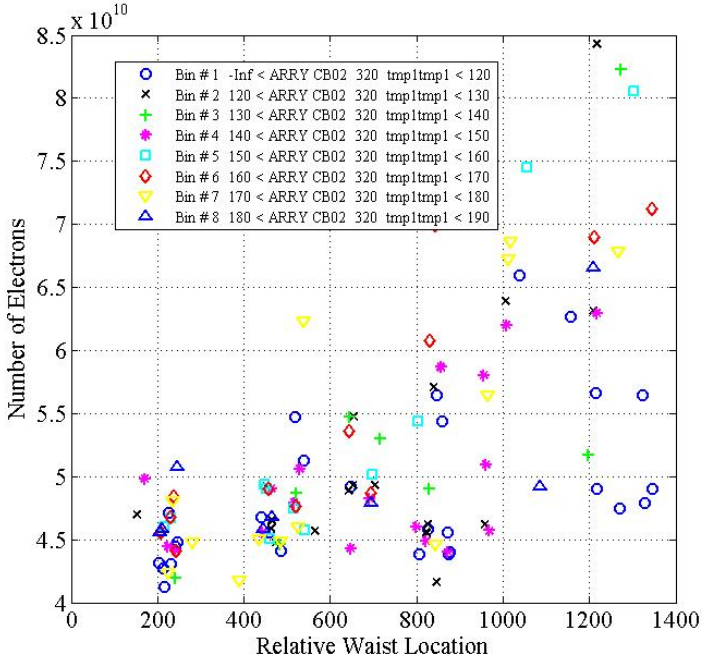


Figure 4.17: Charge measured after the plasma for 7 set of events. Each set represents a different waist position, each set is represented by a different color blue to yellow. Blue represents the set where the waist is located before the plasma source and it is moved further in through each new data set.

number of counts on the beam area is equal to 1.8×10^{10} and by proportionality we convert the trapped particle count to the number of particles. Figure 4.23 shows the energy spectrum of the beam and low energy trapped particles. Using the method explained above the number of total trapped particles are calculated and plotted. This plot shows that the number of trapped particles changes from 4×10^8 to 14×10^8 . Note that the very low energy electrons trapped in the second buffer and below 100 MeV are not visible in this image because they are deflected out by the dipole magnets field. Also note that for these data points the high energy trapped particles overlap with the beam on the image. We assume that they are an order of magnitude less in number and do not affect the total beam count. Figure 4.24 shows the same plots for a higher B field setting where the low

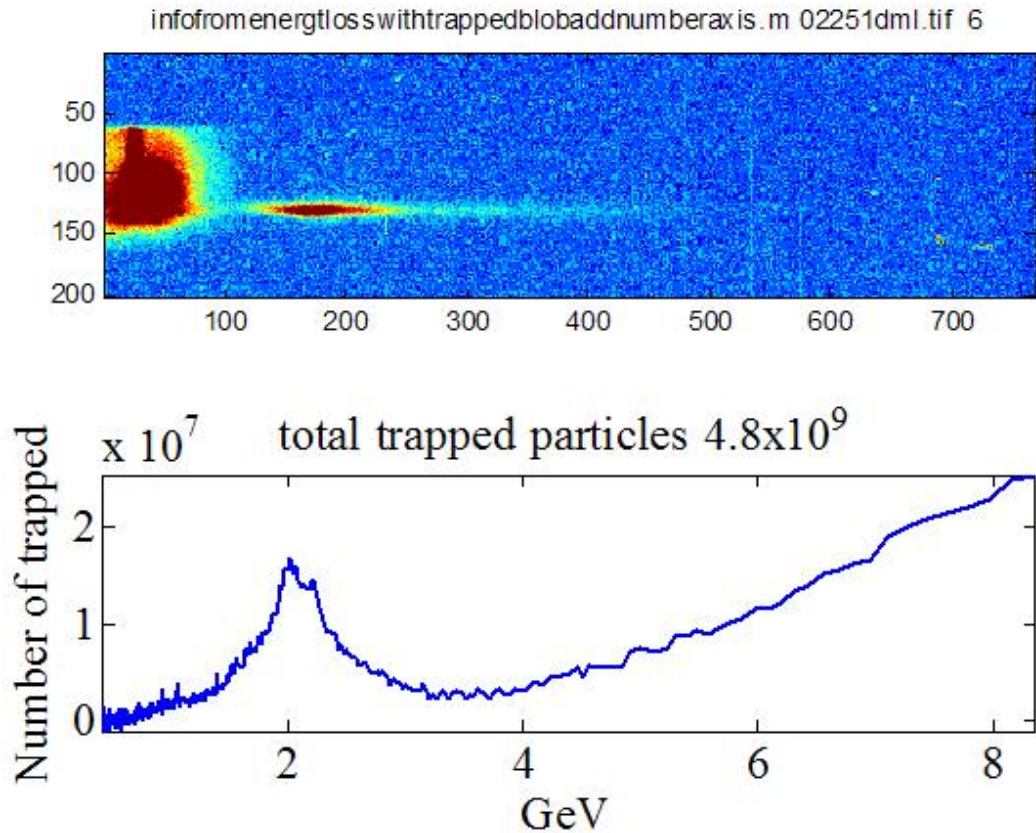


Figure 4.18: Top figure is the energy spectrum of the particles exiting the plasma for $B = 1$ kGauss

energy particles are not on the image anymore and higher energy trapped particles are separated from the beam.

Figure 4.24 shows the same analysis for high energy trapped particles. If this level is correct, then the number of trapped particles is between 2×10^9 and $2 \times 10^9/6$. If the other level is correct then number of trap could be between 1×10^9 to 6×10^9 or so. Therefore the actual number could be anywhere between 0.3×10^9 to 6×10^9 .

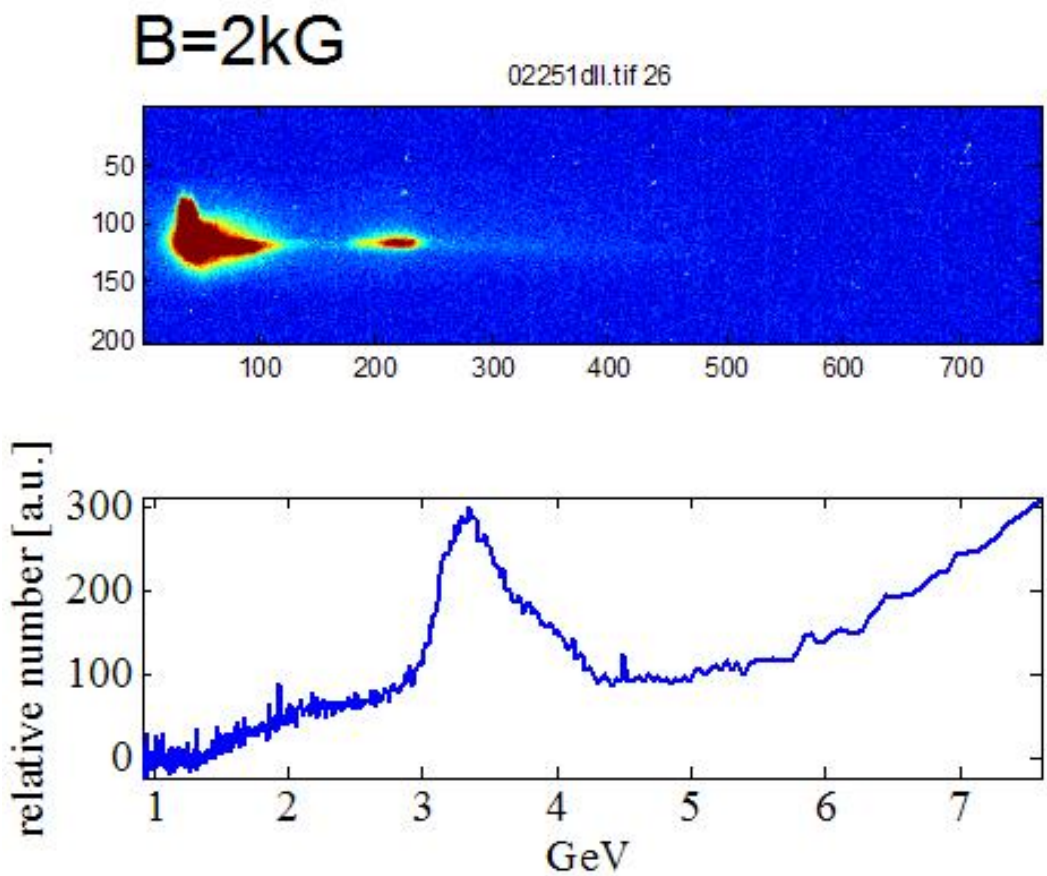


Figure 4.19: Top figure is the energy spectrum of the particles exiting the plasma for $B = 2$ kGauss

infofromenergtlosswithtrappedblobaddnumberaxis.m 02251djl.tif 154

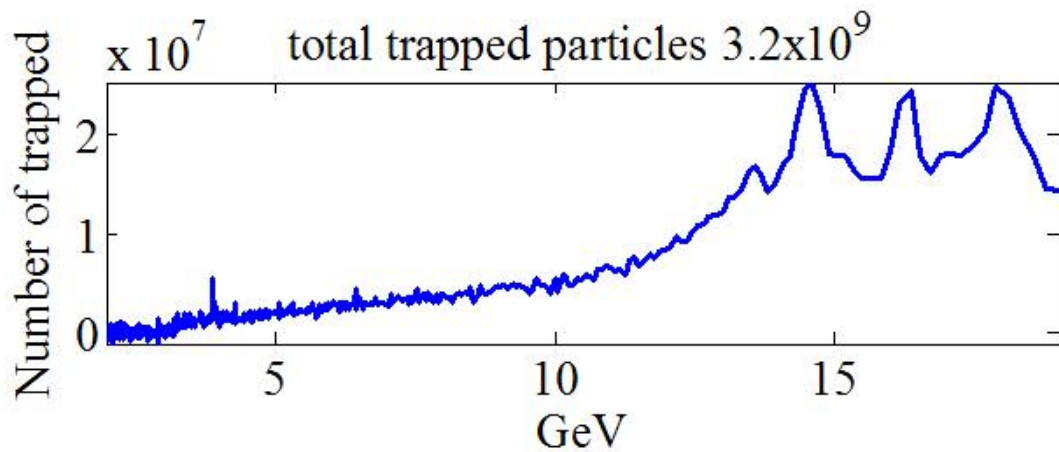
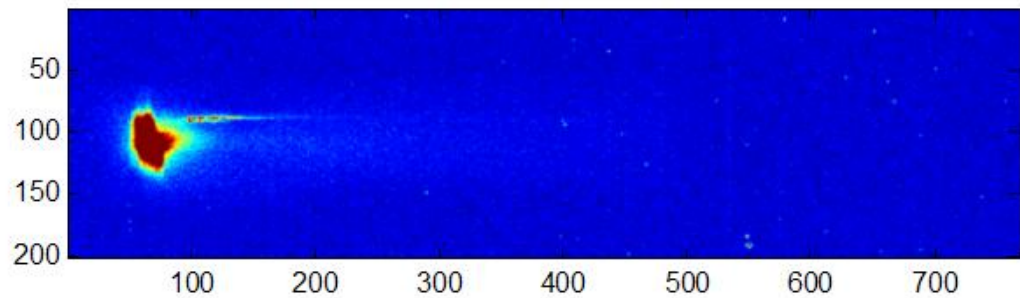


Figure 4.20: Top figure is the energy spectrum of the particles exiting the plasma for $B = 4$ kGauss

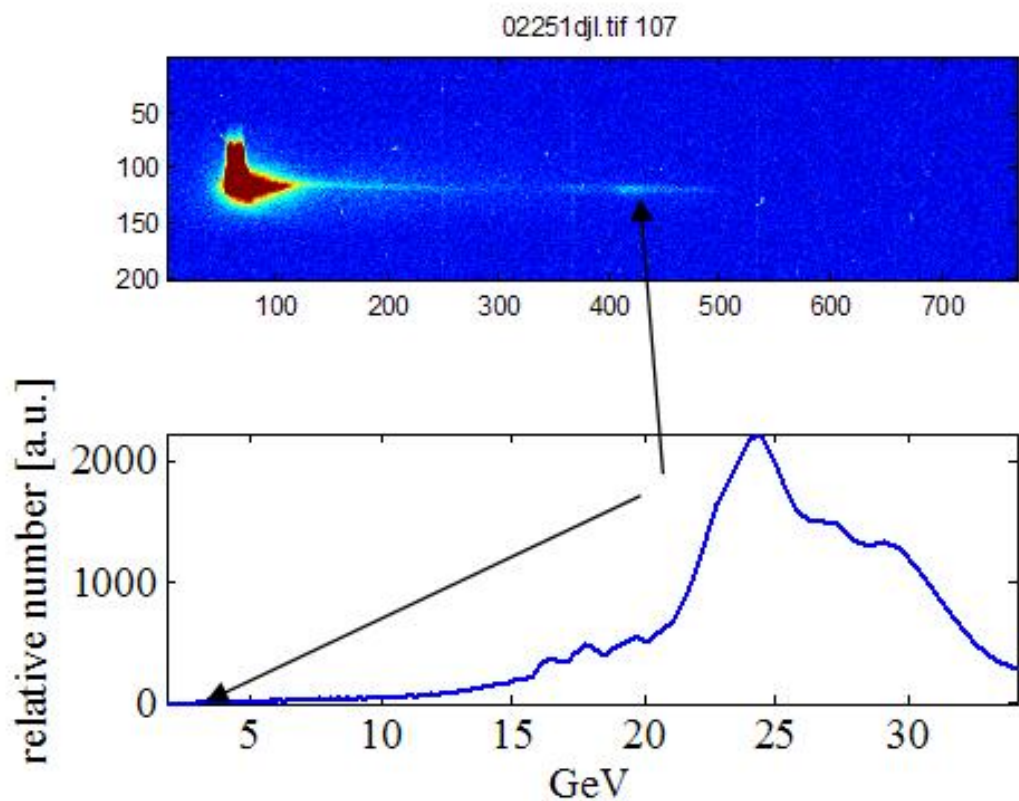


Figure 4.21: Top figure is the energy spectrum of the particles exiting the plasma for $B = 4$ kGauss

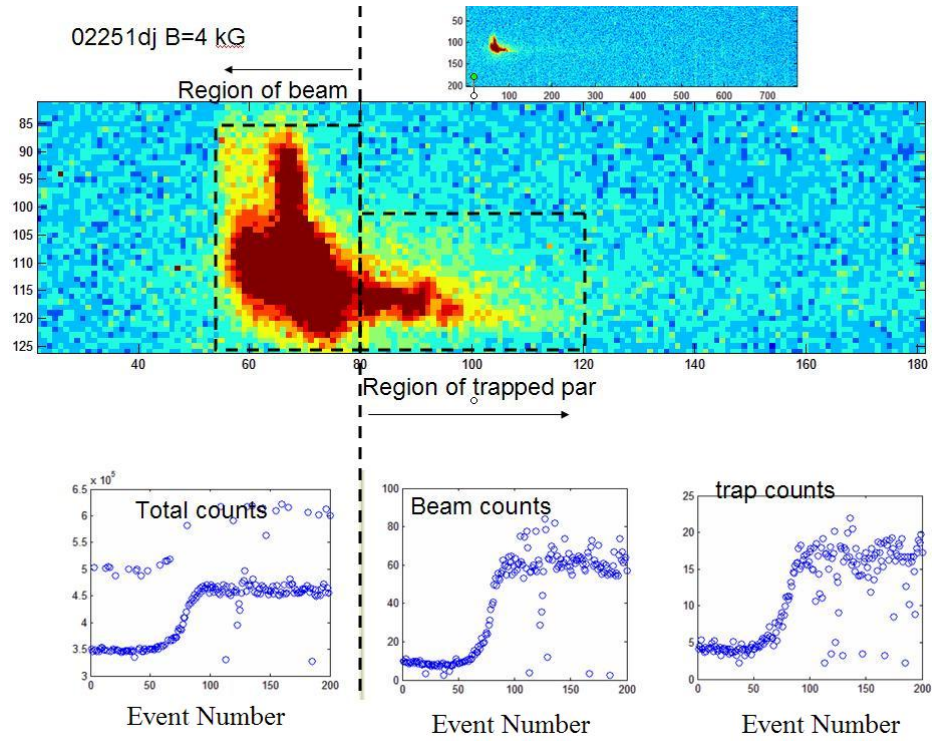


Figure 4.22: Top figure is the energy spectrum of the particles exiting the plasma for $B = 4$ kGauss the dashed rectangles mark the region of beam and trapped particles, the plots show the number of counts on the whole image and on the marked rectangular regions respectively.

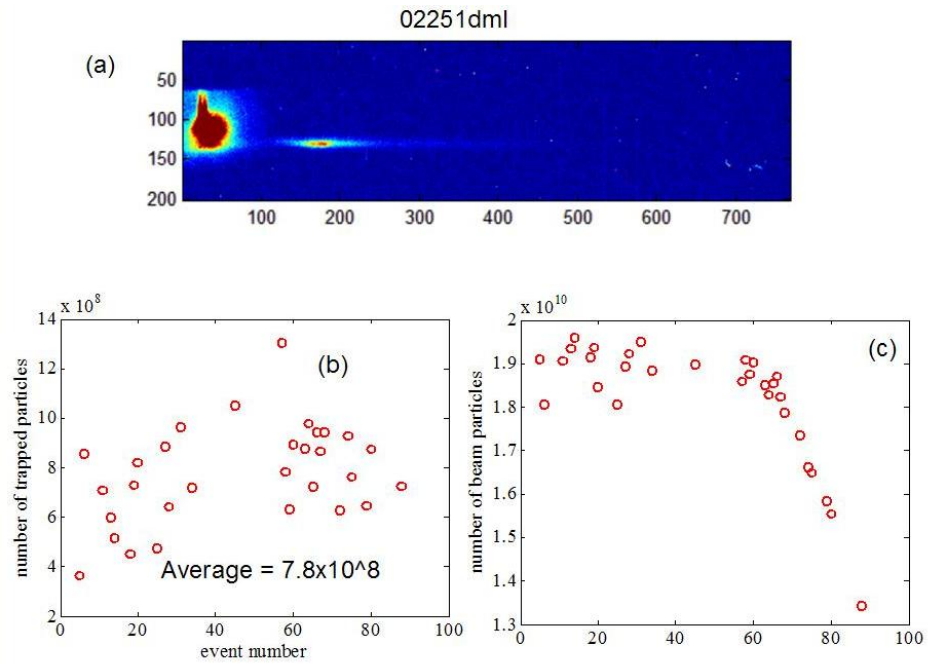


Figure 4.23: (a) The energy spectrum of the particles exiting the plasma for $B = 1$ kGauss trapped particles blob is centered about 2 GeV. (b) The number of trapped particles for several events. (c) Electron beam counts normalized by the first image counts to 1.8×10^{10}

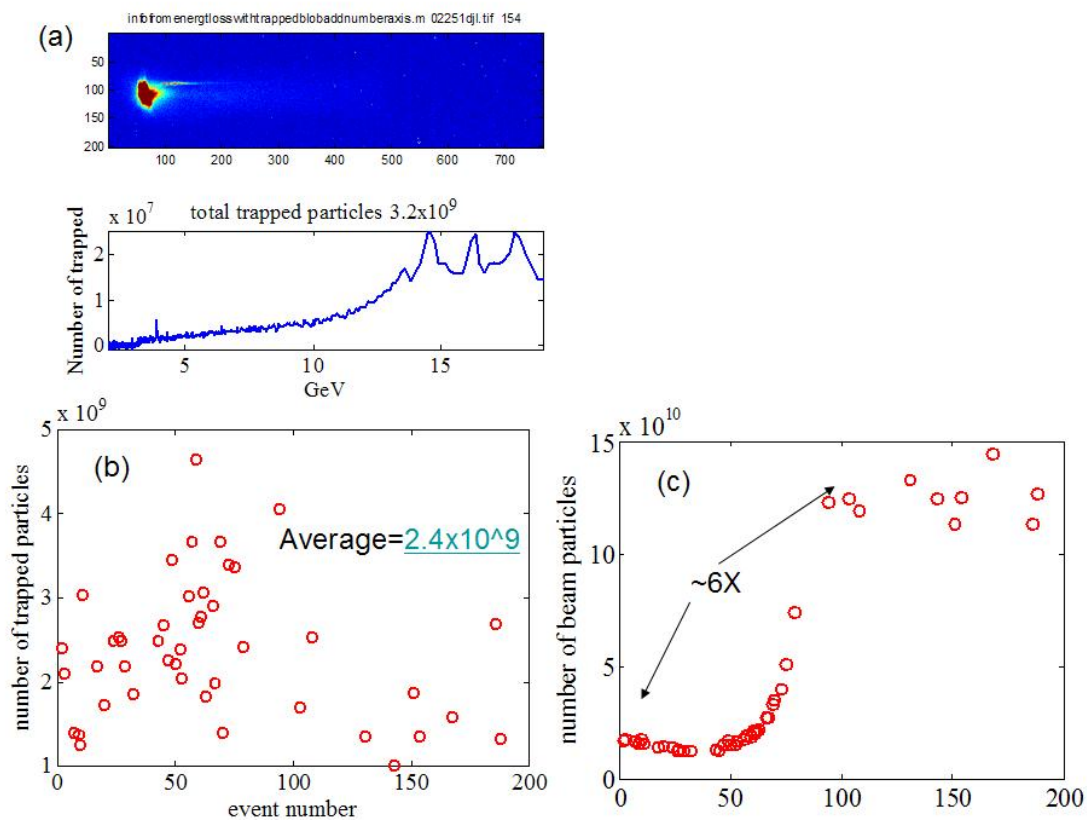


Figure 4.24: (a) The energy spectrum of the particles exiting the plasma for $B = 4$ kGauss. (b) Number of trapped particles for several events. (c) Electron beam counts normalized by the first image counts to 1.8×10^{10} .

Chapter 5

Simulations

In this chapter we complete the picture that we have started painting in chapter 4 (experimental results) with the help of simulations. Experimental results are supported and complemented with results from the simulations, such as the origins of trapped particles, the threshold field for trapping, energy spectrum of trapped particles.

To gain insight into physics of particle trapping we perform 2-D particle-in-cell (PIC) simulations using the numerical code OSIRIS [Hem99, Den05] for the full parameters of the experiment, including the Li and He profiles of Fig. 1.3, as well as the field ionization process [ADK86]. The PIC code OSIRIS solves Maxwell equations on a grid using currents and charge densities without any physics approximations (other than discretization of the differential equations) and pushes the particles using these self-consistently calculated fields and repeats this cycle.

5.1 What are the trapped particles?

The simulations of the experiment reveal that the trapped particles consist primarily of the helium electrons ionized from neutral helium (He I). Simulations also show that the He II and Li II electrons are also trapped. But the total number of these electrons are an order of magnitude less than from He I mainly because the percentage of ionization of these ions is less. Figure 5.1 shows snapshots of Li (a,c) and He (b,d) electrons. The top panels show the electron density in real space

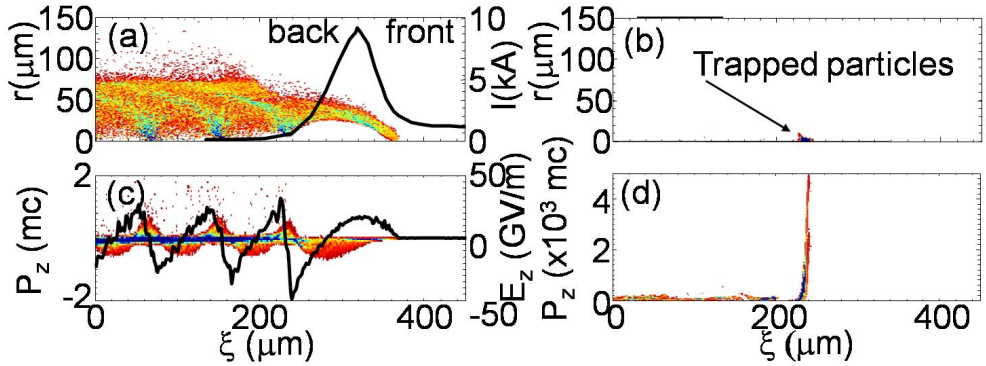


Figure 5.1: 2-D OSIRIS simulation results with the Li vapor and He gas profiles and density of Fig. 1.3(b). The left panels correspond to Li and the right to He electrons. Figures (a) and (b) are real space densities (r - z) at $z = 11.3$ cm (see Fig. 1.3(b)) and (c) and (d) are the corresponding phase space densities ($p_z - z$) at $z = 11.3$ cm and $z = 22$ cm, respectively. The line plot in (c) is the on-axis wakefield E_z . The beam (black line in (a)) has a charge of 1.88×10^{10} electrons, a Gaussian transverse profile with $\sigma_r = 10\mu m$ and a longitudinal profile with FWHM $\approx 65\mu m$ shown by the. The simulation was performed on a moving 500×600 grid ($\Delta z \times \Delta r$, $1\mu m \times 0.5\mu m$) with 25 beam particles/cell and 1 of each gas atoms/cell.

(r- z). The Li electrons are ionized in the bunch front, blown out, return on axis, and support the wake (Fig. 5.1(a)). We observe the He electrons being trapped and bunched in a short ($\sigma_z \approx 2\mu m$ long bunch) region near the peak accelerating field of the first wake bucket ($\xi = 230\mu m$ in Fig. 5.1(b)). The momentum of the Li electrons that are oscillating in the wake Fig. 5.1(c) is much less than that of the He electrons Fig. 5.1(d). The He electrons are focused near the beam axis and in this case reach energies up to 2.5 GeV at the plasma exit, a value similar to that observed in the experiment[K⁺06]. Simulations show that the only difference between helium electrons and lithium electrons is where they originate; He electrons are born inside the wake unlike Li electrons are born in front of the wake because of their lower ionization potential.

5.2 Trapping threshold

In chapter 3 we derived an analytic expression for the trapping threshold (Eq. 3.46). To verify this expression, ideally one would measure the same threshold in the experiment and compare it to the theoretical value. Since in the experiment we can not directly measure the accelerating field or the decelerating field (Fig. 4.3), the threshold wake amplitude is inferred from the average energy loss of the drive beam. We can measure the maximum or the average energy loss for each passage of the electron beam. The only way to convert the energy change to a field amplitude is to assume a plasma interaction length. We can not measure the interaction length experimentally; however, we can assume that the effective interaction length is the FWHM of the lithium gas column. The assumptions that go into this are as follows: The accelerating wake amplitude that the accelerated electrons see is W_{max} in the flat region and $W_{max}/2$ on the up ramp and down ramp. Therefore the energy change for the whole oven is (see fig. 5.2) $2 \times W_{max}x/2 + W_{max}d = W_{max} \times (x + d)(FWHM)$.

Now lets look at the snap shots of the electric field to see if these assumption are verified. Fig. 5.3 (b) shows the on axis longitudinal wake at three points along the plasma. If we look at the Fig. 5.3 (c) we see that the electrons at $\xi = 240\mu m$ gained the most energy and the ones at $\xi = 320\mu m$ lost the most. Fig. 5.3 (b) shows that the accelerating field these electrons see is about 17 GV/m at $z = 5.8cm$, 46 GV/m at $z = 11cm$ and almost zero at $z = 18cm$. The decelerating field the least energetic electrons see is almost constant at three different points and is about 17 GeV. The accelerating field is zero after $z = 18.5cm$ whereas the decelerating field is still considerable for another couple of cms (see fig. 5.4); therefore the FWHM assumption is wrong.

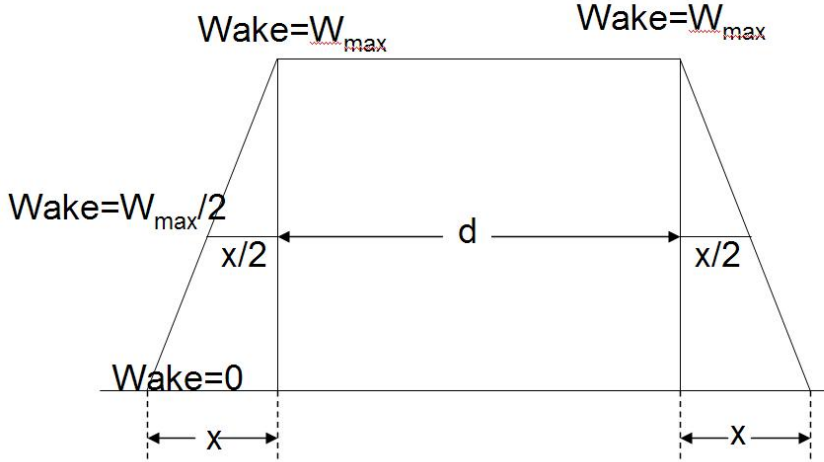


Figure 5.2: cartoon of longitudinal density of lithium vapor. The accelerating wake field amplitude W is estimated at the start middle and the top of the ramp

Fig. 5.4 shows that effectively the decelerating field is felt about twice the distance that the accelerating field is felt. Hence we can not make a direct comparison between theory and the simulation without the help of the simulations. Therefore to connect and compare our theory threshold to the experiment, we find the average energy loss in the simulation of Fig. 5.1 which is carried out for the exact parameters of the experiment. The peak field of 40 GV/m in that simulation corresponds to an average energy loss of 1 GeV. Using this proportionality factor, the observed trapping threshold at $E_{loss} \approx 0.9\text{GeV}$ in Fig. 4.3(a) implies a trapping threshold field of $\approx 36\text{GeV/m}$. Now lets see what our theory model predicts.

To reduce the simulation time while investigating the threshold, a short plasma profile (Fig. 5.5) is used where the plasma density is quickly ramped up to match the peak density of the measured profile seen in Fig. 1.3, and an arbitrarily small amount of He is introduced along the Li profile. The beam and trapped electrons exit the plasma through a short vacuum section. A threshold plot is produced using

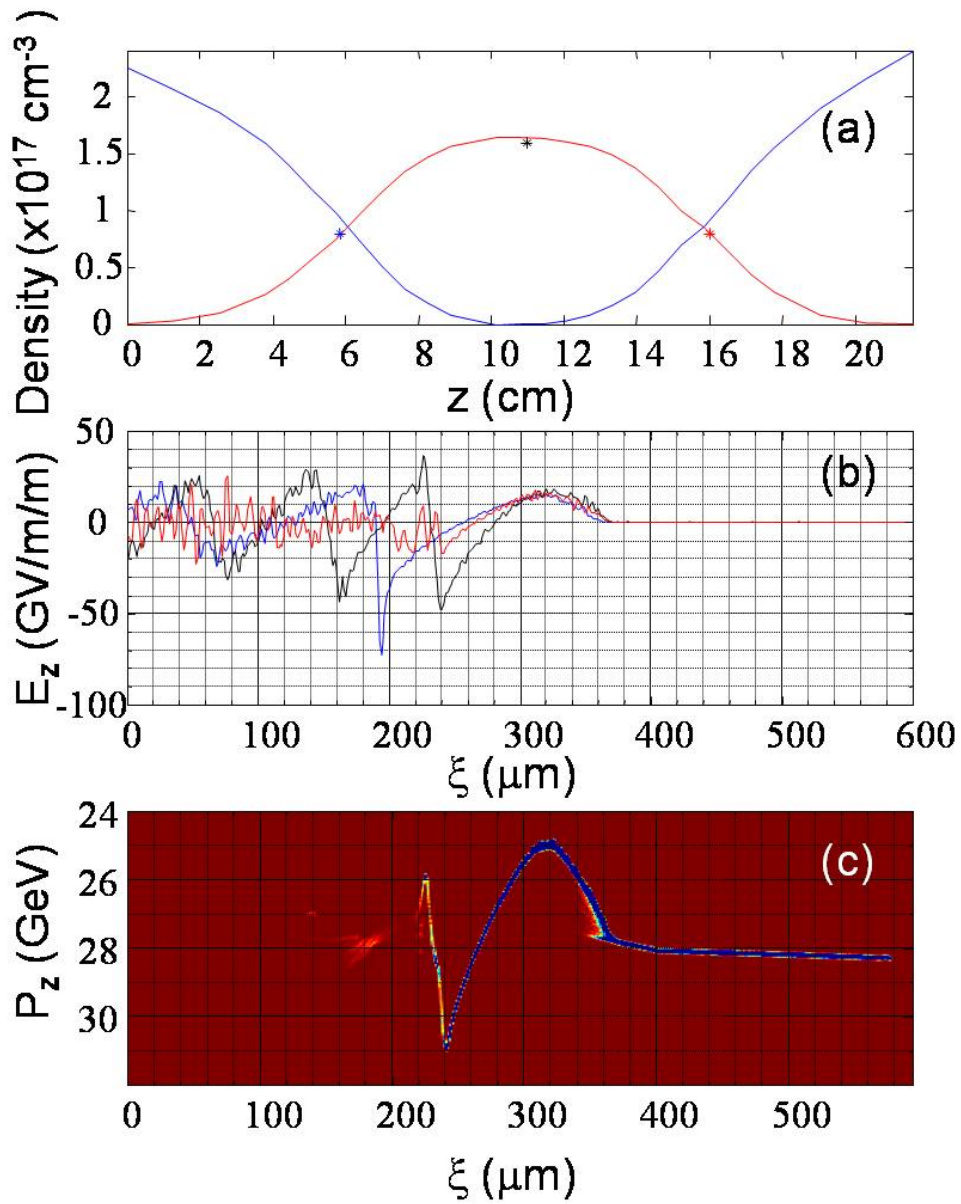


Figure 5.3: (a) Oven profile used in the simulation (same as Fig. 1.3). Stars indicate the position of the electron beam for the following plots. (b) On axis longitudinal field E_z at three positions: $z=5.85$ cm where density is $n_0/2$ (blue line), $z=11$ cm where density is n_0 (black line), and $z=16$ cm where density is $n_0/2$ (red line). (c) Phase space P_z vs z of the electron beam at the end of the oven

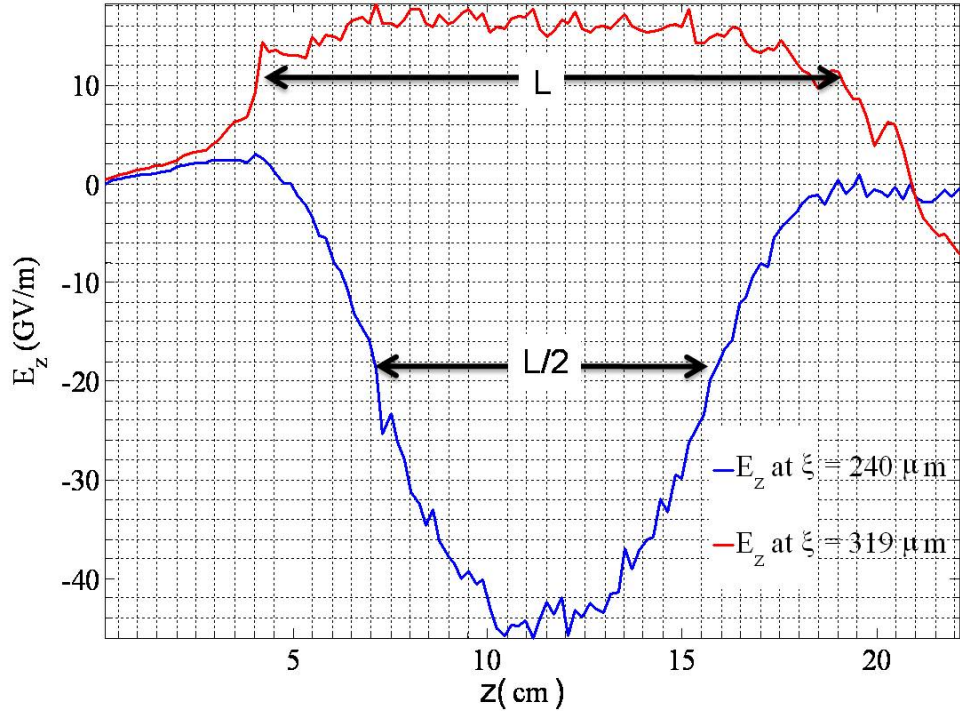


Figure 5.4: Longitudinal electric field at $\xi = 240\mu m$ (red line) and $\xi = 320\mu m$ (blue line) vs distance in the plasma

this short gas profile (Fig. 5.6). We change the wake field amplitude by changing the charge and therefore changing the peak current of the drive beam. The number of trapped electrons is counted using the phase space of helium electrons in the vacuum. The peak wake field amplitude that traps the electrons is taken to be the one on the peak of the lithium density and the slope k is also calculated at this point in the simulation. The electron beam profile used in the this simulations is shown in Fig. 1.3. We plot the number of trapped He electrons as a function of the accelerating field E_{useful} . Trapping is observed when the $E_{useful} > 30$ GV/m. Both in these simulations and in the experiment (Fig. 4.3) there is a sudden increase in the number of trapped particles when the wake amplitude is

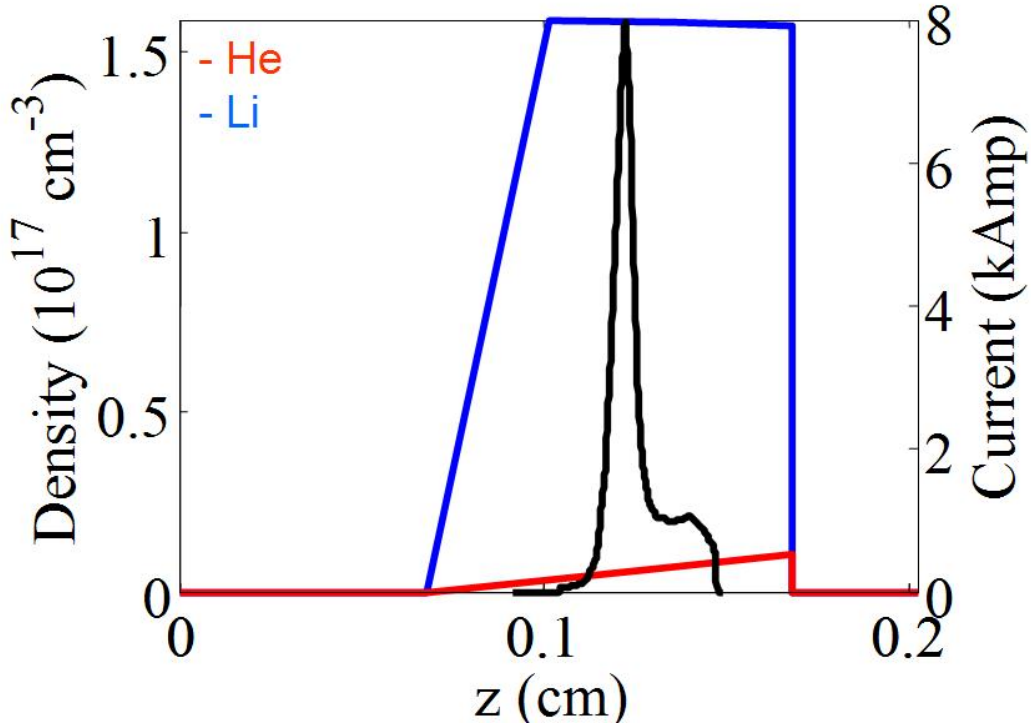


Figure 5.5: Simulation gas profile used, blue line is the lithium gas and the red line is the helium gas, black line is the same electron beam current that is used in the case of Fig. 5.1 except the peak current is less in the example shown and the beam spot size is made five times smaller to account for the plasma focusing.

increased. Equation (3.46) is also plotted in Fig. 5.6 (dashed vertical lines) using the values of k obtained from E_z of the short simulations described above. Trapping is observed only for simulations where the peak accelerating field is higher than the trapping threshold (Eq. 3.46), i.e. when the colored circles are to the right of the lines of same color in Fig. 5.1. The onset of trapping occurs at $E_{useful} \approx 30$ GV/m, compared to the experimental value of 36 GV/m. Therefore experiment simulations and theory have very good agreement.

Note, simulations without He buffer gas show that no Li electrons are trapped over the range of fields shown in Fig. 5.6. Note also that the number of trapped

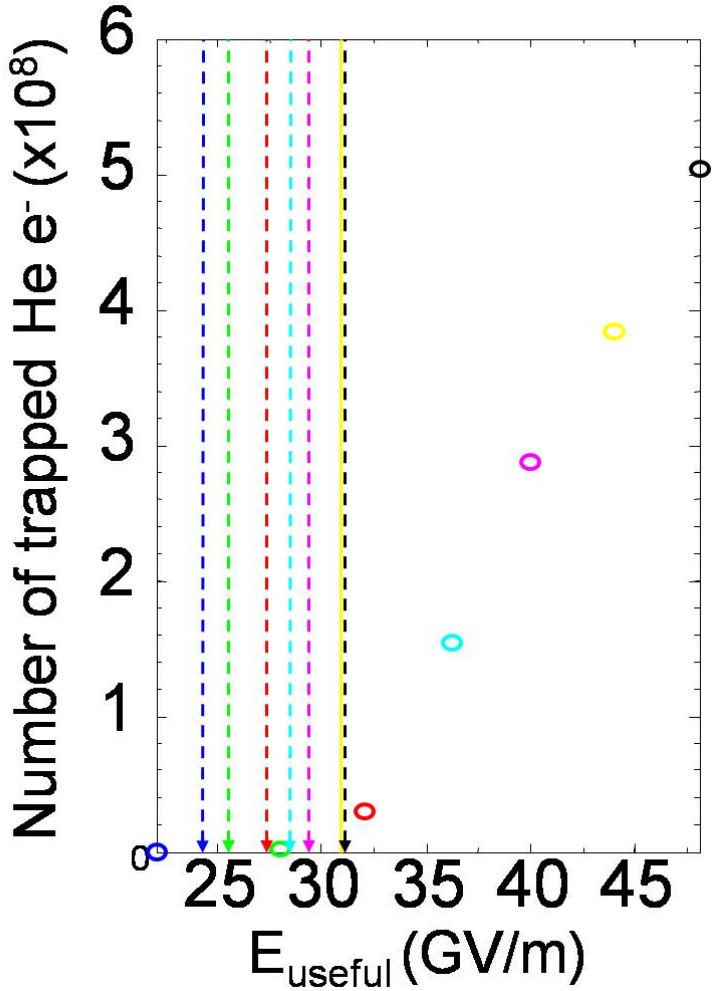


Figure 5.6: Number of trapped He electrons (circles) as a function of the peak accelerating field obtained from simulations with $n_0 = 1.6 \times 10^{17} \text{ cm}^{-3}$, and a bunch charge increasing from 0.4 to 1 times $1.8 \times 10^{10} e^-$. The dashed vertical lines show the trapping threshold (Eq. 3.46) from the values of $k = \frac{dE}{d\xi}$ obtained from the same simulations. Circles and the lines of the same color corresponds to the same simulation. The same current profile as in Fig. 5.1 has been used but $\sigma_r = 2.4 \mu\text{m}$.

electrons in Fig. 5.6 is much smaller than that in Fig. 4.3(a). It is the result of trapping of low density He over the short plasma length used in the simulation while in the experiment electrons are trapped in both buffer regions of the oven (Fig. 1.3).

Now lets look at an alternative way of deriving the threshold from simulations. The number of helium electrons above 10 MeV is plotted in Fig. 5.7. Figure 5.7

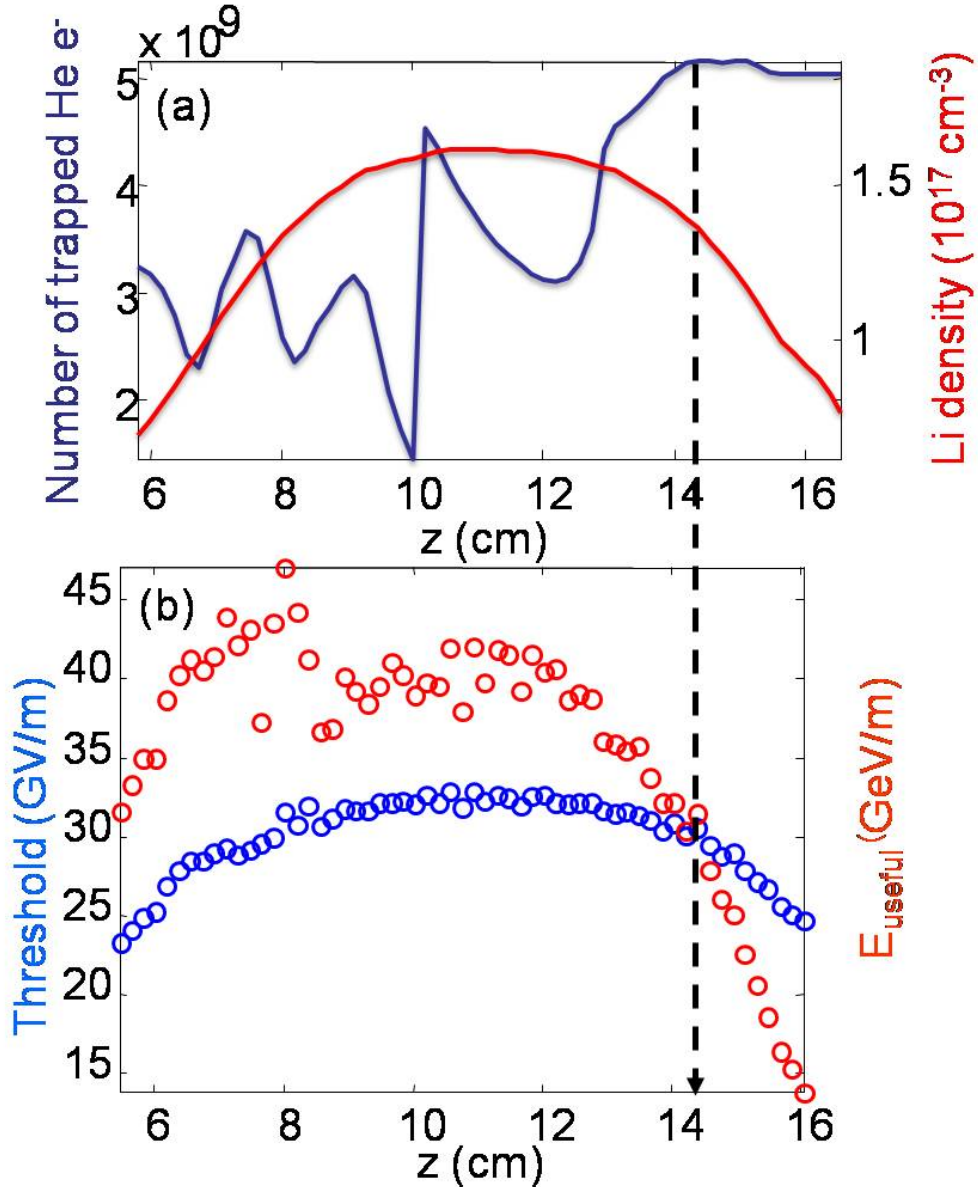


Figure 5.7: (a) Number of trapped electrons along oven (overlaid is the lithium density) (b) Threshold along oven (blue circles), E_{useful} along oven (red circles)

(a) and (b) are from the full simulation of the experiment Figure 5.7 (a) is the plot of the number of helium electrons above 10 MeV versus position of the beam in the

oven (blue line). The red line is the lithium gas profile. A black dashed line shows where the helium trapping stops. Figure 5.7 (b) is the plot of the theory threshold (Eq. 3.46) versus beam position in the oven (blue circles); the value of k in Eq. 3.46 for the threshold is obtained from the linear fit to the on axis wake in the simulation. Also plotted is E_{useful} (red circles). The significant point is that the z location where E_{useful} becomes less than the threshold is also where trapping stops. So this single simulations show that the threshold is at 30 GV/m. Figure 5.7(b) also shows that the E_{useful} changes by about 20 percent. The average value of E_{useful} over the trapping regions is about 39 GV/m which is approximately the E_{useful} in the peak density region. In figure 5.8 we plot the value of $\Delta\Psi = \Psi_{max} - \Psi_{min}$ (Eq. 3.45) and as expected from the Eq. 3.45 the location where $\Delta\Psi$ becomes less than the threshold in Ψ 0.5 MV (blue line) is the location where trapping stops.

Using this way of looking at the threshold we also verified that threshold is indeed independent of γ of the beam. We obtained the same threshold with a drive beam of 14 GeV energy.

5.3 Effect of trapped particles on energy gain

In conventional accelerators dark current is a fundamental limit on the maximum acceleration gradient that can be obtained. It is then natural to ask if trapped particles, i.e. plasma dark current, is the limiting factor on the accelerating gradient in a plasma? We attempt to answer that question in this section.

In laser wake field accelerators trapping is the mechanism of producing the accelerated bunches. The plasma is driven to the point of wave breaking, and just like the white water that we see when an ocean wave breaks, plasma electrons get

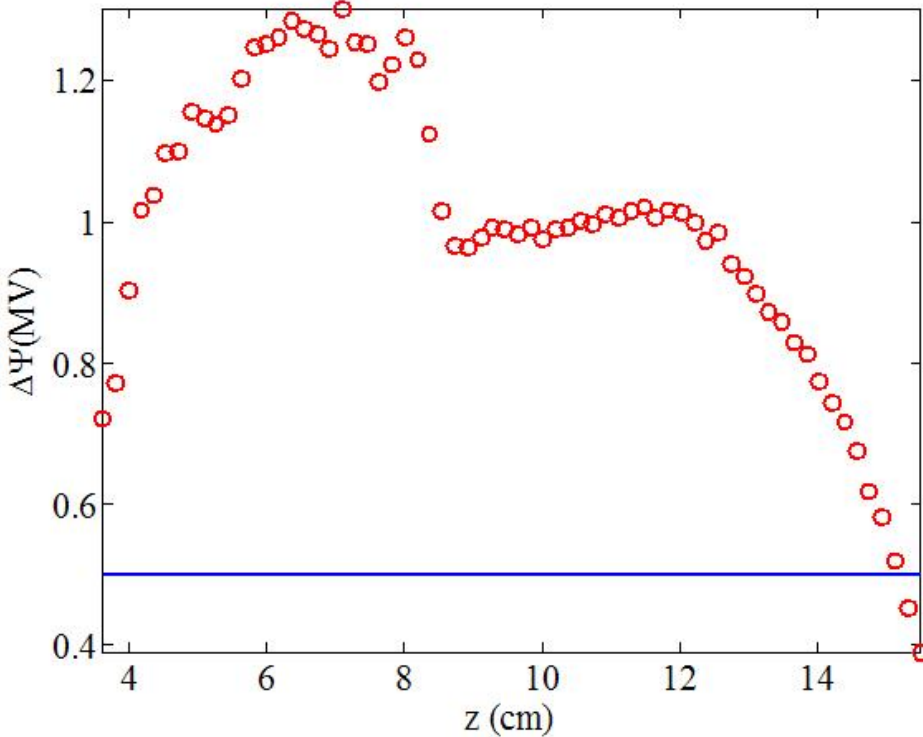


Figure 5.8: Value of $\Delta\Psi = \Psi_{max} - \Psi_{min}$ (Eq. 3.45) as a function of beam position (red circles). Blue line is the threshold for trapping ($\Delta\Psi = 0.5 mc^2$)

trapped and load the wake. They phase slip to the bottom of the potential. By choosing the right plasma length a mono-energetic bunch can be produced.

In our case the trapped particles are a priori unwanted because they are taking energy from the wake that could be used to accelerate the electrons of the witness beam or the electrons located at the back of the electron beam. However the simulations show that the location of the trapped particles are at and behind the peak of the accelerating wake therefore they should have a little effect on the maximum energy of an electron located at the peak. Moreover the double bunch experiments suggest that the best place to locate the witness beam is near and on the forward direction of the peak [H+06]. Hence trapped particles would have no effect at all. Moreover, we may expect that sufficient external beam load

would reduce the wake below the threshold for trapping and eliminate trapping all together.

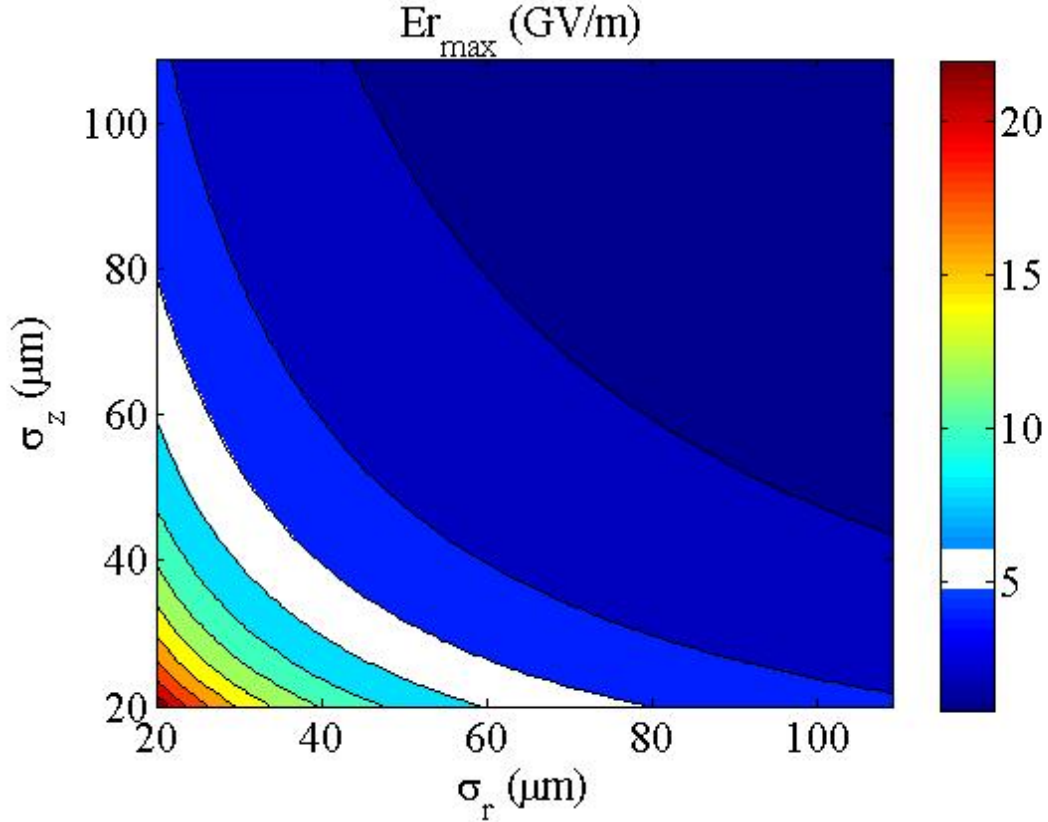


Figure 5.9: Maximum radial field of a Gaussian bunch is calculated for various beam rms spot size (σ_r) and bunch length (σ_z). The white contour corresponds to the tunneling ionization threshold for various bunch lengths

There are other possibilities to avoid trapping. One may think of moving the waist of the beam later than the buffer in order not to ionize helium and lithium. The peak radial field of a relativistic Gaussian electron bunch is plotted in Fig. 5.9. The white region corresponds to the thresholds for tunneling ionization for various bunch lengths (Varying bunch length from 20 to 100 microns changes threshold by about 1 GV/m). This shows that if the electron beam parameters are such that the maximum field is below the threshold then electron initial trapping can

be avoided. In the experiment the nominal spot size value was $10 \mu\text{m}$. The waist of the beam was changed and its looks possible that there may be cases where nothing was ionized in the buffer avoiding the trapping.

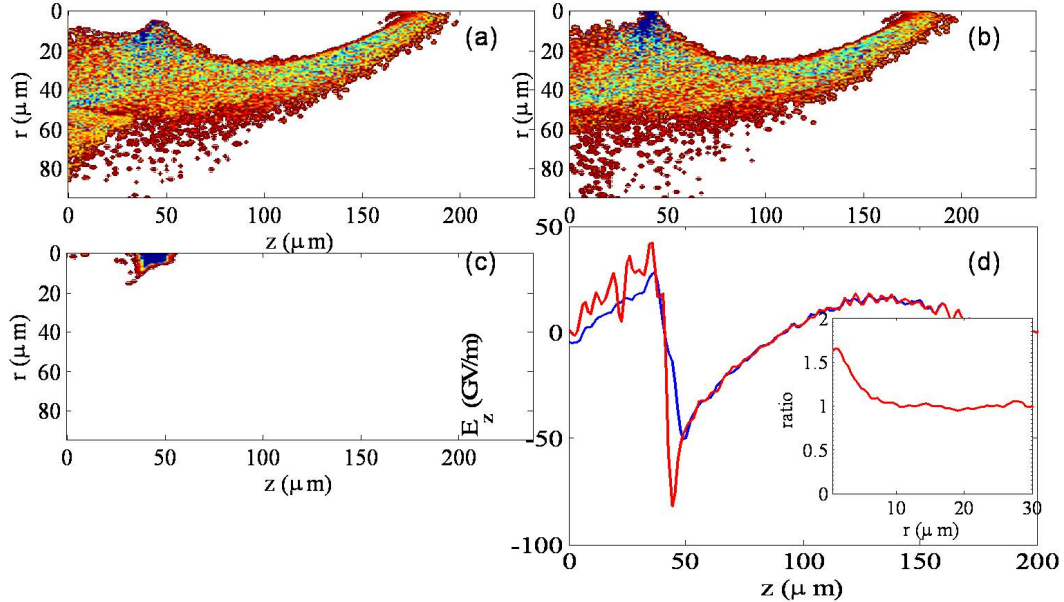


Figure 5.10: (a)Real space (r - z) of Li electrons from an Osiris simulation (at a location of the simulation box in the middle of the oven profile Fig. 1.3). (b) The same as (a) except in the simulation there is no He. (c) The real space of He electrons. (d) The blue line is the E_z on axis from the simulation with He, and red line is from the simulation with no He. The inset shows the ratio of peak on-axis field at different r positions

In the simulations unlike the experiment we can remove Helium. When this is done keeping the beam parameters and lithium density the same, we see a considerable reduction in the peak accelerating field. However this can not be explained by drive beam loading. The reason becomes obvious when we compare two plasma wakes by looking at the real space of the Li electrons. Fig. 5.10 (a) shows that the Li electrons cannot come back to axis unlike the case when there

is no trapping (Fig. 5.10 (b) because of the trapped He electrons located on axis (Fig. 5.10 (c)) and this causes the accelerating field (Fig. 5.10 (d) blue line) near the axis to be much less (about 40 percent in this case) than the case with no He (Fig. 5.10 (d) red line). Alternatively, this reduction can be stated as beam loading by the trapped particles. The inset in Fig. 5.10 (d) show the ratio of peak accelerating field for the two cases as a function of radius.

Chapter 6

A Brightness Transformer Using a Beam Driven Plasma Wake Field Accelerator

High brightness (B) electron beams are essential for colliders and for radiation sources such as the X-ray Linear Coherent Light Source (LCLS) FEL at Stanford Linear Accelerator Center (SLAC), the Berkeley Advanced Light Source (ALS), and the Argonne Advanced Photon Source (APS). Currently operational state of the art photo injectors can produce electron beams with brightness as high as $1 \times 10^{13} A/(mrad)^2$ [Sch04]. Here we introduce a new scheme for producing an ultra high brightness beam with brightness two orders of magnitude greater than this. The idea is illustrated in Fig. 6.1. An ultra relativistic electron beam ($\gamma = 56000$) enters a passive gas or vapor, ionizes it, and drives a large amplitude plasma wave that traps a short bunch.

As was demonstrated in chapters 4 and 5, electrons are trapped when the short wavelength (with λ_p few tens of microns) plasma wake amplitude exceeds a threshold value of ≈ 30 GV/m. Numerical simulations show that these electrons are He ($\Phi_{He} = 23.5$ eV) electrons born inside the wake itself, through ionization by the focused electron bunch. The trapped electrons born at rest quickly slip back in the wake, bunch near the peak of the accelerating field and form an ultra-short bunch [ODK⁺07].

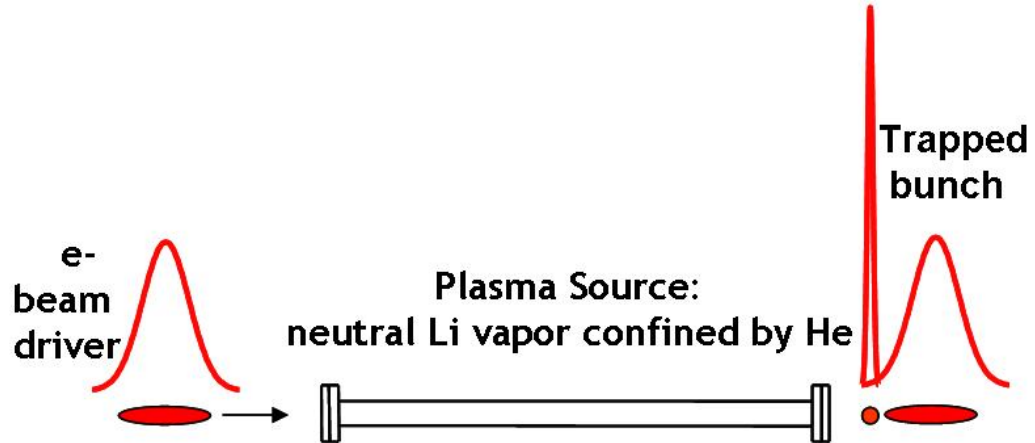


Figure 6.1: Schematic of the brightness transformer.

To obtain the parameters of the trapped electron bunch we again perform 2D particle in cell (PIC) simulations with the fully relativistic, PIC code OSIRIS [Hem99]. The simulations are performed on a moving 200×400 grid with 25 beam particles/cell and 1 of each gas atoms/cell of cell size $\Delta z \times \Delta r = 1.2 \mu m \times 0.25 \mu m$. The Li vapor and the He gas profiles used in the simulation are shown in Fig. 6.2 and corresponds to those in a heat-pipe oven [MMW⁺99]. As an example we use beam parameters similar to those of the beams available at the Stanford Linear Accelerator Center: a charge of 1.45×10^{10} electrons, a Gaussian transverse profile with FWHM $\approx 10 \mu m$ and a longitudinal profile with FWHM $\approx 65 \mu m$, corresponding to a peak current of 20 kA. The beam current profile is shown in Fig. 6.2(a). Simulations show that the He electrons that are trapped in the initial buffer zone (Fig. 6.1) form an ultra-short bunch. The trapped bunch has a FWHM of $\approx 2 \mu m$, much shorter than the drive bunch, a radius of $\approx 0.3 \mu m$ and has a peak current of 20 kAmps, also higher than that of the drive bunch

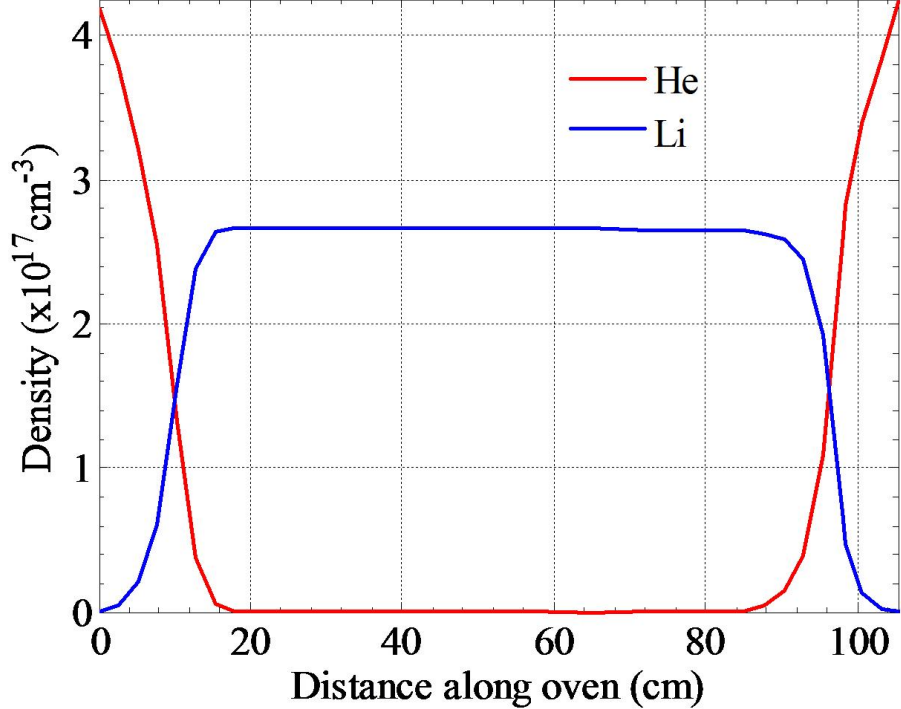


Figure 6.2: Longitudinal density profiles of lithium vapor (blue line) and helium gas (red line) in the plasma source for a vapor and plasma density of $2.7 \times 10^{17} \text{ cm}^{-3}$. At this density the plasma wavelength is of the same order as the bunch length. The pressure is constant along the oven while the Li vapor has a temperature of $\approx 1300 \text{ K}$ and the He gas is at room temperature far from the hot Li vapor.

(Fig. 6.3(a)). The energy spectrum of the trapped particle bunch is shown on Fig. 6.3(b). The rms energy spread of the trapped bunch (calculated from the FWHM of the distribution) is less than 2 percent. The emittance of the trapped particle bunch is $\approx 5 \text{ mm-mrad}$. We calculate the brightness of the trapped particle bunch using the simulation results to be:

$$\begin{aligned} B_N &= \frac{2I_{peak}}{\epsilon_N^2} \\ &\approx 2 \times 10^{15} A / (\text{mrad})^2 \end{aligned} \tag{6.1}$$

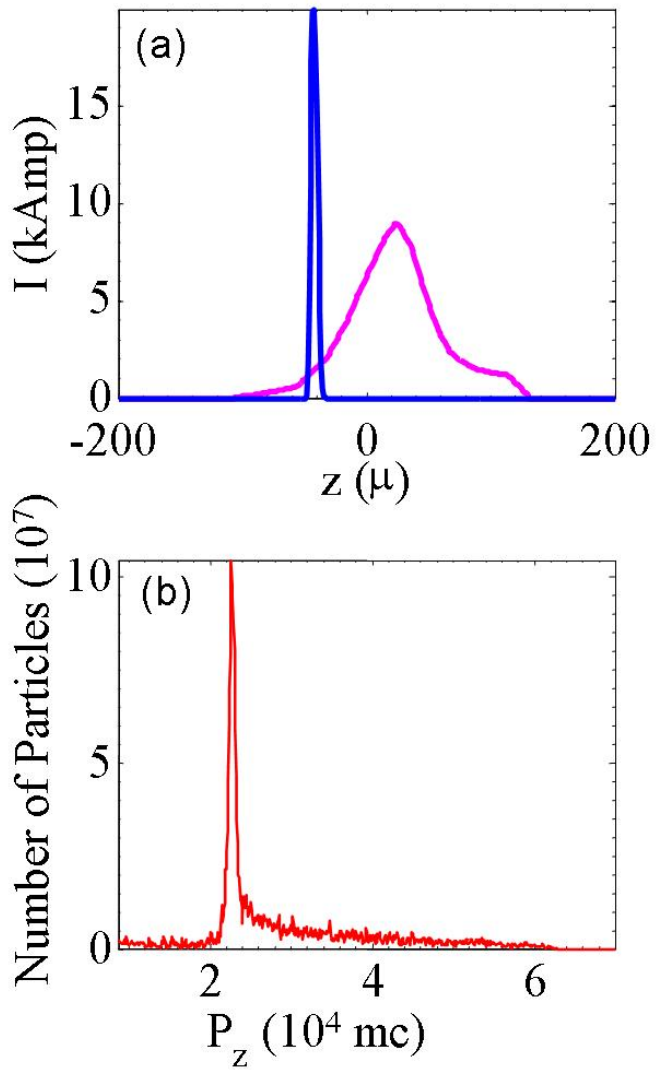


Figure 6.3: Simulation results obtained with the 2-D OSIRIS PIC code, using the plasma profile of Fig. 6.2: (a) Longitudinal profile of the drive bunch (pink) and the trapped particles bunch (blue). (b) Energy distribution of the trapped particle bunch at $z = 84$ cm.

two orders of magnitude higher than the brightness of the drive beam ($\approx 4 \times 10^{12}$). Therefore the plasma wake field transforms the brightness of the drive beam to a much higher value.

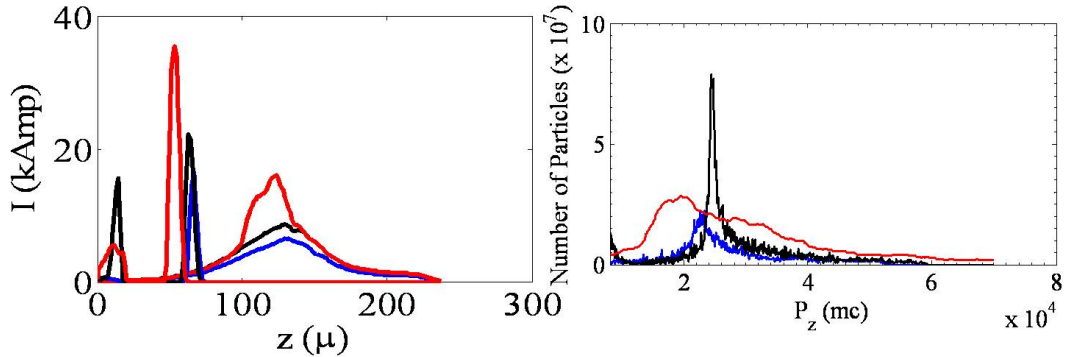


Figure 6.4: OSIRIS simulations with three different drive beams, the gas profiles are the same as in Fig. 6.2 (a) Drive beam and trapped particle current profiles. (b) Energy spectrum of the trapped bunches

| | Case1 | Case2 | Case3 |
|---|-----------------|-----------------|------------------------------------|
| Peak drive beam current (kA) | 6.5 | 8.6 | 16 |
| Number of trapped particles in the bunch | 2×10^9 | 3×10^9 | 6×10^9 |
| Emittance (mm-mrad) | 7.5 | 5.0 | 11.4 |
| Peak current of trapped bunch (kA) | 16.4 | 22.2 | 35.5 Combination of (27.6 + 10) |
| Plasma wavelength (μm) | 91.6 | 100.7 | 110.5 |
| Peak of the energy spectrum (GeV) | 1.1 | 1.15 | 1 |
| Peak accelerating field (GV/m) | 40 | 45 | 55 |
| FWHM of trapped bunch | 5.5 | 6.5 | 8 combination of (6.5 and 10) |
| Brightness ($\times 10^{15}$ A/mrad2) | 0.6 | 1.8 | 0.6 |

Figure 6.5: OSIRIS simulations with three different drive beams.

We also performed simulations to see how the brightness of the trapped particle beam brightness changes when the drive beam current is varied (see table 6.5). Figure 6.4 shows that as the drive beam amplitude is increased, the peak current of the trapped particle beam increases as a result of the larger plasma wake. The emittance also improves compared to the lowest current driver case; however for the highest driver the emittance increases. This is a result of the ionization and

trapping of the second electron of helium. The only difference between the helium electron trapping and helium ion electron trapping is that after the electron beam is focused the helium gas tunneling ionization threshold is reached and the radial fields stay above threshold. Therefore there is a continuous trapping for helium electrons in the buffer region. However the threshold for helium plus ionization is reached only when the beam is at a minimum of a betatron oscillation when the radial field is maximum. This causes broadening of the trapped bunch and also worsens both the emittance and energy spread of the trapped helium electrons. Fig. 6.6 shows the phase space of helium electrons where this multiple branching occurs because of the betatron oscillations.

Simulations also show that the trapped particle beam is so intense that it ionizes helium and forms a helium wake throughout the helium only region. Just like the slac beam driver the trapped particle beam starts lose most of its energy in this section.

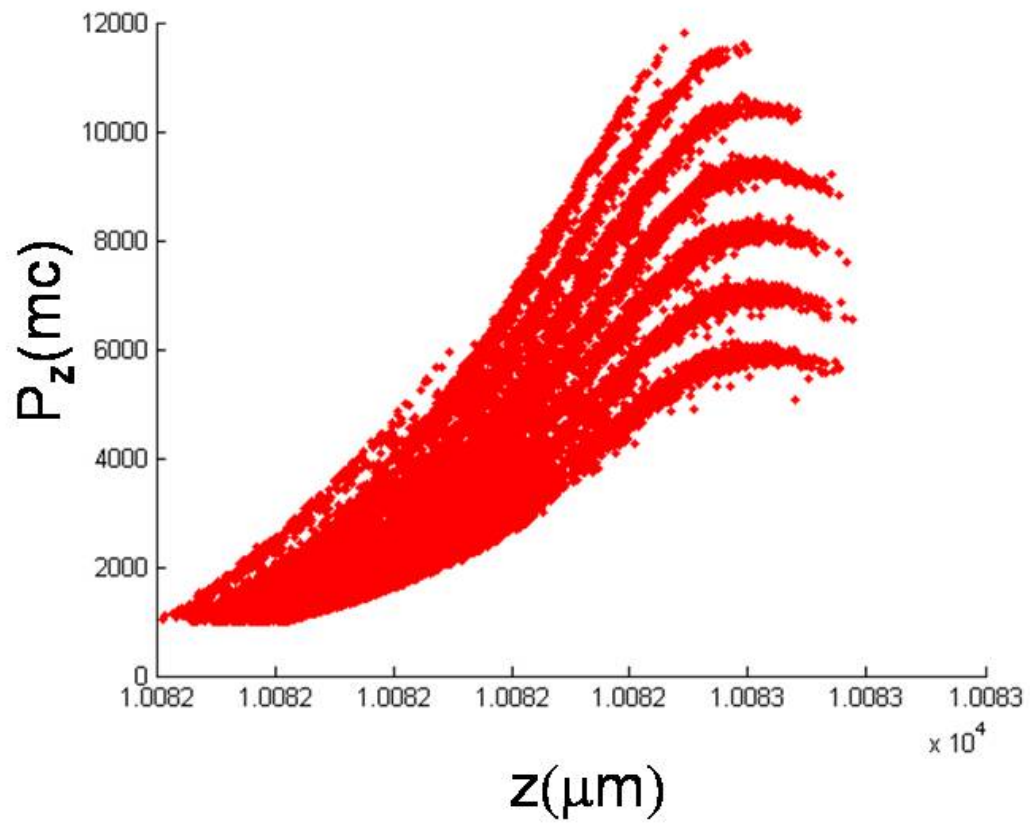


Figure 6.6: Phase space of trapped helium plus electrons from OSIRIS simulation.

Chapter 7

Future Work

In this chapter we discuss new ideas for future experiments to get higher brightness electron beams and present the results of OSIRIS simulations testing these ideas.

7.1 An alternative buffer gas

One way to increase the brightness of the trapped particle bunch is to increase the number of trapped electrons by making use of multiple ionization of the buffer gas. We know from the simulations presented in the previous chapter that as long as the radial fields in the plasma stays above the threshold for ionizing these second electron of the gas for the whole length of the buffer, the phase space of the trapped electrons from the second ionization should be similar to that of the first, and hence the brightness of the trapped particle beam should increase.

The idea of using a new buffer gas is tested using the same drive beam and the same density profile as in Fig. 6.2 but replacing helium with argon (Ar). Ar is chosen because of the low threshold of ionization for the subsequent ionization states (see table 7.1).

The results are shown in Figure 7.2. Although total trapped particle current is higher as a result of multiple ionization of argon, the energy spectrum is much broader and emittance is worse for the same reasons as the high current drive beam simulation where helium plus electrons worsen the brightness (Chapter 6). The

| Ionization level | Ionization energy (eV) He | | |
|------------------|------------------------------|---------|---------|
| | | Li | Ar |
| 1st | 24.587 | 5.392 | 15.759 |
| 2nd | 54.416 | 75.638 | 27.629 |
| 3rd | | 122.451 | 40.74 |
| 4th | | | 59.81 |
| 5th | | | 75.02 |
| 6th | | | 91.007 |
| 7th | | | 124.319 |

Figure 7.1: Ionization energies of He, Li and Ar.

brightness of argon trapped particle beam is $0.8 \times 10^{15} A/mrad^2$ and is lower than the case when He is the buffer gas.

One can also think of tailoring the buffer profile to control the injection to improve the brightness of the trapped particle beam. These narrow bunches can also be used as injectors for other accelerators or a positron accelerator [W^+]. For example one could post-accelerate in a conventional accelerator to produce even higher brightness and small energy spread for X-ray FELs.

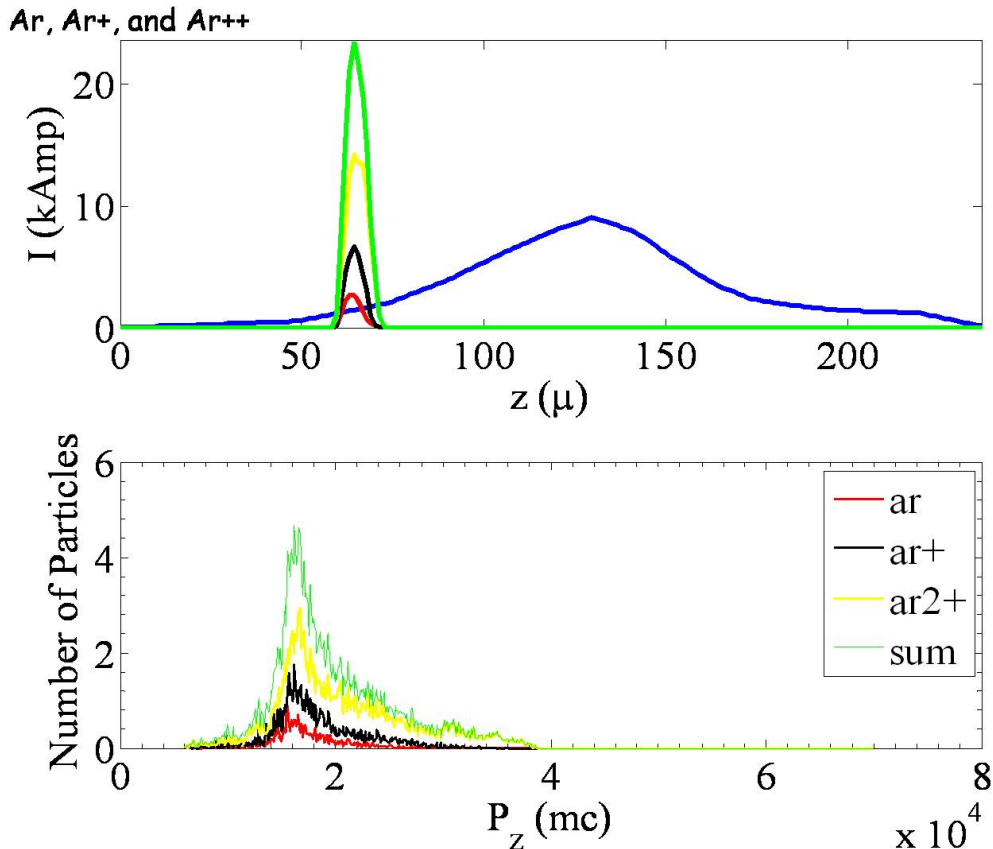


Figure 7.2: Simulation results obtained with the 2-D OSIRIS PIC code, using the plasma profile of Fig. 6.2: (a) Longitudinal profile of the drive bunch (blue) and the trapped particles bunch of argon I electrons (red), argon II electrons (black), argon III electrons (yellow) and the combined current profile (green); (b) the corresponding energy distribution of the trapped particle bunches.

References

- [ADK86] M. V. Ammosov, N. B. Delone, and V. P. Krainov. *Journal of Experimental and Theroretical Physics*, 64:1191, 1986.
- [AP56] A. I. Akhiezer and R. P. Polovin. *Journal of Experimental and Theroretical Physics*, 3:696, 1956.
- [AS70] P.M. Laposstolle A. Septier. *Linear Accelerators*. North Holand Publishing, Amsterdam, 1970.
- [B⁺91] J. Buon et al. A beam size monitor for the final focus test beam. *Nuclear Instruments and Methods in Physics Research Section A*, 306:93–111, 1991.
- [Bar05] C. Barnes. *Longitudinal Phase Space Measurements and Application to Beam-PLasma Physics*. PhD thesis, Stanford University, 2005.
- [BCD⁺06] I. Blumenfeld, C. E. Clayton, F. J. Decker, P. Emma, M. Hogan, C. Huang, R. H. Iverson, D. K. Johnson, C. Joshi, T. Katsouleas, P. Krejcik, W. Lu, K. A. Marsh, W. B. Mori, P. Muggli, C. L. O’Connell, E. Oz, R. H. Siemann, and D. Walz. Energy doubling of 42 gev electrons in a meter scale plasma wakefield accelerator. *Nature*, 2006. To be published, all authors contributed equally to this work.
- [Bor00] M. Borland. Elegant: A flexible sdds-compliant code for accelerator simulation. *Advanced Photon Source LS-287, September 2000*, 2000.
- [Cof71] T. P. Coffey. Breaking of large amplitude plasma oscillations. *Physics of Fluids*, 14(7):1402–1406, 1971.
- [Daw59] J. M. Dawson. *Physical Review*, 113:383, 1959.
- [Den05] S. Deng. *Models and Physics of Plasma Wakefield Accelerators*. PhD thesis, University of Southern California, 2005.
- [H⁺06] C. Huang et al. *Particle Accelerator Conference*, 2006.

- [HAD⁺00] M. J. Hogan, R. Assmann, F.-J. Decker, R. Iverson, P. Raimondi, S. Rokni, R. H. Siemann, D. Walz, D. Whittum, B. Blue, C. E. Clayton, E. Dodd, R. Hemker, C. Joshi, K. A. Marsh, W. B. Mori, S. Wang, T. Katsouleas, S. Lee, P. Muggli, P. Catravas, S. Chattopadhyay, E. Esarey, and W. P. Leemans. E-157: A 1.4-m-long plasma wake field acceleration experiment using a 30 gev electron beam from the stanford linear accelerator center linac. volume 7, pages 2241–2248. AIP, 2000.
- [HBC⁺05] M. J. Hogan, C. D. Barnes, C. E. Clayton, F. J. Decker, S. Deng, P. Emma, C. Huang, R. H. Iverson, D. K. Johnson, C. Joshi, T. Katsouleas, P. Krejcik, W. Lu, K. A. Marsh, W. B. Mori, P. Muggli, C. L. O’Connell, E. Oz, R. H. Siemann, and D. Walz. Multi-gev energy gain in a plasma-wakefield accelerator. *Physical Review Letters*, 95(5):054802, 2005.
- [Hem99] R. Hemker. *the Fifth IEEE Particle Accelerator Conference*, 1999.
- [HNN93] A. Ogata K. Nakajima D. Whittum Y. Yoshida T. Ueda T. Kobayashi H. Shibata S. Tagawa N. Yugami H. Nakanishi, A. Enomoto and Y. Nishida. Wakefield accelerator using twin linacs. *Nuclear Instruments and Methods in Physics Research Section A: Accelerators, Spectrometers, Detectors and Associated Equipment*, 328:596–598, May 1993.
- [int] ILC official website. <http://www.interactions.org/linearcollider/>.
- [JK03] C. Joshi and T. Katsouleas. Plasma accelerators at the energy frontier and on tabletops. *Physics Today*, 56(6):47–53, 2003.
- [K⁺06] N. Kirby et al. *AIP Conf. Proc.*, 2006.
- [KM88] T. C. Katsouleas and W. B. Mori. *Physical Review Letters*, 61:90, 1988.
- [L⁺05] W. Lu et al. Limits of linear plasma wakefield theory for electron or positron beams. *Physics of Plasmas*, 12(6), 2005.
- [LHZ⁺06] W. Lu, C. Huang, M. Zhou, W. B. Mori, and T. Katsouleas. Nonlinear theory for relativistic plasma wakefields in the blowout regime. *Phys. Rev. Lett.*, 96(16):165002, Apr 2006.
- [LSE⁺96] W. P. Leemans, C. W. Siders, E. Esarey, N. E. Andreev, G. Shvets, and W. B. Mori. *IEEE Trans. Plasma Sci.*, 24:331, 1996.

- [MA97] P. Mora and T. M. Antonsen. Kinetic modeling of intense, short laser pulses propagating in tenuous plasmas. *Physics of Plasmas*, 4(1):217–229, 1997. eq. differs slightly because we transform to $z - v_\phi t$.
- [MK90] W. B. Mori and T. C. Katsouleas. *Physica Scripta*, t30:127, 1990.
- [MMW⁺99] P. Muggli, K. A. Marsh, S. Wang, C. E. Clayton, S. Lee, T. C. Katsouleas, and C. Joshi. *IEEE Trans. Plasma Sci.*, 27:791, 1999.
- [MND⁺95] A. Modena, Z. Najmudin, A. E. Dangor, C. E. Clayton, K. A. Marsh, C. Joshi, V. Malka, C. B. Darrow, C. Danson, D. Neely, and F. N. Walsh. Electron acceleration from the breaking of relativistic plasma waves. *nature(London)*, 377:606, October 1995.
- [MOM02] P. Muggli, E. Oz, and K. A. Marsh. *Advanced Accelerator Conference*, 2002.
- [MSZ96] G. V. Stupakov M. S. Zolotorev. 1996. SLAC PUB 7132.
- [MVAK86] N. B. Delone M. V. Ammosov and V. P. Krainov. Tunnel ionization of complex atoms and of atomic ions in an alternating electromagnetic field. *Sov. Phys. JETP*, 64:1191–1194, 1986.
- [OBC⁺04] E. Oz, C. D. Barnes, C. E. Clayton, F. J. Decker, S. Deng, M. J. Hogan, C. Huang, R. H. Iverson, D. K. Johnson, C. Joshi, T. Katsouleas, P. Krejcik, W. Lu, K. A. Marsh, P. Muggli, C. L. O’Connell, and D. Walz. *Advanced Accelerator Conference*, 2004.
- [O’C05] C.L. O’Connell. *Field Ionization of a Neutral Vapor Using a 28.5 GeV Electron Beam*. PhD thesis, Stanford University, 2005.
- [OCD⁺] C. L. O’Connell, C. E. Clayton, F. J. Decker, S. Deng, P. Emma, M. J. Hogan, C. Huang, R. H. Iverson, D. K. Johnson, C. Joshi, T. C. Katsouleas, P. Krejcik, W. Lu, K. A. Marsh, W. B. Mori, P. Muggli, E. Oz, R. H. Siemannand D. Walz, and M. Zhou. submitted to Phys. Rev. ST Accel. Beams.
- [ODK⁺07] E. Oz, S. Deng, T. Katsouleas, P. Muggli, C. D. Barnes, I. Blumenfeld, F. J. Decker, P. Emma, M. J. Hogan, R. Ischebeck, R. H. Iverson, N. Kirby, P. Krejcik, C. O’Connell, R. H. Siemann, D. Walz, D. Auerbach, C. E. Clayton, C. Huang, D. K. Johnson, C. Joshi, W. Lu, K. A. Marsh, W. B. Mori, and M. Zhou. Ionization-induced electron trapping in ultrarelativistic plasma wakes. *Physical Review Letters*, 98(8):084801, 2007.

- [PE05] K. Bane P. Emma. Littrack: A fast longitudinal phase space tracking code with graphical user interface. *Proceedings of the 2005 Particle Accelerator Conference (PAC)*, 2005.
- [Pir05] S. Pirkins. *Sciencenews*, 167(24):382, 2005. <http://www.sciencenews.org/articles/20050611/note15.asp>.
- [Ros88] J. B. Rosenzweig. Trapping, thermal effects, and wave breaking in the nonlinear plasma wake-field accelerator. *Phys. Rev. A*, 38(7):3634–3642, 1988.
- [RSC⁺89] J. B. Rosenzweig, P. Schoessow, B. Cole, W. Gai, R. Konecny, J. Norem, and J. Simpson. Experimental measurement of nonlinear plasma wake fields. *Phys. Rev. A*, 39(3):1586–1589, Feb 1989.
- [Sch04] S. Schreiber. *European Particle Accelerator Conference*, 2004.
- [TN06] R. M. G. M. Trines and P. A. Norreys. Wave-breaking limits for relativistic electrostatic waves in a one-dimensional warm plasma. *Physics of Plasmas*, 13(12):123102, 2006.
- [UKD96] D. Umstadter, J. K. Kim, and E. Dodd. Laser injection of ultra-short electron pulses into wakefield plasma waves. *Phys. Rev. Lett.*, 76(12):2073–2076, 1996.
- [W⁺] X. Wang et al. *Particle Accelerator Conference Proceedings*. <http://pac07.org/proceedings/PAPERS/THPMS037.PDF>.
- [YPP⁺03] V. Yakimenko, I. V. Pogorelsky, I. V. Pavlishin, I. Ben-Zvi, K. Kusche, Yu. Eidelman, T. Hirose, T. Kumita, Y. Kamiya, J. Urakawa, B. Greenberg, and A. Zigler. Cohesive acceleration and focusing of relativistic electrons in overdense plasma. *Phys. Rev. Lett.*, 91(1):014802, Jul 2003.

Appendices

Appendix A

Derivation of the Constant of Motion

We can also derive the constant of motion that was derived in chapter 3 as follows:

$$\frac{dP_z}{dt} = q(E_z + (\mathbf{v} \times \mathbf{B})_z) \quad (A.1)$$

$$E_z = -\partial_t A_z - \partial_z \Phi \quad (A.2)$$

$$\mathbf{V} \times \nabla \times \mathbf{A} = \nabla(\mathbf{V} \cdot \mathbf{A}) - (\mathbf{V} \cdot \nabla)\mathbf{A} \quad (A.3)$$

$$(\mathbf{V} \times \nabla \times \mathbf{A})_z = \partial_z \mathbf{V} \cdot \mathbf{A} - (\mathbf{V} \cdot \nabla)\mathbf{A}_z \quad (A.4)$$

Using these vector identities Eq. A.1 becomes

$$\frac{dP_z}{dt} = q(-\partial_t A_z - \partial_z \Phi + \partial_z \mathbf{V} \cdot \mathbf{A} - \mathbf{V} \cdot \nabla \mathbf{A}_z) \quad (A.5)$$

$$\frac{d\mathbf{P}}{dt} = q(\mathbf{E} + \mathbf{v} \times \mathbf{B}) \quad (A.6)$$

$$\mathbf{V} \cdot \frac{d\mathbf{P}}{dt} = \mathbf{V} \cdot (q(\mathbf{E} + \mathbf{v} \times \mathbf{B})) \quad (A.7)$$

$$\mathbf{P} = \gamma m \mathbf{V} \quad (A.8)$$

It would turn out to be convenient to write the left side of Eq. A.7 as a complete derivative, derivation of which is as follows: (For convenience take $m = 1$)

$$\mathbf{V} \cdot \frac{d\gamma \mathbf{V}}{dt} = V^2 \frac{d\gamma}{dt} + \gamma \mathbf{V} \cdot \frac{d\mathbf{V}}{dt} \quad (\text{A.9})$$

$$\gamma \mathbf{V} \frac{d\mathbf{V}}{dt} = \frac{\gamma}{2} \frac{dV^2}{dt} \quad (\text{A.10})$$

$$\gamma^{-2} = 1 - \frac{V^2}{c^2} \quad (\text{A.11})$$

$$V^2 = c^2 - \frac{c^2}{\gamma^2} \quad (\text{A.12})$$

$$\frac{dV^2}{dt} = -c^2 \frac{d}{dt} \left(\frac{1}{\gamma^2} \right) \quad (\text{A.13})$$

$$= 2c^2 \gamma^{-3} \frac{d\gamma}{dt} \quad (\text{A.14})$$

$$\gamma \mathbf{V} \frac{d\mathbf{V}}{dt} = \frac{c^2}{\gamma^2} \frac{d\gamma}{dt} \quad (\text{A.15})$$

$$\mathbf{V} \cdot \frac{d\gamma \mathbf{V}}{dt} = (V^2 + \frac{c^2}{\gamma^2}) \frac{d\gamma}{dt} \quad (\text{A.16})$$

$$= \left(c^2 - \frac{c^2}{\gamma^2} + \frac{c^2}{\gamma^2} \right) \frac{d\gamma}{dt} \quad (\text{A.17})$$

$$= c^2 \frac{d\gamma}{dt} \quad (\text{A.18})$$

therefore

$$\mathbf{V} \cdot \frac{d\mathbf{P}}{dt} = mc^2 \frac{d\gamma}{dt} \quad (\text{A.19})$$

$$\frac{d}{dt} \gamma mc^2 = q \mathbf{V} \cdot \mathbf{E} \quad (\text{A.20})$$

$$\frac{d}{dt} \gamma mc^2 = q(-\mathbf{V} \cdot \partial_t \mathbf{A} - \mathbf{V} \cdot \nabla \Phi) \quad (\text{A.21})$$

$$\frac{d}{dt} \gamma mc = \frac{q}{c} (-\mathbf{V} \cdot \partial_t \mathbf{A} - \mathbf{V} \cdot \nabla \Phi) \quad (\text{A.22})$$

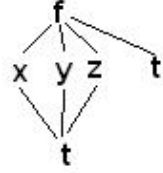


Figure A.1: Partial derivative tree for the variables of interest

subtract Eq. A.5 from Eq. A.22

$$\frac{d}{dt}(\gamma mc - P_z) = q(-\mathbf{V} \cdot \frac{\partial_t}{c} \mathbf{A} - \frac{\mathbf{V} \cdot \nabla \Phi}{c} + \partial_t \mathbf{A}_z + \partial_z \Phi - \partial_z \mathbf{V} \cdot \mathbf{A} + \mathbf{V} \cdot \nabla \mathbf{A}_z) \quad (\text{A.23})$$

add and subtract $\frac{\partial_t}{c} \Phi$ to be able to get a complete time derivative

$$\frac{df}{dt} = \frac{\partial f}{\partial x} \frac{dx}{dt} + \frac{\partial f}{\partial y} \frac{dy}{dt} + \frac{\partial f}{\partial z} \frac{dz}{dt} + \frac{\partial f}{\partial t} \quad (\text{A.24})$$

$$\frac{d}{dt} = \frac{\partial}{\partial t} + \mathbf{V} \cdot \nabla \quad (\text{A.25})$$

$$\frac{d}{dt}(\gamma mc - P_z) = q(-\mathbf{V} \cdot \frac{\partial_t}{c} \mathbf{A} - \frac{1}{c} \frac{d\Phi}{dt} + \frac{\partial_t}{c} \Phi + \partial_z \Phi + \frac{d\mathbf{A}_z}{dt} - \partial_z \mathbf{V} \cdot \mathbf{A}) \quad (\text{A.26})$$

$$\frac{d}{dt}(\gamma mc - P_z + q(\frac{\Phi}{c} - A_z)) = q(\frac{\partial_t}{c} + \partial_z)(\Phi - \mathbf{A} \cdot \mathbf{V}) \quad (\text{A.27})$$

Since the variables on the left side are functions of $z - ct$, the right side of Eq. A.27 is zero therefore $\gamma mc - P_z + q(\frac{\Phi}{c} - A_z)$ is a constant of motion.

A similar derivation in cgs units will give the conserved quantity as

$$\gamma mc - P_z + q \frac{\Psi}{c} = \text{constant} \quad (\text{A.28})$$

where $\Psi = \Phi - A_z$.